Water deuterium fractionation in star-formation regions

Dissertation
zur
Erlangung des Doktorgrades (Dr. rer. nat.)
der
Mathmatisch-Naturwissenschaftlichen Fakultät
der
Rheinischen Friedrich-Wilhelms-Universtät Bonn

vorgelegt von
Fang-Chun Liu
aus
Taipei, Taiwan

Bonn Oct 2017

Angefertigt mit Genehmigung der Mathematisch-Naturwissenschaftlichen Fakultät
der Rheinischen Friedrich-Wilhelms-Universtät Bonn

Diese Dissertation ist auf dem Hochschulschrifttenserver der ULB Bonn unter
http://hss.ulb.uni-bonn.de/diss online elektronisch publiziert.

1.Referent: **Prof. Dr. Karl Menten**

2.Referent: **Prof. Dr. Pavel Kroupa**

Tag der Promotion: 17 Okt. 2017

Erscheinungsjahr: 2017

Dedicated to my parents

Publications

Chapter 3 was published as:

Water deuterium fractionation in the low-mass protostar NGC1333-IRAS2A, Liu, F.-C., Parise, B., Kristensen, L., et al. 2011, A&A, 527, A19

Chapter 4 was published as:

Water deuterium fractionation in the high-mass hot core G34.26+0.15, Liu, F.-C., Parise, B., Wyrowski, F., Zhang, Q., & Güsten, R. 2013, A&A, 550, A37

Abstract

Water is an essential molecule to oxygen chemistry and to the proliferation of life. Also, it is the main constituent of icy grain mantles in the Universe. The formation of water can be studied through the HDO/H_2O ratio. Thanks to the launch of the Herschel Space Observatory and the advance of sensitive submillimeter receivers on ground-based telescopes, many H_2O and HDO transitions can now be observed, enabling more accurate studies of the level of water fractionation, i.e., the enhancement of the HDO/H_2O abundance ratio over the D/H elemental ratio. Using these new technologies, we aim at revisiting the water fractionation studies toward star-forming regions. We present here detailed studies of the D/H ratios of water in one low-mass protostar and six luminous high-mass star-forming regions. Deuterated water has been detected in these sources with ground-based telescopes (APEX and SMA). We analyzed these observations using the 1D radiative transfer code RATRAN to obtain the HDO fractional abundances throughout the envelopes. The results show that the HDO fractional abundances in the inner and outer regions are different by more than two orders, which implies that the sublimation is very similar in low- and high-mass star-forming regions. Previous and our studies show that the values of the HDO fractional abundance in star-forming regions with different masses do not correlate with their evolution. The H_2O abundance is deduced from the analysis of the $H_2^{18}O$ transition lines observed with the Herschel Space Observatory and APEX. The similarity of the measured HDO/H_2O ratios suggests that the chemical evolution of water is the same regardless of the masses of the regions.

Contents

Chapter 1

Introduction

Water is a fundamental molecular component on Earth. Water has been thought to be essential to the proliferation of life and to the chemical evolution of other larger molecules because it helps many chemical reactions, especially those leading to organic compounds. Water is widely found in the Universe. Not only on Earth, water is also found on planets and comets in interstellar clouds and star-forming regions. However, the two main questions are not yet fully answered: how does water form in the universe and where does water on Earth come from.

To solve these questions, we studied the distribution of deuterated water (HDO) in star-forming regions. Deuterated water is a form of water that contains deuterium (D), the hydrogen isotope which has one additional neutron. Although the D/H elemental ratio in the interstellar medium is $\sim 1.5 \times 10^{-5}$ (Linsky 2003), the investigations of water deuterium fractionation (HDO/H_2O) show the ratios are ten times higher in the water on Earth ($\sim 3.1 \times 10^{-4}$, de Laeter et al. 2003) and even much higher in several star-forming regions ($\sim 10^{-2} - 10^{-3}$, Parise et al. 2005a; Bergin et al. 2010; Liu et al. 2011; Coutens et al. 2012). Obviously, chemical reactions and the formation of water take responsibility for this difference. Water can be formed by three mechanisms: dissociative recombination in the gas phase by ion-molecule chemistry (Bergin et al. 2000), combination of atoms on the surface of cold dust grains at low temperature (Tielens & Hagen 1982; Cuppen et al. 2010), and gas phase reactions at high temperature (> 250 K) (Wagner & Graff 1987; van der Tak et al. 2006). Because deuterium enrichment happens only in cold environments, the three scenario above would result in different levels of fractionation. Therefore, studying the HDO/H_2O ratios is a promising method to understand the formation process of water.

In this thesis, we present our studies of the water deuterium fractionation in several star-forming regions spanning a range of masses. With our observational results, current chemical models can be verified to try to constrain the formation of water.

1.1 Water and deuterated water

1.1.1 Importance of water and deuterated water

Water (H_2O) is one of the most important and fundamental molecules (Kasting et al. 1993; Hoover 2006; Lis et al. 2013; van Dishoeck et al. 2013). Water comes in three phases: gas, liquid, and solid ice. Water in liquid form not only influences many chemical reactions as a solvent but it is also essential to the initial development of life and its proliferation.

Because water is a dominant form of oxygen (the third most abundant element in the Universe), it assists many chemical reactions of other species, whether in the gas phase or the solid phase (van Dishoeck et al. 2013). In addition, water can be a coolant with its radiative spectral lines and thus it plays a role in helping interstellar clouds to collapse to form stars (van Dishoeck et al. 2014). Water is also a major component of ice-grain mantles. Therefore, it serves as an excellent probe of the inner and warmer regions of star-forming cloud cores after the water ice has been evaporated (e.g. Gibb et al. 2004; Liu et al. 2013; Coutens et al. 2014).

Water has been widely found in the Universe, in both gas or ice form, with masing, and thermal emission and in infrared bands caused by vibrationally excited states. In our solar system, it exists on the terrestrial planets, moons, asteroids, comets and Kuiper Belt Objects, including as gas in the atmosphere and as ice on the surfaces (see Encrenaz 2008; Hartogh et al. 2011; Lis et al. 2013; Campins et al. 2010; Küppers et al. 2014). Moreover, water also has been observed in many molecular clouds and star-forming regions throughout the Galaxy and even in some external galaxies (Cheung et al. 1969; Cernicharo & Crovisier 2005; Boogert et al. 2008; Shimonishi et al. 2010; Liu et al. 2011; Bergin & van Dishoeck 2012; Liu et al. 2013; Weiß et al. 2013). Hence, water molecules exist in a large variety of environments and sources, T $<$10 K in cold prestellar cores to T $\sim$ 2000K in shocks and protoplanetary disks; Density $\sim 10^4$ cm^{-3} in molecular clouds to $\sim 10^{19}$ cm^{-3} in planetary atmospheres, see van Dishoeck et al. (2013).

At the same time, molecular deuteration has been the focus of many studies. The abundance of deuterated molecules has been shown to be significantly increased in low-temperature environments (e.g. Snell & Wootten 1977; Wootten et al. 1982; Roueff et al. 2000; Loinard et al. 2001), compared to the D/H elemental ratio in the interstellar medium ($\sim 1.5\times10^{-5}$, Linsky 2003). This can be interpreted based on the chemical formation pathways of these molecules, and therefore the level of deuterium fractionation of molecules is a potentially good tracer of their formation process (Ceccarelli et al. 1998; Parise et al. 2004; Liu et al. 2011; van Dishoeck et al. 2013). In the past, it has been found that for water the fractionation is significantly lower than formaldehyde and methanol in the same sources (van Dishoeck et al. 1995; Parise et al. 2005a; Roberts & Millar 2007; Liu et al. 2011, 2013). This suggests that these species do not form simultaneously on dust surfaces. Thanks to the advance of sensitive submillimeter receivers, such as those on the APEX telescope, and to the launch of Herschel, it is now possible to carry out much more detailed radiative transfer analyses of HDO and H_2O. We aim in this thesis to carry out such a detailed study on low- and high-mass star-forming regions to constrain the formation of water.

1.1.2 Water chemistry

In environments where densities are above $\sim 10^{13}$ cm^{-3}, such as planetary atmospheres and the shielded mid-planes of inner protoplanetary disks, the fractional abundance of water is governed by the elemen-

tal composition of the gas (three-body reactions) and the stability of molecules and solids. In such an environment the chemistry is close to thermodynamic equilibrium (TE). However, in most cases in interstellar space, the densities are much lower than the required condition for equilibrium chemistry. Similarly, the equilibrium chemistry cannot prevail in strong UV irradiation environments, such as the upper atmospheres and disks of planets. The fractional abundances of water then are mainly determined by two-body reactions. Below, we introduce the three identified mechanisms which can form water under different conditions.

1.1.2.1 High-temperature gas-phase chemistry

In high-temperature environments (> 250 K), the chemical equation O+H_2→OH+H is the dominant reaction initiating water formation (Elitzur & Watson 1978) and then OH reacts with H_2 to form H_2O. The energy barriers for these two reactions can be overcome in high-temperature environments (Wagner & Graff 1987; Atkinson et al. 2004; van der Tak et al. 2006; van Dishoeck et al. 2013).

1.1.2.2 Low-temperature gas-phase chemistry

At temperature < 100 K and densities $< 10^4$ cm^{-3}, ion-molecule chemistry in the gas phase plays a main role to form water (Herbst & Klemperer 1973; Bergin et al. 2000; Bergin & van Dishoeck 2012; van Dishoeck et al. 2013). This network starts from the products of cosmic ray ionization of H_2 or O (H_2^+, H^+, or O^+). The H_2^+ and H^+ ions will have fast reactions with H_2 to form H_3^+. Then, OH^+ is produced with the reactions O+H_3^+ or O^++H_2. The following steps are the rapid reactions to form H_3O^+:

$$\begin{aligned} \mathrm{OH^+ + H_2} &\rightarrow \mathrm{H_2O^+ + H} \\ \mathrm{H_2O^+ + H_2} &\rightarrow \mathrm{H_3O^+ + H} \end{aligned}$$

With electrons, H_3O^+ will dissociatively recombine to form H_2O and OH:

$$\begin{aligned} \mathrm{H_3O^+ + e^-} &\rightarrow \mathrm{H + H_2O} \\ &\rightarrow \mathrm{OH + H_2} \\ &\rightarrow \mathrm{OH + 2H} \end{aligned}$$

The productivity ratios here for H_2O and OH are ∼0.17 and ∼0.83, respectively (Buhr et al. 2010).

1.1.2.3 Low-temperature grain-surface chemistry

Because the timescale for an atom or a molecule to collide with a grain and then stick to it is $\sim 3 \times 10^9/n_{H_2}$ in dense environments ($> 10^4$ cm^{-3}), the required time for freeze-out is less than a few 10^5 yr. This timescale is smaller than the lifetime of dense cores, so the grain-surface reactions are important in chemical networks. In fact, the observed water ice abundance is much higher than the expected value predicted only with the direct condensation of gaseous water (e.g. Watanabe & Kouchi 2008). Most water ice can be produced via three routes including hydrogenation of oxygen, molecular oxygen and

ozone on grain surfaces (Tielens & Hagen 1982; Miyauchi et al. 2008; Oba et al. 2009; Mokrane et al. 2009; Cuppen et al. 2010; Dulieu et al. 2010; Lamberts et al. 2013; Coutens et al. 2014):

$$\mathrm{O + H} \rightarrow \mathrm{OH}, \qquad \mathrm{OH + H \rightarrow H_2O}. \tag{1.1}$$

$$\mathrm{O_2 + H} \rightarrow \mathrm{HO_2}, \qquad \mathrm{HO_2 + H \rightarrow H_2O_2}, \qquad \mathrm{H_2O_2 + H \rightarrow H_2O + OH}. \tag{1.2}$$

$$\mathrm{O_3 + H} \rightarrow \mathrm{OH + O_2}, \quad \mathrm{OH + H_2 \rightarrow H_2O + H}. \tag{1.3}$$

After water ice has formed, non-thermal desorption and thermal sublimation can convert solid water back to the gas phase (water vapor). Non-thermal desorption includes UV-photodesorption (Prasad & Tarafdar 1983; Andersson & van Dishoeck 2008), which is thought to dominate the production of gaseous water in cold environments under the thermal sublimation temperature, and chemical desorption (Dulieu et al. 2013). Once the dust temperatures rise above the sublimation temperature, for example in warmer and inner envelopes, water ice thermally sublimates.

1.1.3 The origin of the deuterium and deuterated hydrogen

Deuterium (D) is produced during the Big Bang Nucleosynthesis (BBN) process which happened in the first few minutes after the Big Bang. In the very early Universe, the temperature was too high to form deuterons (nuclei of deuterium). It is because high energy photons immediately destroy the binding of deuterons (deuterium bottleneck) when they form. Therefore, deuterons started to be formed after the temperature of the expanding Universe fell to $\sim$ 1 billion K (Boesgaard & Steigman 1985, and references therein):

$$\mathrm{p + n} \rightarrow \mathrm{d} + \gamma \tag{1.4}$$

where p is a proton, n is a neutron, and γ is a photon. This reaction is exothermic and the binding energy of deuterium is 2.2 MeV.

Once deuteron formation has occurred, the nuclei proceed to form helium nuclei. The binding energy of a helium nucleus is 28 MeV, which is much larger than that of the deuteron, so the reactions of helium formation have only one direction. After the temperature of the Universe dropped to $\sim 5{\times}10^8$ K, the formation of helium nuclei stopped due to the electrostatic repulsion of the deuterons. In the end, BBN resulted in $\sim$ 91% of H^1, $\sim$ 8% of He^4, and $\sim$ 0.001% of D (by number of nuclei) (Wagoner 1969, 1973; Yang et al. 1984; Peimbert & Torres-Peimbert 1999; Steigman 2006). After BBN, deuterium is mainly destroyed in the interiors of stars. Hence, the D/H ratio in the local interstellar medium is $\sim (2.0 - 1.5) \times 10^{-5}$ (Linsky 2003; Prodanović et al. 2010).

Deuterated hydrogen (HD) is a main reservoir of D in molecular clouds and it plays an important role in deuterium chemistry. The formation of HD follows two main routes (Lepp & Shull 1984; Latter 1989; Puy et al. 1993; Galli & Palla 1998; Lepp et al. 2002; Glover & Abel 2008):

$$\mathrm{D + H_2} \rightarrow \mathrm{HD + H}. \tag{1.5}$$

$$\mathrm{D^+ + H_2} \rightarrow \mathrm{HD + H^+}. \tag{1.6}$$

The reaction (1.5) has been measured in many experiments with a wide range of temperatures (e.g., Mitchell & Roy 1973; Michael & Fisher 1990) and theoretical calculations are in good agreement with

the experimental data (e.g., Mielke et al. 1994; Charutz et al. 1997). In diffuse interstellar clouds, reaction (1.6) is the major source of HD and its rate coefficient is almost constant with temperature (e.g., Dalgarno et al. 1973; Gerlich 1982).
The reverse reactions of (1.5) and (1.6) are the main pathway for destruction HD. The reaction HD + H^+ $\rightarrow$ D^+ + H_2 is endothermic and thus the removal of HD is reduced at low temperature, causing significant fractionation.

1.1.4 Water deuteration

The pathways for the formation of deuterated water (HDO) are likely the same as the ones of the formation of water (H_2O) (Pineau des Forets et al. 1991; Ceccarelli et al. 2014; Cleeves et al. 2014; Oba et al. 2014). However, in different conditions, there are several chemical processes able to form HDO or even enhance the HDO/H_2O ratio. In the case of high-temperature gas-phase chemistry, the direct exchange reaction $H_2O + HD \rightarrow HDO + H_2$ is considered to be important (Richet et al. 1977; Geiss & Reeves 1981; Lécluse & Robert 1994). In addition, the abundance of OD, which reacts with H_2 to form deuterated water, will be enhanced with the exchange reaction $D + OH \rightarrow H + OD$ (barrier is $\sim$100 K, Thi et al. 2010; Sultanov & Balakrishnan 2004). In low-temperature environments, abundances of H_2D^+, HD_2^+ , and D_3^+ in the gas phase are increased because of the two chemical processes below. First, the reaction $HD + H_3^+ \rightarrow H_2 + H_2D^+$ has a barrier so that H_2D^+/H_3^+ becomes larger with time (Millar et al. 1989; Roberts et al. 2004; Ceccarelli et al. 2014). Second, when the ortho-H_2 abundance drops and the important destruction partners of these H_3^+ isotopologues (CO and O) freeze out on the grains at low temperature ($\lesssim$25 K), the formation rate of the deuterated species increases (Dalgarno & Lepp 1984; Pagani et al. 1992; Roberts et al. 2003). The enhancement of H_2D^+ leads to an increase of the abundance of H_2DO^+, which will dissociatively recombine with electrons to form HDO in cold gas. Solid HDO can form via three additional pathways. The first pathway is that H atoms in water ice (H_2O) can be exchanged with D atoms from other deuterated molecules trapped in the ice, such as CH_3OD and D_2O, and this isotopic exchange occurs at $\gtrsim$ 120 K, in the process of crystallization or sublimation (Ratajczak et al. 2009; Gálvez et al. 2011). Secondly, the H–D exchange in methane-water ices can form HDO after these ices are ultraviolet photolyzed (Weber et al. 2009; Ceccarelli et al. 2014). The D/H ratios of water and other more complex organic molecules will alter with this mechanism. And finally, the third route is through a thermal exchange, for example, H_2O + OD $\rightarrow$ HDO + OH. These exchange reactions can both increase and decrease the fractionation (van Dishoeck et al. 2014).

1.1.5 The variation in the water deuteration fractionation

Given the D/H elemental ratio in the interstellar medium (see Section 1.1.3), the HDO/H_2O ratio should be $\sim (4-3) \times 10^{-5}$ if there were no deuterium fractionation. However, past studies show that the D/H ratios of water are always found to be higher than this value and vary from place to place. Inside the solar system, the HDO/H_2O ratio is 3.1×10^{-4} in Earth's oceans (de Laeter et al. 2003) and this value is similar to the values found in at least two comets (Hartogh et al. 2011; Bockelée-Morvan et al. 2012), but this value is a factor of 2 lower than that found in most comets (Villanueva et al. 2009). In addition,

the data from the Rosetta mission to comet 67 P/Churyumov- Gerasimenko suggest that the D/H ratio of water in Jupiter family objects has a wider range (Altwegg et al. 2015). Hence, the question whether most water on Earth originates from impact of asteroids or comets is still not clearly answered.
Past studies toward the envelopes of low-mass protostars found that values of the HDO/H_2O ratio show a very large variation. In the very inner region of the cores, ($\lesssim$ 300 AU), the ratios range from $\sim 10^{-3} - 10^{-4}$ (Coutens et al. 2012, 2013a; Persson et al. 2013, 2014). For larger scales of the warm region of the cores, (e.g. $\sim$ 2500 AU), much higher D/H ratios have been obtained ($\sim 10^{-2}$ to $\sim 10^{-3}$ Parise et al. 2005a; Liu et al. 2011; Coutens et al. 2012). In the cold/outer envelopes of low-mass protostars, the HDO/H_2O ratios are slightly lower again ($\sim 10^{-3}$ Parise et al. 2005a; Liu et al. 2011; Coutens et al. 2012). On the other hand, the D/H ratios of water in high-mass star-forming regions are $\sim 10^{-3}$ to $\sim 10^{-4}$ (Gensheimer et al. 1996; van der Tak et al. 2006; Liu et al. 2013; Emprechtinger et al. 2013; Coutens et al. 2014). Therefore, HDO/H_2O ratios show a wide variation.

1.2 Star formation

Stars are the fundamental components in the Universe and the crucibles in which heavy elements are produced. In the last decades, there has been much progress in our understanding of the formation of stars. In this section, we briefly describe the evolutionary stages of low-mass star formation (Section 1.2.1) and then outline possible scenario of massive star formation (Section 1.2.2).

1.2.1 Low-mass star formation

Observations suggest that the formation of a low-mass star involves a series of different stages (Lada 1987; Shu et al. 1987; André et al. 2000; McKee & Ostriker 2007)(Figure 1.1):
Pre-stellar Cores (Figure 1.1b)
In dense molecular clumps (size: $\sim 0.3 - 3$ pc, density: $10^3 - 10^4$ cm^{-3}) embedded in dark molecular clouds (size: $\sim 2 - 15$ pc, density: $50 - 500$ cm^{-3}), matter slowly accumulates toward the center and causes central condensations to form dense cores (size: $\sim 0.03 - 0.2$ pc, density: $10^4 - 10^5$ cm^{-3}, T $\sim$ 10 K, Bergin & Tafalla 2007, and reference therein). Past studies show that these dense cores have flat inner radial density profiles and do not have outflows or internal heating sources. Therefore, they are considered to be precursors of protostars (Mizuno et al. 1994; Ward-Thompson et al. 1994) and named "pre-stellar cores". In other words, the definition of a pre-stellar core is a gravitationally bound core whose density is increasing toward its center, but in which no central hydrostatic protostellar object exists yet (André et al. 2000).
Class 0 (Figure 1.1c)
Once free-fall collapse happens due to gravitational instability, a strong central concentration of matter will be produced and this process will end with the formation of a hydrostatic protostellar object (Larson 1969; Bate 1998). The gravitational energy is converted into radiation, so that the envelope around this protostar is heated from the inside-out. At this stage, most of the mass of the core is still in the envelope and the protostar is embedded in its envelope. Class 0 protostars are therefore only detected at submillimeter and IR wavelengths. In addition, jets and outflows are launched to remove the excess of angular

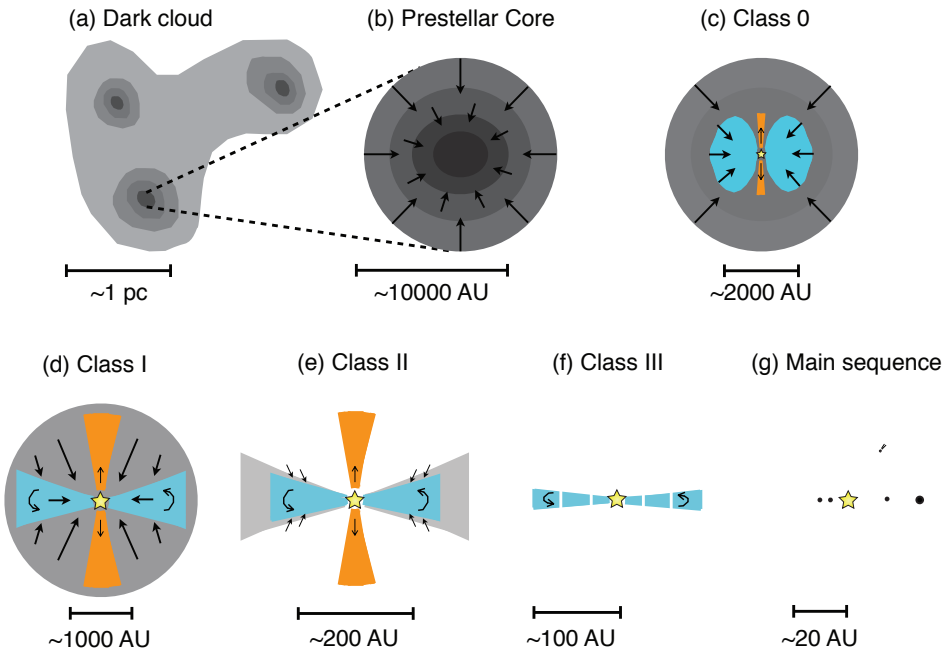

Figure 1.1 Evolutionary stages of low-mass star formation (adapted from Wilking 1989; Wang 2013)

momentum to allow accretion onto the central objects.

Class 0 sources are now defined by several observational properties (Andre et al. 1993; Chen et al. 1995, 1997; André et al. 2000): (i) evidence that indicates the existence of a central young stellar object (YSO), such as an internal heating source or a collimated CO outflow; (ii) extended but centrally peaked submillimeter continuum emission, suggesting the presence of a circumstellar dust envelope ; (iii) a high ratio of submillimeter to bolometic luminosity, indicating that the envelope mass exceeds the central stellar mass; (iv) bolometeric temperature less than 70 K. Hence, Class 0 sources are considered to be hydrostatic YSOs in their main accretion phase and believed to have rich material in their envelopes whose mass is greater than the stellar mass (André et al. 2000).

Class I (Figure 1.1d)

From the Class 0 to the Class I stage, accretion of material onto the protostar continues from the envelope and circumstellar disks settle into Keplerian rotation due to the conservation of angular momentum of the infalling gas. When half of the initial mass has been accreted on to the protostar and the disk, one speaks of a Class I object. These objects are observationally defined as having a bolometeric temperature of more than 70 K, but a core is still optically invisible. Although most radiation is still reprocessed by the envelope, some direct radiation from the central protostar is already detectable in their spectral energy distribution (SED), which has a different shape from the SEDs of Class 0 (which are similar to a single-temperature modified blackbody).

Class II/Classical T Tauri (Figure 1.1e)

After most gas and dust of the envelope has been accreted onto the protostar, the central star is considered

to be a pre-main sequence star (PMS star). It is now optically visible and shows up on the stellar birthline in the Hertzsprung-Russell diagram (H-R diagram). Its SED shows the contribution of the radiation from the stellar photosphere and disk (IR excess). The energy source is gravitational contraction. The material in the disk is continuously accreted onto the star and bipolar jets/outflows are still active. At this stage, the mass of the PMS star is close to its final mass.

Class III (Figure 1.1f)

After the Classical T Tauri star stage, the nebular disk will gradually condense into planets or stellar companions and the bipolar outflow ceases. The central PMS star contracts and its internal temperature rises until it begins hydrogen burning, and the star reaches the zero age main sequence.

1.2.2 High-mass star formation

Although our understanding of the formation of the high-mass stars or star clusters is not yet as clear as in the low mass case, modern techniques, providing interferometer telescopes with submillimeter receivers, allow us to observationally classify massive star-forming cores (Churchwell 1999; Beuther et al. 2007; Zinnecker & Yorke 2007). We highlight the various stages below (Figure 1.2).

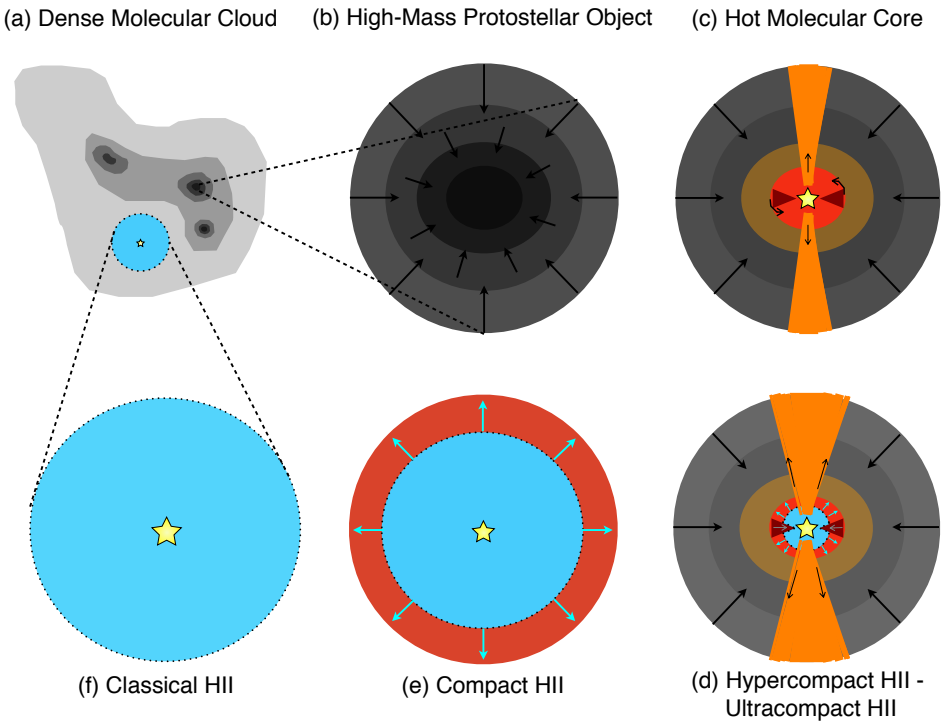

Figure 1.2 Observational classification of massive star-forming cores (adapted from Wang 2013).

High-mass starless core (Figure 1.2a)

Typically, a high-mass starless core (HMSC) is thought to be the starting point for massive star forma-

tion. It is located in a molecular clump with a mass of ∼100–1000 $M_{\odot}$ and a scale of 0.25 to 0.5 pc. The temperature of a HMSC is a local minimum (< 20 K) and the density is a local maximum (> 10^6 cm^{-3}) (e.g., Beuther et al. 2002; Williams et al. 2004). HMSCs are rare, implying that their timescales probably are very short (Ragan et al. 2012). On the other hand, the existence of HMSCs is still doubtful and many scientists are trying to find and study possible candidates (e.g., Sridharan et al. 2005; Olmi et al. 2010; Kong et al. 2016).

High-mass protostellar object (Figure 1.2b)

High-mass protostellar Objects are classified based on the detection of infall signatures, detection of strong dust emission (sub-mm), and non-detection of free-free emission from the ionized gas (de Buizer 2004). The lack of centimeter-wave emission indicates that the forming protostar does not yet emit strong UV radiation. Because HMPOs begin as a protostar just after creation via free-fall collapse, the central hot core is still small in both mass and size. HMPOs are still relatively cold and deeply embedded in their envelopes, so they can not be detected at mid-infrared or shorter wavelengths and have no or weak emission from complex molecules (de Buizer 2004; Wang 2013).

Hot molecular core (Figure 1.2c)

Hot molecular cores (HMCs) are dense (> 10^6 cm^{-3}) and warm (> 100 K). They always show rich emission from complex organic molecules such as CH_3OH, CH_3CCH, $HCOOCH_3$ and HC_3CN, etc. (e.g., Kurtz et al. 2000; Cesaroni 2005; Herbst & van Dishoeck 2009). This indicates that the star-forming core has been significantly heated up, so the ice on the grain evaporates, which is followed by further high-temperature gas-phase chemical reactions (Herbst & van Dishoeck 2009).

Hypercompact and ultracompact HII regions (Figure 1.2d)

After the forming massive stars start fusion and reach high surface temperatures, their UV radiation ionizes the surrounding gas and thus compact bubbles of photoionized gas appear (Kurtz 2005; Hoare et al. 2007). These are called hypercompact or ultracompact HII regions (HCHII or UCHII) and their central stars are still embedded within their natal molecular clumps (Churchwell 2002; Hoare et al. 2007). The main difference between the two is their size: typical sizes of HCHII and UCHII are $\lesssim$ 0.03 and $\lesssim$ 0.1 pc (Kurtz 2005), respectively.

Compact and classical HII regions (Figure 1.2e and f)

In these sources, photo-ionization happens spherically in $\lesssim$ 0.5 (compact HII region) and $\sim$ 10 (classical HII region) pc scales (Mezger et al. 1967; Yorke 1986; Kurtz 2005). They show the recombination lines of hydrogen and some forbidden lines of O^+, O^{++}, and N^+. During this stage, the HII region expands dynamically and thus may break out of its parent molecular cloud. The central massive stars therefore can be observed at optical and near-infrared wavelengths (Ward-Thompson et al. 2004).

1.3 Questions, motivation and aims

The investigation of the D/H ratios of water in different places in the Universe, raises questions: why does the D/H ratio of water show so much variation and how does water forms? Generally, chemistry is thought to be responsible for this difference. For example, the lower D/H ratios of water indicate that water does not form simultaneously on dust surfaces with formaldehyde and methanol (van Dishoeck et al. 1995; Parise et al. 2005a; Roberts & Millar 2007; Liu et al. 2011, 2013). Therefore, the D/H ratios of water are very crucial for us to understand the formation and the chemical evolution of water. In fact,

several frameworks of water chemistry in interstellar space have been built, and some critical reactions have been measured in the laboratory in the last decade (see Section 1.1.2 and 1.1.3). However, due to the limitation of the observational instruments (including the angular resolution and detectable wavelengths), they were not fully tested and verified on a large observational sample. Now, detailed analyses of HDO and H_2O become available because of the advance of sensitive submillimeter receivers and the launch of Herschel, enabling us to have more accurate studies to test these chemical networks. In this thesis, we present our studies of the HDO/H_2O ratios in different-masses star-forming regions to try to improve our understanding of water formation.

1.4 Outline of this thesis

The thesis is laid out as follows. Chapter 2 describes the tools used in this thesis. Sections 2.1 is about radiative transfer and molecular exciation, because the measurement of electromagnetic radiation plays a key role in this work. The observational techniques (single-dish and interferometry) and the modeling tools used to analyze the observed data are described in Section 2.2 and 2.3, respectively.
Chapters 3 to 5 present the studies of water deuterium fractionation in different star-formation regions (Chapter 3 – low-mass, Chapters 4 and Chapter 5 – high-mass). The observational data and the analysis with radiative transfer modeling are presented in these chapters. Chapters 3 and 4 has been published and refereed in the journal Astronomy & Astrophysics (Liu et al. 2011, 2013) while that of Chapter 5 will be submitted to the same journal. Finally, I discuss and conclude the results from all my studies in Chapter 6.

Chapter 2

Methodology

This chapter describes the methodology used in this thesis. Brief descriptions of radiative transfer processes, Planck equation, and Rayleigh-Jeans approximation are presented in Sections 2.1.1. and 2.1.2. Then, basic ideas about the determination of the molecular energy level population are discussed in Sections 2.1.3 to 2.1.5. Section 2.2 explains how to measure the radiation with single-dish and interferometer telescopes and Section 2.3 demonstrates the radiative transfer modeling.

2.1 Radiative transfer and molecular excitation

2.1.1 Basic radiative transfer

Propagation of radiation with the specific intensity (I_ν) though a medium is illustrated in Figure 2.1. The intensity is weakened by absorption/scattering and reinforced by emission or scattering from other

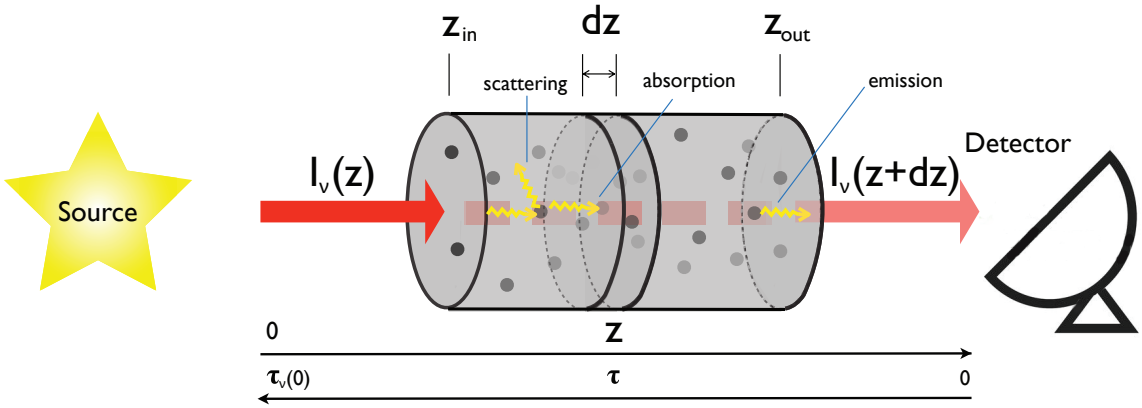

Figure 2.1 A sketch of the radiative transfer process. The coordinate along the line of sight (z) increases from z_{in} to z_{out}. At z_{out}, the optical depth at a frequency ν (τ_ν) is 0 and it increases with the opposite direction to the direction of z. I_ν is the specific intensity.

direction. Because our observations were done at wavelengths longer than near-infrared (mainly sub-millimeter and millimeter), the scattering here can be completely neglected. This process can be described by the equation of radiative transfer:

$$\frac{dI_\nu}{dz} = -\rho\kappa_\nu I_\nu + j_\nu \tag{2.1}$$

where I_ν is the specific intensity in an infinitesimal frequency range d_ν, $\rho\kappa_\nu$ is called absorption coefficient ($1/\rho\kappa_\nu$ is the photon mean free path), κ_ν is the opacity (in $\mathrm{cm^2 g^{-1}}$) and j_ν is the emission coefficient (also called emissivity). The parameters (κ_ν and j_ν) are macroscopic parameters. They specify the probability that a photon is absorbed and emitted, respectively. They are related to the frequency as well as the properties and the density of the atoms or molecules.
The optical depth at a frequency ν (τ_ν) is differentially defined as

$$d\tau_\nu = -\rho\kappa_\nu dz \tag{2.2}$$

Note that at z_{out}, the optical depth (τ_ν) is 0 and it increases with the opposite direction to the direction of the coordinate system of z. Therefore, the basic equation of radiative transfer (2.1) can be written as

$$\frac{dI_\nu}{d\tau_\nu} = I_\nu - S \tag{2.3}$$

with the source function $S \equiv \frac{j_\nu}{\rho\kappa_\nu}$ which is a local property of the medium.
Multiplying this equation by $e^{-\tau}$ and the Integrating the equation from 0 to τ yields

$$I_\nu(z_{out}) = I_\nu(z_{in})e^{-\tau_\nu(0)} + \int_0^{\tau_\nu(0)} S_\nu(\tau)e^{-\tau}d\tau \tag{2.4}$$

where $I_\nu(z_{in})$ is the background intensity, and $I_\nu(z_{out})$ is the intensity arriving at the observers location.
In the following, we describe the solutions of transfer equation (2.4) in some particular cases.
If the source function is uniform, solving the integral gives

$$I_\nu(z_{out}) = I_\nu(z_{in})e^{-\tau_\nu(0)} + S_\nu(1 - e^{-\tau_\nu(0)}) \tag{2.5}$$

If the medium is optically thin ($\tau_\nu(0) \ll 1$), the intensity is

$$I_\nu(z_{out}) = I_\nu(z_{in}) + S_\nu\tau_\nu(0) \tag{2.6}$$

If the medium is optically thick ($\tau_\nu(0) \gg 1$), the intensity is

$$I_\nu(z_{out}) = S_\nu \tag{2.7}$$

Thus, the detector only receives the emission from the foreground. Because τ_ν is very dependent on frequency, different layers can be seen when we observe a source at different frequencies.

2.1.2 Planck equation and Rayleigh-Jeans approximation

In thermal equilibrium (TE), the spectral radiance emitted by a black body (B) can be described with Planck's equation at a given temperature T. The expression is

$$B = \frac{2h\nu^3}{c^2}(e^{\frac{h\nu}{kT}} - 1)^{-1} \tag{2.8}$$

where k is the Boltzmann constant, h is the Planck constant, and c is the speed of light. Thus, the Planck function shows that the radiation emitted by a body is governed by its temperature.
There is a famous approximation, called the Rayleigh-Jeans approximation which can be used if $h\nu$ is much smaller than kT. In this case, $e^{\frac{h\nu}{kT}} \approx 1 + \frac{h\nu}{kT}$:

$$B_{\mathrm{RJ}} = \frac{2h\nu^3}{c^2}\frac{kT}{h\nu} = \frac{2\nu^2 kT}{c^2} \tag{2.9}$$

Because $B \propto T$ here, an intensity I can be expressed with a brightness temperature T_b when we have low-frequency observations ($h\nu \ll kT$).

2.1.3 Basic molecular excitation

Microscopically, the interaction between radiation and matter is described by the Einstein coefficients A and B. A_{ul}, B_{lu}, and B_{ul} are for spontaneous emission, absorption, and stimulated emission, respectively (Einstein 1916, 1917). For simplicity, we consider the two-level case (l for lower, u for upper) of a molecule here (Figure 2.2). The Energy difference between upper and lower state is

$$\Delta \mathrm{E} = \mathrm{E}_u - \mathrm{E}_l \tag{2.10}$$

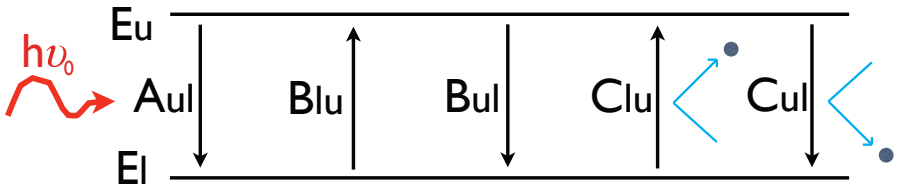

Figure 2.2 A sketch of molecular excitation in the two-level case. A_{ul}, B_{lu}, and B_{ul} are the Einstein coefficients. C_{lu} and C_{ul} are the collisional rate coefficients.

When the photon is emitted or absorbed during a transition, a spectral line with frequency $\nu_0 = \Delta \mathrm{E}/h$ is caused (emission or absorption lines). The number density in the upper level, n_u, decreases by spontaneous emission, which is proportional to n_u itself and to the Einstein A coefficient. Moreover, n_u and n_l (number densities of lower level) are also affected by the absorption and stimulated emission which are described by the Einstein B_{ul} and B_{lu} coefficients. They both are related to the radiation and the probabilities thus are proportional to the mean intensity J_{ul}. Therefore, the populations (n_u and n_l) change according to

$$\frac{dn_u}{dt} = -\frac{dn_l}{dt} = -A_{ul}n_u - B_{ul}J_{ul}n_u + B_{lu}J_{ul}n_l \tag{2.11}$$

The last two terms describe the induced emission which means that a passing photon of the right frequency is doubled and the absorption of a passing photon, respectively.
In addition to radiative transitions, collisions, which happen between particles, also change the state of the molecules. C_{lu} and C_{ul} (from upper to lower and from lower to upper level, respectively) are the collisional rate coefficients which depend on the molecule, the levels, and the collision partner. In

molecular clouds, the main collision partners are molecular hydrogen, electrons and helium atoms. (In this work, the differences for collisions between HDO and ortho–H_2, and collisions between HDO and para–H_2 are adopted.) Therefore, the system can be excited with absorption of radiation and collision, while the system can also be de-excited with stimulated emission, spontaneous emission and collisions

$$\frac{dn_u}{dt} = -\frac{dn_l}{dt} \quad = \quad -n_u(A_{ul} + B_{ul}J_{ul} + n_{col}C_{ul}) + n_l(B_{lu}J_{ul} + n_{col}C_{lu}) \tag{2.12}$$

In the end, the observed spectral lines are the results of the balance between radiation and collision. Note that Einstein coefficients and collisional rate coefficients are intrinsic properties of a transition of a molecule/atom.

2.1.4 Boltzmann distribution, excitation temperature, and the relations between the coefficients

In thermal equilibrium (TE), the levels in an isolated system are populated according to the Boltzmann distribution:

$$\frac{n_u}{n_l} \quad = \quad \frac{g_u}{g_l} e^{-\frac{h\nu}{kT}}, \tag{2.13}$$

where $h\nu$ is the energy difference between two levels (n_u and n_l) and the statistical weight g is the degeneracy of a level. In the general case out of TE, the excitation temperature (T_{ex}) is defined via the Boltzman relation by the ratio of the population in the two levels.

To understand the relations between collisional rate coefficients and Einstein coefficients, we can consider the following two extreme cases.

If the radiation is strong enough and thus the collision can be neglected, the emission terms will equal to the absorption term in TE. Hence, with equation (2.12), we have

$$n_u(A_{ul} + B_{ul}J_{ul}) \quad = \quad n_l(B_{lu}J_{ul}). \tag{2.14}$$

Inserting the Boltzmann equation (2.13) and rearranging the formula, then we get

$$J_{ul} \quad = \quad \frac{A_{ul}/B_{ul}}{(g_l B_{lu}/g_u B_{ul})(e^{\frac{h\nu}{kT}} - 1)}. \tag{2.15}$$

In TE, the radiation field is given by the Planck formula (2.8), which means $J_{ul} = B$. To make the mean intensity (J_{ul}) equal to the Planck function, the Einstein coefficients must satisfy the relations below:

$$g_l B_{lu} = g_u B_{ul} \tag{2.16}$$

and

$$A_{ul} = \frac{2h\nu^3}{c^2} B_{ul}. \tag{2.17}$$

The two equations (2.16) and (2.17) are called the equations of detailed balance. Because the Einstein coefficients do not depend on environmental conditions, the relations above are generally valid.

The radiative terms can be neglected if the density of collision partners n_{col} is high enough. The level population in steady state will be determined by

$$n_u C_{ul} \quad = \quad n_l C_{lu}. \tag{2.18}$$

With the Boltzmann equation (2.13), the collisional rate coefficients are related as

$$\frac{C_{lu}}{C_{ul}} = \frac{g_u}{g_l} e^{-\frac{h\nu}{kT_{kin}}}. \tag{2.19}$$

Therefore, one of the collisional rate coefficents can be calculated if the other one and T are known.

2.1.5 Critical density

Considering a two-level system which does not have background radiation, the system only has collisions to excite the upper levels. These then decay collisionally or radiatively. Thus in steady state, equation (2.12) becomes

$$\frac{dn_u}{dt} = -\frac{dn_l}{dt} = -n_u(A_{ul} + n_{col}C_{ul}) + n_l n_{col} C_{lu} = 0. \tag{2.20}$$

Rearranging the formula above,

$$\frac{n_u}{n_l} = \frac{n_{col}C_{lu}}{n_{col}C_{ul} + A_{ul}}. \tag{2.21}$$

Inserting the relation (2.19) and defining the critical density $n_{cr} \equiv \frac{A_{ul}}{C_{ul}}$,

$$\frac{n_u}{n_l} = \frac{1}{1 + \frac{n_{cr}}{n_{col}}} \cdot \frac{g_u}{g_l} e^{-\frac{h\nu}{kT_{kin}}}. \tag{2.22}$$

Comparing this equation with the equation (2.13), it is found that T_{ex} is equal to T_{kin} when n_{col} is much larger than n_{cr}. On the contrary, if radiative processes dominate, the gas is thermalized by the radiation.

2.2 Observational Techniques

In star-forming regions, observations at submillimeter and millimeter wavelengths are important because the cold dust and gas can be probed through these bands. In addition, chemical and physical conditions, such as abundances, distributions of molecules, temperature, and kinematics, can be investigated through rotational transitions of molecules which are located in these bands. In this thesis, we observed the HDO transitions in the millimeter and submillimeter wave bands from 80 GHz to 893 GHz (see Table 2.1). The basic concepts of the measurements we used are briefly presented below.

2.2.1 Single-dish Telescopes

Single-dish telescopes collect the radiation with a parabolic dish. The intensity of the incoming radiation is measured by a receiver in the telescope. Heterodyne receivers mix the signals with a tunable local oscillator and thus convert the astronomical signal to a lower-frequency band. Modern receives allow us to detect wide frequency range simultaneously.
The noise appearing in the observed spectra depends mainly on the receiver and atmospheric noise. It

can be reduced by increasing the integration time. The noise from the whole system is proportional to the system temperature, T_{sys}. Thus, the observational noise for an integration time t and a frequency bandwidth $\Delta\nu$ is given by the radiometer formula:

$$\Delta T = \frac{T_{sys}}{\sqrt{\Delta\nu t}} \quad . \tag{2.23}$$

The ability of a telescope to separate two closely-spaced sources is called angular resolution and it is limited by diffraction. If a telescope has a dish with a circular aperture, the angular resolution (θ in radians) of this telescope can be determined by

$$\theta \approx 1.22\frac{\lambda}{D}, \tag{2.24}$$

where λ is the wavelength of the radiation, D is the diameter of the main collecting dish (both in centimeters or meters). The angle θ is equal to the half power beam width (HPBW) in case of a Gaussian beam profile.
The observed sky is convolved by the beam during the observation. The beam consists of a main beam which is offen approximated by a Gaussian, plus sidelobes at wider angles. If the source is smaller than the main beam and is a hypothetical Gaussian-like source with a full width at half-maximum (FWHM) σ, the beam dilution is given by the beam filling factor

$$f = \frac{\sigma^2}{\theta^2 + \sigma^2}. \tag{2.25}$$

To remove the influences from the atmosphere and the receiver bandpass, the signals need to be calibrated by subtracting the reference measurements taken at the positions different from the ones of the sources. Observations are differential measurements made by either slewing to emission free reference positions or by using the wobbling secondary if one observes a compact source (Wilson et al. 2000).

2.2.2 Interferometry

The size for single-dish telescopes is limited and therefore interferometers are used to reach high angular resolution. By combining the signals detected with individual antennas, observations with a large telescope that contains gaps in its aperture can be simulated. Instead of the diameter, the largest distance between antennas (longest baseline) determines the angular resolution in equation (2.24).
The signal from the sky received by one antenna is correlated with those received by other antennas, after applying the appropriate corrections for the geometric and instrumental phase delays. Instead of detecting the direct radiation from the sources, the interference patterns (fringes), which depend on the baselines and the radiation and structures of the sources, are recorded with interferometer observations. During the observations, different pairs of antennas have different spatial sensitivities formulated as $\theta_{ij} \sim \lambda/B_{ij}$. Here θ_{ij} and B_{ij} are the spatial resolution and the lengths of the baseline (distances) for a given antenna pair ij. As the Earth rotates, θ_{ij} changes due to projections of the baselines. The outputs of the different correlations with different projections form a spatial sampling in Fourier space (u, v plane).
In principle, telescope configurations with large and small uv-distances can probe signals from small and large scales, respectively. However, unlike a single-dish telescope which has complete sampling from the very inner area up to a maximum scale (limited by the size of its diameter), an interferometer has an

Table 2.1. Details of the observed HDO transitions

Frequency (GHz)	Transition	E_{up} (K)	n^a_{cr}(para-H_2) (cm^{-3})	n^a_{cr}(ortho-H_2) (cm^{-3})
80.578	$1_{1,0}$–$1_{1,1}$	46.8	2.23×10^7	2.23×10^7
225.897	$3_{1,2}$–$2_{2,1}$	167.7	9.91×10^7	2.20×10^7
241.561	$2_{1,1}$–$2_{1,2}$	95.3	3.53×10^7	8.78×10^6
266.161	$2_{2,0}$–$3_{1,3}$	157.2	1.21×10^9	2.93×10^8
464.924	$1_{0,1}$–$0_{0,0}$	22.3	1.71×10^6	3.69×10^5
827.263	$4_{1,3}$–$3_{2,2}$	263.3	2.44×10^8	5.17×10^7
848.962	$2_{1,2}$–$1_{1,1}$	83.6	1.89×10^8	4.29×10^7
893.639	$1_{1,1}$–$0_{0,0}$	42.9	5.72×10^7	1.47×10^7

[a] Critical density at 100 K calculated by using the values of the Einstein coefficient and the collision rates tabulated for HDO (Faure et al. 2012) in the LAMDA database (http://www.strw.leidenuniv.nl/moldata/).

incomplete uv-coverage. Especially the inner uv-sampling, which corresponds to large spatial scales, is missing. Interferometers thus cannot detect the signals coming from the scales larger than the ones set by the shortest baselines. This is the so-called "missing flux" problem. In other words, the interferometers are blind to the emission from the (very) extended structures of the sources. Because the uv-data (visibility data) are the real output from interferometers, to obtain the images of observed sources, we need to perform Fourier transformation of the visibility and subsequent image processing which involves deconvolution to reconstruct the true sky intensity distribution (Thompson et al. 2008).

2.3 Radiative transfer modeling

Solving the equation of radiative transfer to investigate the environment where the molecules exist is not simple because it needs proper assumptions of many physical conditions of the source, such as density and temperature. Nevertheless, some basic quantities, such as excitation temperature T_{ex} and total molecular column density N_{tot}, can be estimated by analyzing the molecular line intensities without solving the radiative transfer equation. The most straightforward and common method is rotation diagram analysis, which is used in this thesis and assumes that the lines are optically thin and in local thermodynamic equilibrium (LTE) (Goldsmith & Langer 1999). Over the past few decades, the collisional-rate coefficients of many molecules have been computed (e.g. Offer et al. 1994; Daniel et al. 2005; Dayou & Balança 2006; Faure & Josselin 2008; Dubernet et al. 2009; Daniel et al. 2011; Faure et al. 2012) and radiative transfer codes developed. These advances allow us to create models and compare their predicted radiation to the observational data.

Sections. 2.3.1 presents the radiative transfer code RATRAN, which is used to compute the molecular and dust radiation. In Sections. 2.3.2 I discuss how to compare models and real data.

2.3.1 RATRAN

To analyze the HDO data, we used the 1 D Monte Carlo code RATRAN, developed by Hogerheijde & van der Tak (2000). This code calculates the excitation and radiative transfer for molecular lines and it determines the level populations by using an accelerated Monte Carlo method. Detailed information including the code itself and manual can be found at the website, https://personal.sron.nl/ vdtak/ratran/frames.html. There are two parts in this code: AMC and SKY. AMC computes the level population based on the physical source profiles and SKY uses the AMC results with ray-tracing to reproduce the output radiation of the source (source map). The input source model (physical profiles in different shells) is spherically symmetric and the required molecular data file is taken from the LAMDA database (http://home.strw.leidenuniv.nl/∼moldata/).
AMC consists of two steps. In the first step, the program lets a group of random rays propagate through the source and then iterates the populations until the required accuracy is achieved. Then, the code repeats this procedure with rays from various directions (second step). The amount of photons is doubled, until the populations and the radiation are consistent. In the optically thick case, the procedure is accelerated by treating local contributions to the radiation field.
SKY solves the radiative transfer equation along the line-of-sight for each cell continuously from the back to the front. This progress is repeated for all pixels in the sky plane. The code computes one line at a time based on the frequency-dependent opacity and source function, which are known from the temperature, the dust opacity and the level populations.

2.3.2 Comparison of Model and Data

The output of the radiative transfer code finally produces the simulated synthetic radiation from the source, including continuum and line emission/absorption. In order to compare modeled results with the observational data, we need to modify the synthetic data. In this thesis, we mainly use the astronomical software MIRIAD to do this. For single-dish observations, the synthetic data first have to be convolved with the telescope beam, which is usually approximated as a Gaussian with the width obtained from equation (2.24). Then the modeled spectra are reprojected to the position where the telescope pointed.
For comparison with the interferometer data, mock observations are generated from the modeled data with the steps below. The values of the real observed parameters, such as epoch, rest frequency, and the coordinate of the observed reference position, are inserted into the blank header of the modeled data. After that, the modeled image is multiplied by the interferometer primary beam. Afterward, the (u,v) sampling retrieved from the real interferometer data is applied to the modeled image and then the resulting (u,v) data are inverted to obtain the simulated maps/spectra.
Because the judgment made by eye in comparing the overlaid spectra is subjective, computing the χ^2 is adopted in thesis to estimate the goodness of the fits. In order to model the line velocity profiles, the definition of χ^2 is $\Sigma \frac{(T_{mb,ob} - T_{mb,mod})^2}{\sigma^2}$, where the sum is taken over the channels in the spectrum. The σ within this χ^2 analysis includes the statistical errors and uncertainties in flux calibration, but does not include any uncertainty in the adopted collisional rate coefficients used in the excitation calculation (Faure et al. 2012).

Chapter 3

Water deuterium fractionation in the low-mass protostar NGC1333-IRAS2A

Sections 3.1 to 3.5 appeared in Astronomy & Astrophysics: Liu, F.-C., Parise, B., Kristensen, L., et al. 2011, A&A, 527, A19 (Received 3 August 2010 / Accepted 22 October 2010)

3.1 Introduction

Molecular deuteration has been the focus of many studies. The abundance of deuterated molecules has been shown to be significantly increased in low-temperature environments, compared to the D/H elemental ratio in the interstellar medium ($\sim 1.5\times10^{-5}$, Linsky 2003). Over the last decade, very high D/H ratios in several molecules have been found in low-mass protostars, e.g. D_2CO/H_2CO=0.05 (Ceccarelli et al. 1998) and CD_3OH/CH_3OH=0.01 (Parise et al. 2004) toward IRAS 16293-2422. This can be interpreted in terms of the chemical formation pathways of these molecules – both are believed to be grain surface products in cold dark clouds through the formation process of successive CO hydrogenation (Parise et al. 2006). Because water is the main constituent of grain mantles, studies have been performed to investigate if deuterium enrichment of water is similar to the fractionation of formaldehyde and methanol. Several HDO transitions have been observed toward IRAS 16293−2422, and were modeled to derive the HDO abundance profile in its envelope (Parise et al. 2005a). Using the H_2O abundance profile as derived from ISO observations (Ceccarelli et al. 2000), the HDO/H_2O ratio was found to be ~ 0.03 in the inner hot corino, and <0.002 in the cold outer envelope (Parise et al. 2005a), i.e. significantly lower than the formaldehyde and methanol fractionation in the same source. A search for HDO ices in low-mass sources with large fractionation of formaldehyde and methanol found no HDO ices to a very low limit (Parise et al. 2003, $HDO/H_2O < 0.01$ in ices), which might be surprising if all species formed simultaneously on dust surfaces. Studying the abundance and distribution of HDO in low-mass prestellar envelopes is moreover an essential astrochemical goal, as it would provide the early conditions from where comets form. The HDO/H_2O ratio has been measured in several comets and found to be $\sim 3\times10^{-4}$ (Balsiger et al. 1995; Bockelée-Morvan et al. 1998; Meier et al. 1998). Up to now, the HDO emission has been studied in detail only in one low-mass protostar (IRAS 16293−2422, Parise et al. 2005a). A radiative transfer analysis of HDO emission has shown that the abundance profile of HDO can be constrained in low-mass protostellar

Table 3.1. Parameters of the HDO observations

Telescope	Transition	Frequency GHz	E_{up} K	Beam $''$	B_{eff}	rms[b] mK	Resolution km/s	T^b_{peak} mK	Δv km/s	$\int T_{mb}$dv K km/s
NGC1333-IRAS2A										
IRAM	$1_{1,0}$–$1_{1,1}$	80.578	46.8	31.2	0.78	11.6	0.15	17.8	3.9±1.1	0.07±0.02
IRAM	$3_{1,2}$–$2_{2,1}$	225.897	167.7	11.1	0.57	24.7	0.10	113.5	4.2±0.3	0.50±0.03
IRAM	$2_{1,1}$–$2_{1,2}$	241.561	95.3	10.4	0.46	30.8	0.19	98.6	4.1±0.5	0.43±0.05
JCMT	$1_{0,1}$–$0_{0,0}$	464.924	22.3	10.8	0.44[a]	125	0.20	305.8	6.2±0.8	2.00±0.23
APEX	$1_{1,1}$–$0_{0,0}$	893.639	42.9	7.0	0.35	210	0.25	...	...	...
Outflow-position										
IRAM	$1_{1,0}$–$1_{1,1}$	80.578	46.8	31.2	0.78	11.5	0.15	...	...	$\leq$0.03[c]
IRAM	$3_{1,2}$–$2_{2,1}$	225.897	167.7	11.1	0.57	21.1	0.10	...	...	$\leq$0.04[c]
JCMT	$1_{0,1}$–$0_{0,0}$	464.924	22.3	10.8	0.44[a]	241	0.20	...	...	$\leq$0.72[c]

[a] Values as observed on Jupiter during the second semester of 2004 with the RxW-C receiver.
[b] T_{mb} scale.
[c] 3σ upper limit of integrated flux with assumption that Δv is 5 km/s.

envelopes by means of the analysis of several HDO lines, spanning different energy conditions (Parise et al. 2005b). Now that the $Herschel$ telescope is delivering its first data, which allows us to get a better measure of the water abundance profile in protostars, the time is ripe to study water fractionation in these environments. Here we present the modeling of HDO observations toward a second solar-type Class 0 protostar, NGC1333-IRAS2A (IRAS2A). In Section 2 we present the observations and first results, in Section 3 we present the radiative transfer modeling, and discuss the results in Section 4. We finally conclude in Section 5.

3.2 Observations and results

3.2.1 The source

IRAS2A is a solar-type Class 0 protostar located in the NGC 1333 molecular cloud. The adopted distance of IRAS2A is 235 pc (Hirota et al. 2008). Deuterium fractionation of formaldehyde and methanol in the envelope has been studied by Parise et al. (2006). The deuterium enrichments ($HDCO/H_2CO \sim 0.17$ and $CH_2DOH/CH_3OH \sim 0.62$) are higher than in IRAS 16293-2422 (Parise et al. 2004).
The H_2O line emission in IRAS2A was recently observed with the *Herschel* telescope (Kristensen et al. 2010b).

3.2.2 Observations

Observations were carried out at three different telescopes. Using the IRAM 30m telescope, we observed the 80, 225, and 241 GHz lines (see Figure 3.1) toward IRAS2A, at position α_{2000}=$03^h28^m55^s.60$ and δ_{2000}=$31^o14^m37^s.00$, on 2004 Nov. 26 under PWV $\sim$2mm. The focus was checked on Uranus, and the local pointing on 0333+321, leading to an uncertainty in the pointing of less than 3″ (rms). We used the wobbler switching mode, with a throw of 90″. Typical system temperatures varied in the range 115–150 K at 80 GHz, 240–310 K at 225 GHz, and 375–525 K at 241 GHz. During a second IRAM run, we observed an offset position relative to the source, to check for a possible contribution of the outflow. We targeted the 80GHz and 225GHz lines on 2005 Apr. 9, toward the position α_{2000}=$03^h29^m01^s.00$ and δ_{2000}=$31^o14^m20^s$.

The 464 GHz observations were retrieved from the JCMT archive (project M04BN06). The $1_{0,1}$-$0_{0,0}$ line was observed toward the position of IRAS2A as well as toward the outflow on 2004 Sep. 27, under an opacity $\tau_{225\,\mathrm{GHz}}$=0.05.The 893 GHz line was observed using the CHAMP$^+$ multi-pixel receiver on APEX in Sep. 2008. The central pixel was centered on position α_{2000}=$03^h28^m55^s.40$ and δ_{2000}=$31^o14^m35^s.00$. Local pointing was checked in CO(6-5) on IK-Tau. We used the wobbler symmetric switching mode, with a throw of 120″, resulting in OFF positions at 240″ from the source. The total integration time is 95 minutes. The CO(6-5) line, observed in parallel on the 650 GHz receiver, is clearly detected with a peak T_A^* of order of 3 K, and is presented in Kristensen et al. (2010b).

Table 3.1 lists the characteristics of the HDO observations. The unit of flux here was converted from T_A^* to T_mb using the beam efficiencies indicated in the Table, which we took from the IRAM[1] and JCMT[2] websites. The beam efficiency for CHAMP$^+$ was measured in Oct. 2007 on Mars.

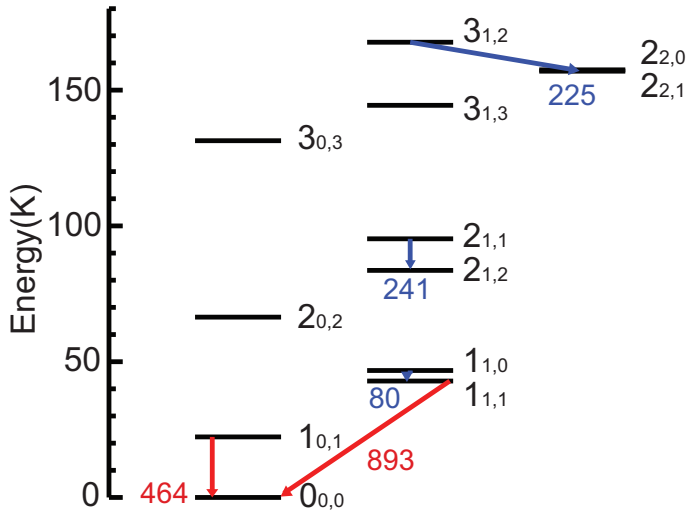

Figure 3.1 HDO energy levels. The transitions that were observed in this work are marked with arrows (frequency in GHz).

[1] http://www.iram.es/IRAMES/telescope/telescopeSummary/telescope_summary.html
[2] http://www.jach.hawaii.edu/JCMT/spectral_line/Standards/beameff.html

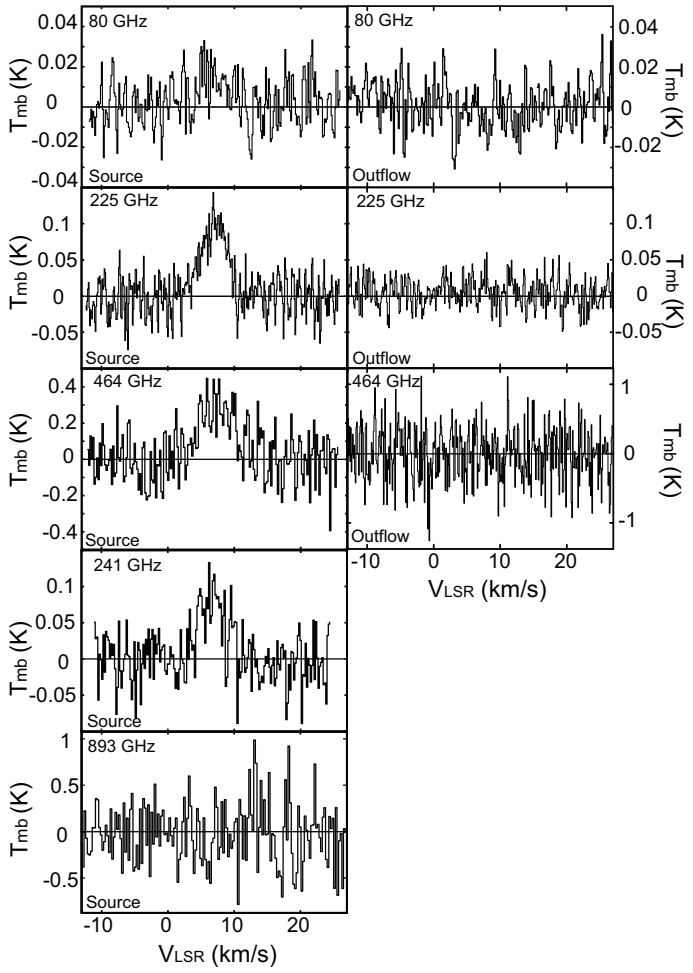

Figure 3.2 Observed HDO spectra. The words in the lower left side of each spectrum indicate the observed position: source (on source) and outflow (offset-position).

3.2.3 Results

The spectra observed toward IRAS2A and the offset outflow position are presented in Figure 3.2. The transitions from 80 GHz to 464 GHz are detected on-source, while we only have an upper-limit for the second ground transition, at 893 GHz. No line is detected at the offset position (see Table 3.1 and Figure 3.2).

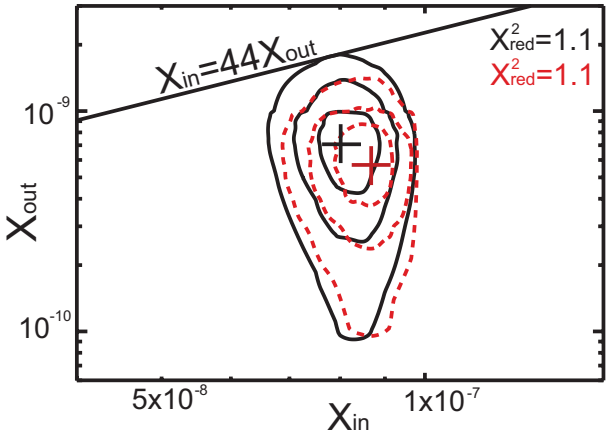

Figure 3.3 x_{in}^{HDO} and x_{out}^{HDO} contours (1, 2 and 3σ) for the χ^2_{red} for the different central star mass (M_*). The black-solid and red-dashed lines indicate the contours of $M_* = 0.07$ $M_\odot$ and $M_* = 0.15$ $M_\odot$. The symbols "+" correspond to the best-fit model of each case.

3.3 Modeling

Because no emission is detected at the targeted outflow position, we use an envelope model to fit the observational results, excluding any possible contribution of outflows or shocks. To analyze the HDO data, we used the 1D Monte Carlo code, RATRAN, developed by Hogerheijde & van der Tak (2000). The adopted density, opacity, and temperature profiles are derived with the 1D DUSTY code (Ivezić & Elitzur 1997) following the procedure of Jørgensen et al. (2002) (Yıldız et al. 2010). In addition, we assumed the free-fall velocity field, $v = (\frac{2GM_*}{r})^{\frac{1}{2}}$ and adopted the somewhat arbitrary values for the central mass, $M_* = 0.07$ and 0.15 $M_\odot$, consistent with the low mass inferred for the central object by Brinch et al. (2009). We will discuss this choice in Section 4.1. The emission was modeled in terms of a jump model, where the fractional abundances of deuterated water, relative to H_2, in the inner part of the source ($T > 100$ K, assumed evaporation temperature) and in the outer part ($T \leq 100$ K) are two free parameters, x_{in}^{HDO} and x_{out}^{HDO}, respectively. We performed an χ^2 analysis for x_{in}^{HDO} ranging from 1×10^{-10} to 2×10^{-7} and for x_{out}^{HDO} ranging from 9×10^{-12} to 5×10^{-8}. Contrarily to the study by Parise et al. (2005a), who only modeled the integrated flux of HDO lines, we here intend to model as well the line velocity profiles. In order to get a higher signal-to-noise ratio and a consistent weighting of each spectra, we smoothed the observed spectra to similar resolutions between 0.4 – 0.6 km/s. The χ^2 was then computed on the profile of these smoothed spectra. Here the definition of χ^2 is $\Sigma\frac{(T_{mb,ob}-T_{mb,mod})^2}{\sigma^2}$, where the sum is over each channel in each spectrum. The parameters of the fits and their results are

Table 3.2. Fitting parameters and their results

Central star mass[a] ($M_\odot$)	Doppler parameter b[a] (km/s)	Best fit HDO abundances inner region	outer region	$\chi^2_{\rm red}$	HDO abundances confidence interval (3σ) inner region	outer region
0.07	2.0	8.0×10^{-8}	7.0×10^{-10}	1.1	6.6×10^{-8}–1.0×10^{-7}	9×10^{-11}–1.8×10^{-9}
0.15	1.0	8.6×10^{-8}	5.5×10^{-10}	1.1	6.8×10^{-8}–1.1×10^{-7}	9×10^{-11}–1.5×10^{-9}

[a] Fixed parameters.

listed in Table 3.2. The σ within this χ^2 analysis includes the statistical errors and uncertainties in flux calibration ($\sim$20%), but does not include any uncertainty in the adopted collisional rate coefficients used in the excitation calculation (Green 1989). The black-solid and red-dashed lines in Fig. 3.3 present the contours delimitating the 1σ (68.3%), 2σ (95.4%) and 3σ (99.7%) confidence intervals. These contours are derived with the method described in Lampton et al. (1976), who shows that the $\Delta S = \chi^2 - \chi^2_{\rm min}$ random variable follows a χ^2 distribution with p variables, p being the number of parameters. Here p=2 (X_{in} and X_{out}), so that these contours correspond to $\chi^2 = \chi^2_{\rm min}$+2.3, $\chi^2_{\rm min}$+6.17 and $\chi^2_{\rm min}$+11.8. Here we use "1σ", "2σ", and "3σ" in analogy with gaussian-distributed random variables.

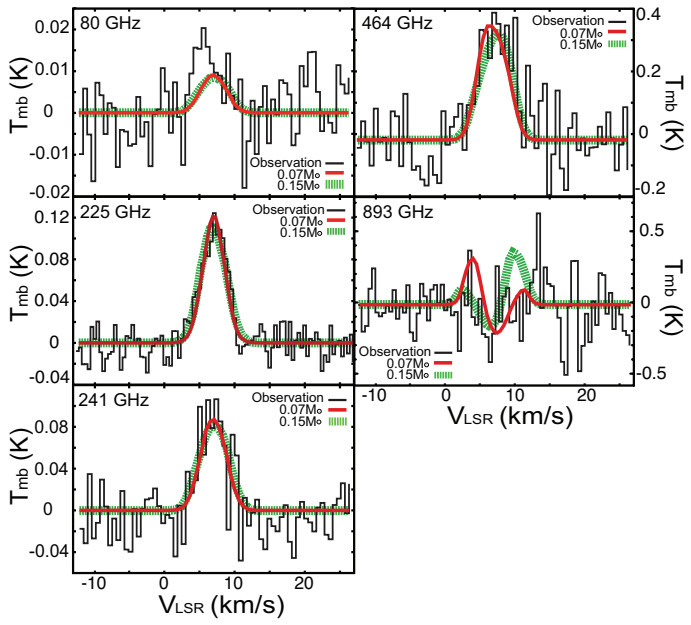

Figure 3.4 Comparison of the observed spectra smoothed to 0.4 – 0.6 km/s spectral resolution with the results of our best-fit models for two different masses of the central protostar. The observed line emission is shown in black lines in each spectrum. The red and green lines show the results of the models with the assumptions that M_* is 0.07 $M_\odot$ and 0.15 $M_\odot$, respectively.

The obtained minimum $\chi^2_{\rm red}$ is not far from 1, which indicates that the model assuming a simple collaps-

ing envelope is a reasonable description of the data. The inner and outer fractional abundance is well constrained by our data at the 3σ level. The smoothed spectra are overlaid with the modeling results of the best fit with two different central-star masses in Fig. 3.4.

3.4 Discussion

The first results of our model are that the observations are well described by the adopted envelope model, and that the HDO abundance profile displays a jump by two orders of magnitude between the cold and the warm envelope for the best fit. Below we first discuss the choice of the velocity field and the Doppler b-parameter, which is the turbulence broadening.

3.4.1 The high turbulence broadening

Although the minimum $\chi^2_{\rm red}$ value shows that the simplest model (i.e. an infalling envelope) describes our data well, the required turbulence broadening b of 2 km/s may seem unrealistically high for the best model (M=0.07 $M_\odot$). We note however that this b parameter is degenerate within the noise of our observations with the choice of the free-fall velocity profile in the envelope. Indeed, increasing the central mass (which is anyway mainly unconstrained) to 0.15 $M_\odot$ allows us to reproduce the linewidths with a significantly lower $b = 1$ km/s. The minimum $\chi^2_{\rm red}$ in this case is the same as the model with central mass 0.07 $M_\odot$, and the $x_{\rm in}^{\rm HDO}$ and $x_{\rm out}^{\rm HDO}$ of the best fit model are 8.6×10^{-8} and 5.5×10^{-10}, which are still within the 1σ of previous results (Fig. 3.3). This shows that the constraints on $x_{\rm in}^{\rm HDO}$ and $x_{\rm out}^{\rm HDO}$ do not depend much on the chosen velocity profile, and that the turbulence is barely constrained in the models.

3.4.2 The fractional abundance of HDO

The low value of $\chi^2_{\rm red}$ = 1.1 for the best-fit model shows that the assumption of a jump profile for the abundance in a spherical envelope is appropriate to fit our data. The abundance of HDO jumps by at least a factor of 44 at the 3σ confidence level (see Fig. 3.3). Ices are therefore shown to evaporate from the grains in the inner part of the envelope in IRAS2A. This property has also been shown on HDO and H_2O in IRAS 16293-2422 (Parise et al. 2005a; Ceccarelli et al. 2000). Moreover, the best-fit HDO abundances of the two cases are also similar to the values of HDO fractional abundances in IRAS 16293-2422 (see Table 3.3). This suggests that the mechanisms to form HDO could be the same in both these solar-type class 0 protostars, even if the two sources are located in different star-forming regions (Perseus v.s. Ophiuchus), and that the case of IRAS 16293-2422 is not peculiar. The present study provides the second detailed multi-transition HDO analysis toward a low-mass protostar, and the study of a greater number of sources would be essential to generalize this result.

3.4.3 Water deuterium fractionation in low-mass protostars

In order to derive the HDO/H_2O ratio in the IRAS2A envelope, we need to infer the H_2O abundance profile in the quiescent envelope. Figure 3.5 compares the spectra of the 225 HDO line and the 987 H_2O line (Kristensen et al. 2010). Both the total water emission and the emission where the broad outflow Gaussian component was removed are shown. In this figure we multiplied the intensity of 225 HDO

Table 3.3. Comparison of HDO fractional abundance between NGC1333-IRAS2A and IRAS 16293-2422

Source	best fit		confidence interval (3σ)		$\frac{\text{HDO}}{\text{H}_2\text{O}}$		$\frac{\text{HDCO}}{\text{H}_2\text{CO}}$ [b]	$\frac{\text{CH}_2\text{DOH}}{\text{CH}_3\text{OH}}$ [b]
	x_{in}^{HDO}	x_{out}^{HDO}	x_{in}^{HDO}	x_{out}^{HDO}	Inner	outer (3σ)	—	—
IRAS2A[a]	8×10^{-8}	7×10^{-10}	6.6×10^{-8}–1.0×10^{-7}	9×10^{-11}–1.8×10^{-9}	≥ 0.01[c]	$0.07^{+0.11}_{-0.06}$[c]	$0.17^{+0.12}_{-0.08}$	$0.62^{+0.71}_{-0.33}$
IRAS 16293[d]	1×10^{-7}	1.5×10^{-10}	7×10^{-8}–1.3×10^{-7}	$\leq 1.0 \times 10^{-9}$	0.03	≤ 0.002	0.15±0.07	$0.37^{+0.38}_{-0.19}$
Orion KL	...	...	...	...	0.02[e]		0.14[f]	0.04[g]

[a]The HDO fractional abundance was derived with M=0.07 $M_\odot$.

[b]Parise et al. (2006)

[c]The fractional abundances of water taken here are $x_{in}^{H_2O} \leq 1 \times 10^{-5}$ and $x_{out}^{H_2O} = 1 \times 10^{-8}$, as constrained by Visser et al. in prep. from the $1_{11} - 0_{00}$, $202 - 111$, and $2_{11} - 2_{02}$ $H_2^{16}O$ lines and the upper-limit on the $1_{11} - 0_{00}$ $H_2^{18}O$ line presented in Kristensen et al. (2010).

[d]Parise et al. (2005a) [e]Bergin et al. (2010) [f]Turner (1990) [g]Jacq et al. (1993)

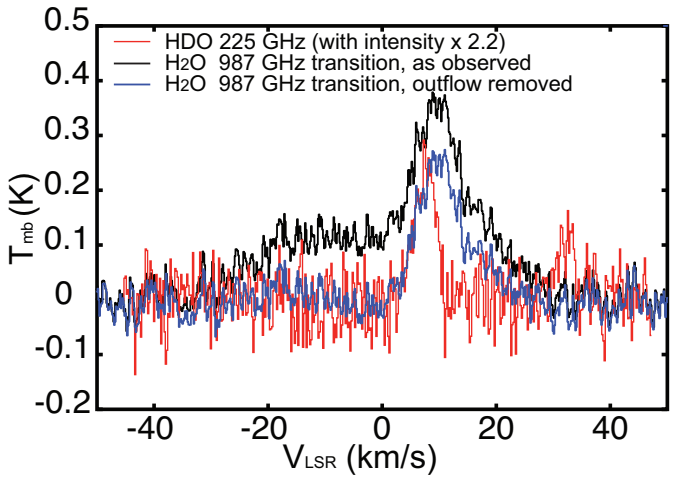

Figure 3.5 Comparison of the HDO emission with H_2O emission with/without wing. The red line indicates the emission line of the HDO transition at 225 GHz . The black and blue line show the line emission of the H_2O transition at 987 GHz with and without outflow component. The H_2O data are taken from Kristensen et al. (2010b).

line with a factor of 2.2 to compare it with the H_2O emission. Obviously the H_2O line is broader than the HDO line (FWHM = 9.5 km s^{-1} versus up to 6 km s^{-1} for HDO), even where the broad outflow component was removed. This medium-broad component has been interpreted to come from small-scale shocks because of the interaction of the jet and wind with the dense inner envelope on scales of $\sim 1''$ (Kristensen et al. 2010b). In addition, the H_2O emission from the warm inner envelope was suggested to be optically thick (Kristensen et al. 2010b). Therefore, the H_2O lines do not probe the quiescent envelope and HDO lines may not probe the same gas.

To obtain upper limits on the quiescent H_2O abundance, Visser et al. in prep. used deep integrations on various $H_2^{18}O$ lines presented by Kristensen et al. (2010). The non-detection of narrow $H_2^{18}O$ features limits the inner H_2O abundance to $\lesssim 10^{-5}$, whereas the presence of narrow deep H_2O self-absorption gives an outer H_2O abundance of $\sim 10^{-8}$.

The values of the HDO/H_2O ratio within the present constraints are listed in Table 3.3. The HDO/H_2O ratios in the inner warm and the outer cold envelope are found to be more than 1% and are in the range of 0.9%–18% (3σ). The D/H ratio of water in the outer envelope is roughly one order of magnitude lower than the ratio of methanol, which confirms the trend measured in IRAS 16293−2422. Obviously, better constraints on the H_2O abundances in the inner warm envelope are required to see if the deuterium enrichment in water is significantly lower than in methanol. On the other hand, the similar HDO/H_2O ratio and the one order magnitude higher CH_2DOH/CH_3OH ratio of IRAS2A and Orion KL suggest that the environment plays a role in the chemistry.

The HDO/H_2O ratio in the inner envelope is found to be more than one order of magnitude higher than the ratio measured in comets, as for IRAS 16293−2422. If this high deuterium enrichment of water is typical of low-mass protostellar envelopes, and if the HDO/H_2O ratio measured in the cometary coma is representative of the cometary ice composition, then this would imply that the deuterium fractionation of water is reprocessed at some point between the protostellar envelope and the cometary ice. Reprocessing of the gas in the hot corino warm environment is expected to reduce the deuterium fractionation on

typical timescales of 10^5 yrs in environments of density $\sim 10^6$ cm^{-3} (Charnley et al. 1997). However, in this case, re-condensation of the gas on the grains would be required. Isotopologue exchanges are also possible at the surface of the grains (see e.g. Ratajczak et al. 2009), without requiring evaporation. This may however not be enough to deplete the deuterium level in water, because water is the main component of water ices. A mechanism to get rid of deuterons from the grain surface would need to be invoked. Because of the high abundance of water, this mechanism should involve efficient exchange reactions. A suggestion would be to study in the laboratory the possibility of deuteron exchange between HDO and H_2 at the grain surfaces.

Improving the observational constraints on the HDO/H_2O ratio in protostellar envelopes is essential to allow us to understand the implications in terms of chemical evolution in the protosolar nebula. Figure 3.6 shows the RATRAN modeling prediction for two $H_2^{18}O$ lines, for a set of reasonable water abundances. We made the assumption that the standard ortho/para ratio is 3 and the $^{18}O/^{16}O$ ratio is 2.05×10^{-3}. Figure 3.6b shows that the $H_2^{18}O$ 1189 GHz line emission is much more sensitive to the inner fractional abundance of water than the $H_2^{18}O$ 1101 GHz line. This line is therefore a good candidate to target with the *Herschel* telescope to further constrain the inner water abundance.

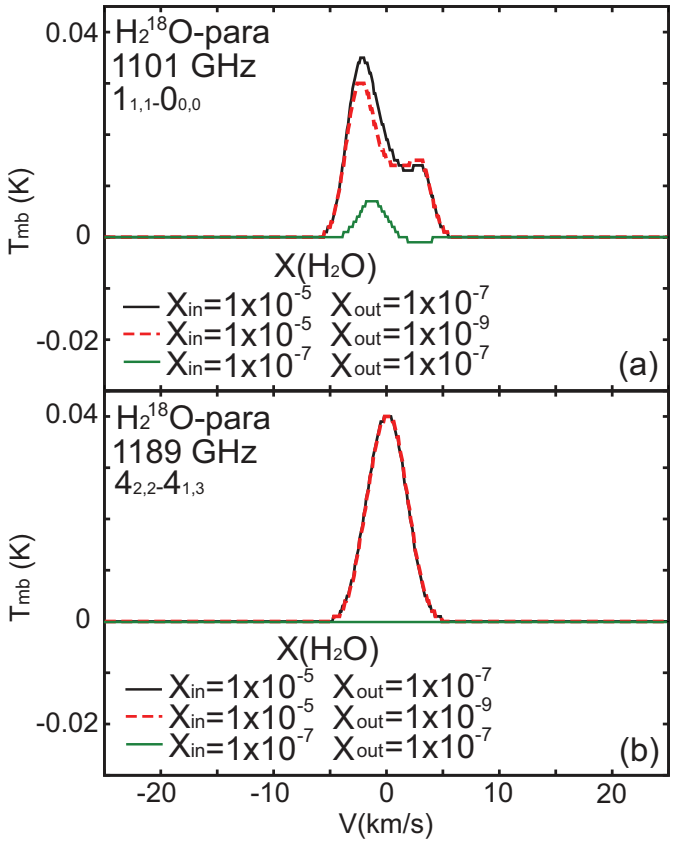

Figure 3.6 Model predictions for the chosen $H_2^{18}O$ lines. X_{in} and X_{out} represent the water (H_2O) abundance in the inner warm ($>$ 100 K) and outer cold ($\leq$ 100 K) envelope. A standard ortho/para ratio of three was assumed.

3.5 Conclusion

We presented the observation of five HDO lines toward the solar-type class 0 protostar NGC1333-IRAS2A using the IRAM 30m, JCMT and APEX telescope. Four of them are clearly detected, while the second ground-state transition line at 893 GHz is not. Because there are no detections at the outflow position at 80, 225, and 464 GHz, we assumed for the modeling that most emission comes from the envelope.

We modeled the emission with the RATRAN radiative transfer code, assuming a step profile for the HDO abundance. We derived the HDO abundance in the inner and outer parts of the envelope to be $x_{\rm in}^{\rm HDO} = 8 \times 10^{-8}$ and $x_{\rm out}^{\rm HDO} = 7 \times 10^{-10}$. This result shows that the HDO abundance is enhanced in the inner envelope because of the ices' evaporation from the grains, as for IRAS 16293-2422. Moreover, the values are similar to those in IRAS 16293-2422, which suggests that the pathway of the formation of HDO is the same in low-mass class 0 protostars. The study of a larger sample of sources is needed to generalize this result.

The HDO/H_2O abundance ratio is found to be $>1\%$ in the inner envelope. A better constraint on the H_2O abundance in the inner envelope is required to derive the deuterium enrichment in the warm envelope.

Chapter 4

Water deuterium fractionation in the high-mass hot core G34.26+0.15

Sections 4.1 to 4.6 and A.1 to A.3 appeared in Astronomy & Astrophysics: Liu, F.-C., Parise, B., Wyrowski, F., Zhang, Q., & Güsten, R. 2013, A&A, 550, A37 (Received 27 June 2012 / Accepted 9 November 2012)

4.1 Introduction

In the past decades, the abundance of deuterated molecules has been shown to be significantly enhanced in low-temperature environments (e.g. Snell & Wootten 1977; Wootten et al. 1982; Roueff et al. 2000; Loinard et al. 2001) compared to the D/H elemental ratio in the interstellar medium ($\sim 1.5 \times 10^{-5}$, Linsky 2003). The level of deuterium fractionation of molecules is a potentially good tracer of their formation process. This characteristic was demonstrated and used to infer chemical routes of formation for, e.g., methanol (Parise et al. 2004, 2006) and ammonia (Roueff et al. 2005).

Water is an important molecule, because it is the main constituent of grain mantles and an essential molecule in the oxygen chemistry in dense interstellar clouds. It can be formed by three mechanisms: dissociative recombination in gas phase by ion-molecule chemistry (Bergin et al. 2000), combination of atoms on the surface of cold dust grains at low temperature (Tielens & Hagen 1982; Cuppen et al. 2010), and gas phase reaction at high temperature (> 250K) (Wagner & Graff 1987; van der Tak et al. 2006). To constrain the formation process of water, studying the D/H ratio of water is a promising method, because the three scenarios would result in different fractionation.

The D/H ratio of water has been studied toward several hot-cores (Jacq et al. 1990; Pardo et al. 2001; van der Tak et al. 2006) and low-mass protostars (Parise et al. 2005a; Liu et al. 2011). The studies of the high-mass hot cores, Orion IRc2 and AFGL 2591, and the low-mass protostars, IRAS16293-2422 and NGC1333-IRAS2A, suggest that the HDO emission mainly originates in the envelope and with different HDO/H_2O ratios in the two different environments ($\sim 10^{-2}$ for low-mass cases and $\sim 10^{-4}$ for high-mass cases). In addition, the D/H ratios of water are significantly lower than the formaldehyde and methanol fractionation in the same sources (Parise et al. 2006; Turner 1990), which might be surprising if all species formed simultaneously on dust surfaces. This low deuterium enrichment of water, if confirmed, is a very

Table 4.1. Details of the APEX HDO observations toward G34.26+0.15

Frequency GHz	Transition	E_{up} K	n^a_{cr}(para-H_2) cm^{-3}	n^a_{cr}(ortho-H_2) cm^{-3}	HPBW $''$	$B_{\rm eff}$	T_{sys} K	dv^b km/s	Receiver
225.897	$3_{1,2}$–$2_{2,1}$	167.7	1.19×10^8	2.65×10^7	28	0.75	196–210	0.16	APEX-1
241.561	$2_{1,1}$–$2_{1,2}$	95.3	4.00×10^7	1.03×10^7	26	0.75	218–235	0.15	APEX-1
266.161	$2_{2,0}$–$3_{1,3}$	157.2	1.53×10^9	3.36×10^8	24	0.75	249–261	0.14	APEX-1
464.924	$1_{0,1}$–$0_{0,0}$	22.3	1.61×10^6	3.74×10^5	14	0.53	498–528	0.08	PI460
893.639	$1_{1,1}$–$0_{0,0}$	42.9	5.64×10^7	1.44×10^7	7	0.36	2656–3685	0.12	CHAMP$^+$

[a] Critical density at 100 K calculated with the values of the Einstein coefficient and the collision rates tabulated for HDO (Faure et al. 2012) in the LAMDA database (http://www.strw.leidenuniv.nl/moldata/).

[b] The velocity resolution of the original settings in the observations.

valuable constraint for astrochemical models that strive to explain the chemical processes involved in the formation of water.

Previous studies have shown that the distribution of the HDO abundance can be constrained in low-mass protostellar envelopes with the radiative transfer analysis of several HDO lines, which span different energy conditions (Parise et al. 2005b; Liu et al. 2011).

While some detailed studies that also involve the ground transitions of HDO have recently been performed toward low-mass star-forming regions (Parise et al. 2005a; Liu et al. 2011; Coutens et al. 2012), most of the water fractionation studies in high-mass hot cores were performed more than ten years ago, when the submillimeter spectrum was still extremely difficult to observe. Thanks to the advance of sensitive submillimeter receivers, such as those on the APEX telescope, and to the launch of Herschel, it is now possible to carry out much more detailed radiative transfer analyses of HDO and H_2O. We aim here to carry out such a detailed study on one massive protostellar object, G34.26+0.15, to constrain the formation of water in a high-mass hot core.

G34.26+0.15 is a well-studied hot core associated with an ultra-compact HII region. The HDO/H_2O ratio has been derived to be 1.1×10^{-4} toward this source from the analysis of one HDO and one H_2O transition line (Gensheimer et al. 1996). With the five transition lines including the ground-state lines in the submillimeter-wave range (241, 225, 266, 464, and 893 GHz with APEX) and with higher angular resolution observations (241 and 225 GHz with SMA), we can study the HDO abundance and distribution at the core scale. This source was one of the targets of the WISH Key Program (van Dishoeck et al. 2011) with the Herschel telescope, ensuring that information on the abundance of water is available (Wyrowski et al. 2010). This hot core has been the target of molecular line surveys and showed high levels of deuterium fractionation (Hatchell et al. 1998b; Jacq et al. 1990; Gensheimer et al. 1996). The D/H ratios of formaldehyde and HCN toward G34.26 are $\sim$1% and $\sim$0.1% (Roberts & Millar 2007; Hatchell et al. 1998a).

This paper is organized as follows. In Section 2 we present the observations. We present the observational results and the radiative transfer modeling in Sects. 3 and 4. The discussion and conclusion are given in Sects. 5 and 6.

4.2 Observations

4.2.1 Single-dish observations

HDO observations were carried out with the APEX telescope. We observed the 225, 241, 266, 464, and 893 GHz lines (Table 4.1) toward G34.26+0.15 at the hot core position α_{2000}=$18^h53^m18^s.57$ and δ_{2000}=$01^o14^m58^s.3$ in September 2010. The focus was checked on Saturn, and the local pointing on G34.26+0.15 itself. We used the wobbler-switching mode with a throw of 240″. Table 4.1 lists the characteristics of the HDO observations. The temperature scale here was converted from $T_{\rm A}^*$ to $T_{\rm mb}$ using the beam efficiencies indicated in Table 4.1, which we took from the APEX[1] website. The beam efficiency for CHAMP$^+$ was measured in July 2010 on Mars.

4.2.2 Interferometer observations

The observations were carried out on April 26 and May 10, 2011 with the Submillimeter Array (SMA) on Mauna Kea, Hawaii. We used the 230 GHz receivers to observe the 225 and 241 GHz lines as well as the 1.3 mm continuum simultaneously. The primary-beam size (HPBW) of the 6-m-diameter antennas at 230 GHz was measured to be ∼54″. The phase tracking center of this observation is the same as for the APEX observations. The spectral correlator covers 4 GHz bandwidth in each of the two sidebands separated by 10 GHz. The frequency coverages are 225.76 – 229.73 GHz in the lower sideband and 237.73 – 241.71 GHz in the upper sideband. Each band is divided into 48 chunks. A hybrid resolution mode was set with 512 channels per chunk (16.2 kHz resolution) for the HDO $J_{K_-K_+}$=$3_{1,2}-2_{2,1}$ (s47), and 256 channels per chunk (32.4 kHz) for the HDO $J_{K_-K_+}$=$2_{1,1}-2_{1,2}$ (s46).
The visibility data were calibrated using the MIR software package, which was originally developed for the Owens Valley Radio Observatory. The absolute flux density scale was determined from observations of Neptune for all data. The pair of nearby compact radio sources 1743-038 and 1911-201 was used to calibrate relative amplitude and phase. We used 3C279 to calibrate the bandpass.
The calibrated visibility data were Fourier transformed and CLEANed using the MIRIAD package. The map was made using uniform weighting. The synthesized beam size was 3.″4×2.″5 with a position angle of –64°. The continuum map was obtained by averaging all line-free channels in the two bands except chunks s44-s48 because they have different frequency resolution.

4.3 First results

4.3.1 Single-dish observations

The spectra observed toward G34.26+0.15 are presented in Figure 4.1. All transitions are detected. They all appear in emission, except for the 893 GHz line, which shows a complex profile, dominated by an absorption component. This is because the 893 GHz line is a ground transition and has a high critical density. The line profiles of the three high-excitation transitions (225, 241, and 266 GHz) are close to Gaussian and their linewidths are ∼ 6.3 – 6.7 km/s, obtained from a Gaussian fit. Not only are the profiles of 225 and 241 GHz HDO lines very similar, but their intensities are very close to each other. The

[1] http://www.apex-telescope.org/telescope/efficiency/index.php

linewidth of the 464 GHz HDO line is slightly wider than the high-excitation lines ($\sim$ 7.2 km/s), although this does not appear to be significant, owing to the large error bars, and as shown in Fig. 4.1(f), which displays the superposition of the 464 and 241 GHz line profiles. It is found that the difference between these two spectra is still within the 3σ noise level, and that there is no obvious evidence for the existence of a broad component in the 464 GHz line, as was found in some ground transition H_2O lines (Kristensen et al. 2010b; Chavarría et al. 2010).

Table 4.2 lists the properties of the observed HDO lines. Using the integrated line intensities, we performed a rotation diagram analysis assuming that the lines are optically thin and in local thermodynamic equilibrium (LTE) (Goldsmith & Langer 1999). We considered only the three high-excitation lines, because the two ground-state lines are suggested to be optically thick (see section 4.3). We assumed a $1''$ source size, as suggested from the interferometric observations (Table 4.3). Because this size is smaller than the three observational beams, the derived column density and source size are degenerate, and the temperature does not depend on the size assumption. The resulting rotation diagram is displayed in Figure 4.2. The rotation temperature obtained is $\sim 141^{+489}_{-62}$ K, which is consistent with the estimates of the kinetic temperature (160$\pm$30 K) from the analysis of OCS, CH_3OH, SO, and HC_3N (Mookerjea et al. 2007). The derived total molecular column density of the hot HDO is 4.1×10^{17} cm^{-2} averaged on the assumed $1''$extended source.

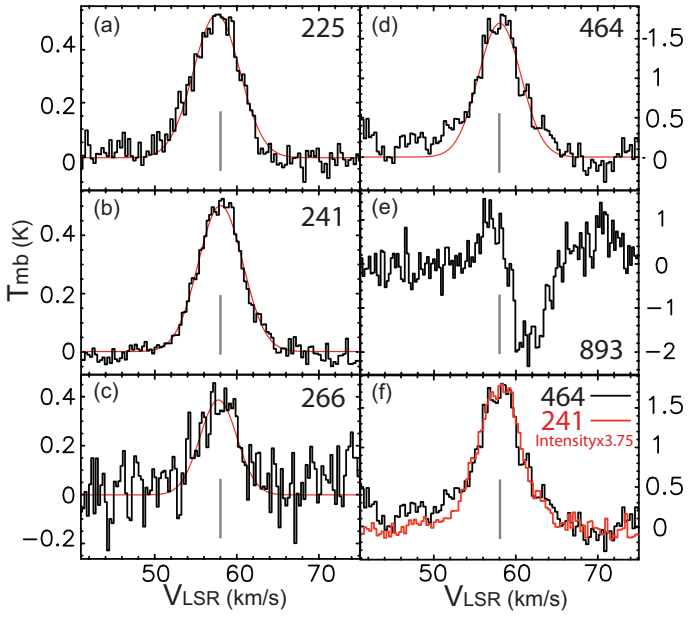

Figure 4.1 (a)–(e) HDO spectra observed with APEX. The red lines indicate the results of the Gaussian fit. (f) Comparison of the HDO 464 and 241 GHz spectra. The numbers in the plots indicate the observed frequencies (in GHz). The gray vertical lines are at $V_{LSR} = 58$ km/s.

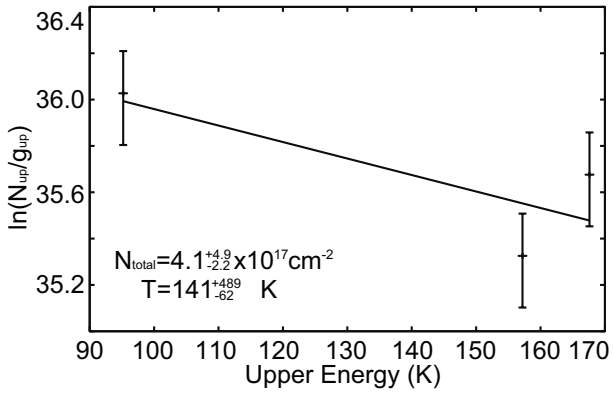

Figure 4.2 HDO rotation diagram. The detected lines are shown as crosses with error bars. The size of the error bars corresponds to 20% of the intensity due to the calibration uncertainty.

Table 4.2. Properties of the HDO lines.

Freq. GHz	rms[bce] K	$T^{c}_{\rm cont}$ K	$T^{ce}_{\rm peak}$ K	$V^{e}_{\rm LSR}$ km/s	Δv[de] km/s	$\int T_{\rm mb}$dv[ef] K km/s
		APEX Observations				
225	0.06	0.85	0.53	57.5±0.1	6.7±0.2	3.8±0.1
241	0.04	0.88	0.52	58.0±0.2	6.3±0.5	3.5±0.2
266	0.12	0.9	0.37	57.9±0.2	6.6±0.6	2.6±0.2
464	0.24	4.0	1.66	57.9±0.2	7.2±0.4	12.6±0.6
893	0.53	13.0	-1.89[a]	61.9±0.1[a]	3.7±0.1[a]	-8.4±0.6[a]
		SMA Observations				
225	4.2	...	0.32	57.9±0.1	7.0±0.2	2.4±0.1
241	17.0	...	0.33	57.9±0.1	6.3±0.2	2.2±0.1

[a] Only the absorption part, between velocity ($V_{\rm LSR}$) 57.6 – 66.2 km/s.

[b] The rms values are measured with the resolutions of the original observation settings (Table 4.1).

[c] $T_{\rm mb}$ scale

[d] FWHM

[e] Value is derived from a Gaussian fit using the software CLASS.

[f] The uncertainties only include the statistical noise and not the calibration uncertainties.

Table 4.3. Results of the SMA observations

	Beam	Freq.	rms	Integrated flux[b]	Peak position[b]		Positional error[c]		Deconvolved size
	″	GHz	Jy/Beam		RA(J2000)	DEC(J2000)	″	″	″
HDO 225	3.″70×2.″54	225.9	0.06	71.3 Jy·km/s	$18^h53^m18^s.61$	$01^o14^m58^s.38$	0.04	0.02	...[ab]
HDO 241	3.″57×2.″44	241.6	0.09	72.8 Jy·km/s	$18^h53^m18^s.61$	$01^o14^m58^s.46$	0.04	0.02	1.″12×0.″67
1.3 mm	3.″44×2.″35	233.6	0.05	8.0 Jy	$18^h53^m18^s.59$	$01^o14^m58^s.22$	0.02	0.02	1.″51×1.″03

[a]Deconvolution appears to produce a point source.

[b]Values are obtained from a Gaussian fit using the task IMFIT of the software MIRIAD.

[c]Values are derived from the theoretical formula $\sigma_{position} = FWHM/[\sqrt{8\ln 2}\cdot(S/N)]$ (Condon 1997).

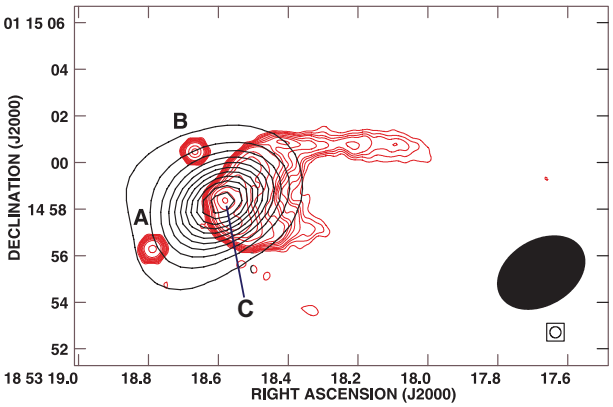

Figure 4.3 Overlay of the 1.3 mm continuum emission observed with the SMA (black contours) with the red contours of the 43.3 GHz free-free continuum emission observed by Avalos et al. (2006). Contour levels are from 3 σ by steps of 6 σ, with 1 σ = 0.1 Jy beam^{-1} for the SMA images and at -4, -3, 3, 4, 5, 6, 8, 10, 12, 15, 20, 40, 60, 100, 200, 400, and 800 times the noise, with 1 σ = 1.04 mJy beam^{-1} for the 43.3 GHz images. The synthesized beams of the SMA (black) and free-free emission (red) images are shown in the lower right of the plot. The synthesized beam of the 2-cm image is 1.″00 × 0.″85 with P.A. = 35°.

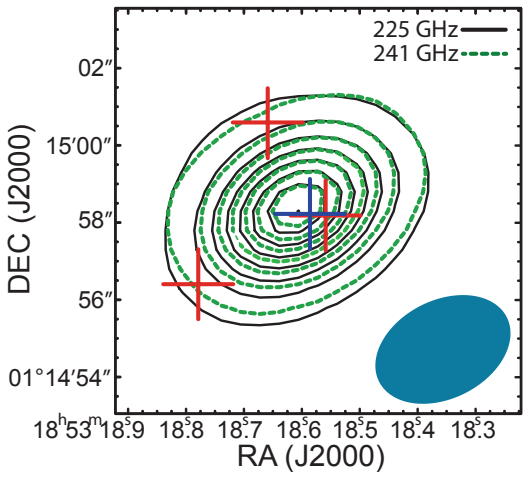

Figure 4.4 HDO 225 GHz (black contours) and HDO 241 GHz (green-dashed contours) integrated map observed with the SMA. The contour levels are from 3 σ by steps of 6 σ, with 1 σ = 1.5 Jy beam^{-1}. The red crosses indicate the peak of the 24 GHz free-free continuum emission (A, B, and C positions from Heaton et al. (1989)) and the peak (maximum pixel) of the 1.3 mm continuum observed with the SMA is shown with the dark blue cross. The blue ellipse indicates the beam size.

4.3.2 Interferometer observations

4.3.2.1 *Continuum at $\lambda = 1.3$ mm*

The total continuum flux retrieved within the SMA primary beam is 8.0 Jy. The continuum emission is found to be slightly resolved (Tab. 4.3). Figure 4.3 shows an overlay of the 1.3 mm continuum image with the free-free continuum emission observed by Avalos et al. (2006). The continuum peak detected at 1.3 mm does not coincide with HII regions A and B, but is roughly consistent with HII region C within the beam size (detail see Fig. 4.4). At 107 GHz, the integrated continuum intensity of 6.7 Jy is suggested to be dominated by free-free emission and only $\sim$10% can be contributed from dust (Mookerjea et al. 2007). To date, neither the turnover point of free-free emission nor the spectral index are clear. Thus, if the free-free emission is already optically thin at a wavelength longer than 3 mm, the free-free emission will contribute $\sim$6 Jy to the emission at 1.3 mm. In other words, the detected continuum flux with the SMA is the combination of free-free and dust emission. Figure 4.4 also supports this argument, because the peak of the 1.3 mm continuum is located between the peak of the free-free emission (from which it is offset by $\sim 0.3''$) and the HDO peak. This point will be important when modeling the emission with RATRAN (which models only the dust continuum).

4.3.2.2 *Spectral lines*

The observational results for the two HDO lines are listed in Table 4.3. The integrated intensity maps of the two HDO lines (Figure 4.4) show that their emission distributions are similar, suggesting that the emission comes from the same gas. In addition, the emission is not coincident with the A and B compact HII regions. The peak of the HDO emission is offset from the 1.3 mm dust continuum peak by

approximately 0.3–0.4″(Table 4.3), under the theoretically positional error of approximately 0.04″with a signal-to-noise ratio (S/N) of 43. We believe that this offset is significant, because the continuum and the lines were observed simultaneously. This offset seems to be much smaller than the offset (2″) observed for CH_3CN by Watt & Mundy (1999), and on the lower end of the different offsets observed for different molecules (CH_3OH, SO, and OCS) by Mookerjea et al. (2007). Those molecules have lower critical densities[2] compared to the two HDO lines, so excitation effects might partly explain the discrepancy between the distribution of the molecules.

Comparing the results observed with APEX, we find that the missing flux of the HDO 225 GHz and 241 GHz line emission are $\sim$37.1% and $\sim$36.4%, suggesting that most HDO emission is coming from the center of the molecular cloud core, which is consistent with the fact that the line shapes are very similar. Here, the SMA map was convolved with the beam size of APEX. The calibration uncertainties of APEX and SMA are usually considered to be $\sim$20% and 5–15%. It is difficult to believe that the apparent missing flux is real, because that would require that these high-excitation HDO lines show some extended emission, which is very unlikely in view of their critical density and energy. Indeed, the differences in fluxes between the SMA and APEX spectra can be also caused by the side lobes in the SMA images. Because the declination (δ_{2000}) of our source is around 1 degree, the side lobes are quite strong and cannot be easily removed thoroughly. The negative side lobes will lower the obtained integrated flux (SMA) in this case. We therefore assume that the flux discrepancy is only originating in the uncertainty of the calibration and imaging of the data.

We resolved the CN 2–1 hyperfine structure of J=3/2-1/2 and J=5/2-3/2. All CN absorption lines show redshifted absorption; we discuss in more detail in section 5.2.2.

4.4 Modeling

4.4.1 Physical profiles of the source

To analyze the HDO data, we used the 1 D Monte Carlo code RATRAN, developed by Hogerheijde & van der Tak (2000). The radiative transfer model takes as input the physical (n, T) profiles of the source. The heating source of the hot core and its density structure are not clearly understood toward G34.26+0.15, because there is no high angular resolution study ($\leq 1''$) in the submillimeter band. It has been argued that the hot core could be externally heated by this HII region (Mookerjea et al. 2007), because the hot core lies off the cometary-shaped HII region (Watt & Mundy 1999). This cometary-shape may be caused by the bow shock produced by the wind from a young star that moves at supersonic speed through an ambient molecular cloud (Wood & Churchwell 1989; van Buren et al. 1990; Watt & Mundy 1999) or by the champagne outflow (Andersson & Garay 1986; Fey et al. 1992; Carral & Welch 1992; Gaume et al. 1994). The separations between the HII region and the emission peaks of most N- and O-bearing molecules are $\leq$1″ (Mookerjea et al. 2007, see figure 3). However, recent studies with HCN, HCO^+, CO, and their isotopes observed with APEX show no evidence for this scenario and, moreover, the results show self-absorption and strong red asymmetries, which suggest an in-falling source with internal heating

[2]At 100 K, their critical densities are 1.1×10^5, 3.8×10^6, 6.6×10^4, and 5.3×10^3 cm^{-3}, calculated using the values of the Einstein coefficient and the collision rates tabulated (Green 1986; Pottage et al. 2004; Kristensen et al. 2010a; Green 1994; Green & Chapman 1978; Schöier et al. 2005) in the LAMDA database.

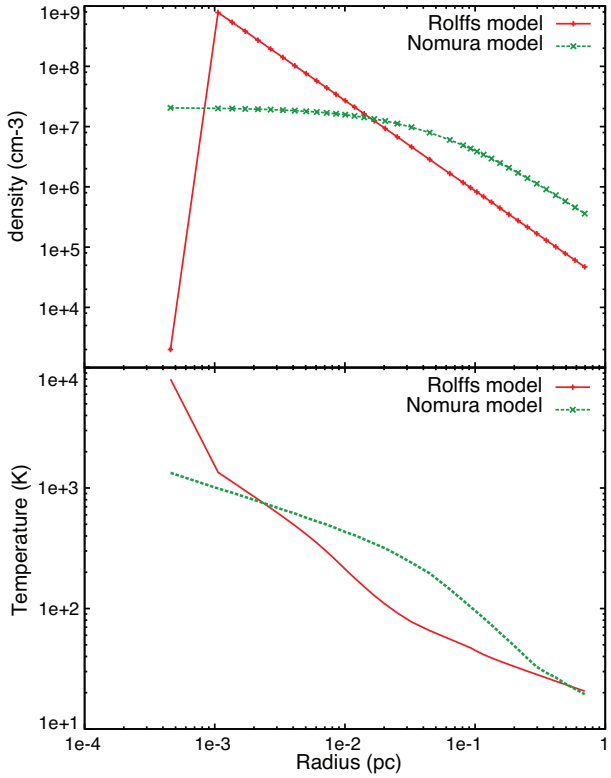

Figure 4.5 Comparison of the physical profiles of the two different models toward G34.26+0.15 (Nomura & Millar 2004; Rolffs et al. 2011).

Table 4.4. Fitting parameters and their results

Physical profiles	Turbulent linewidth[a] km/s	Radius at 100 K pc	Best fit HDO abundances inner region	Best fit HDO abundances outer region	$\chi^2_{\rm red}$	HDO abundances confidence interval (3σ) inner region	HDO abundances confidence interval (3σ) outer region
Rolffs model[b]	3.0	0.02	6.0×10^{-08}	5.0×10^{-12}	6.0	$(5.0 - 7.0) \times 10^{-08}$	$(0.3 - 2.0) \times 10^{-11}$
Nomura model[c]	3.0	0.09	4.0×10^{-10}	1.0×10^{-14}	19.6	$(2.0 - 5.0) \times 10^{-10}$	$\leq 1 \times 10^{-13}$

[a] Fixed parameter

[b] Rolffs et al. (2011)

[c] Nomura & Millar (2004)

(Rolffs et al. 2011). In addition, the studies of the NH_3 (3_2-2_2) line observed with SOFIA also present a clear in-fall absorption in the spectra which are well reproduced also with Rolffs' model (Wyrowski et al. 2012). This may be because they probe larger scales and the structures of the heating area are too small to be resolved in their observations (Rolffs et al. 2011). Therefore, the external heating structures could be internal in the model. Neither our APEX nor our SMA data have a sufficiently high resolution to probe the scale of the heating region; therefore, the two models we adopted here have the temperature structures derived by the inner heating source.

We use in the following the physical profiles of two different models (Nomura & Millar 2004; Rolffs et al. 2011, Figure 4.5). Nomura's model is constrained by the observed spectral energy distribution (SED) data at wavelengths from far-infrared to millimeter. Most data are from Chini et al. (1987) and were observed with the ESO 1 m telescope, except for an additional point at around 3 mm (Nomura & Millar 2004, see figure 1c). The 3-mm data point is taken from Watt & Mundy (1999) and were observed with BIMA (Nomura, private communication). As in Nomura's study, the model with the column density of $N = 10^{25}$ cm^{-2} is used here. The density and temperature profiles of the Rolffs model aim to reproduce the radial intensity profile from LABOCA data (345 GHz continuum). We adopted the opacity and velocity field setting of the Rolffs model for both models (opacity: ice mantle coagulation at a density of 10^5 cm^{-3} (Ossenkopf & Henning 1994); velocity field: $V = -0.2(\frac{2GM_{in}}{r})^{1/2}$ (Rolffs et al. 2011)). The turbulent linewidth, db, is set to be 3.0 km/s. The adopted distance is 3.7 kpc (Kuchar & Bania 1994). The HDO collisional rates used in this study are computed by Faure et al. (2012) for para-H_2 and ortho-H_2 separately. In the modeling, we assumed that the ortho-to-para ratio of H_2 is in LTE in each cell of the core.

4.4.2 Modeling procedure

The HDO emission was modeled with a jump model, where the fractional abundances of deuterated water, relative to H_2, in the inner part of the source ($T > 100$ K, assumed evaporation temperature) and in the outer part ($T \leq 100$ K) are two free parameters, $X_{\rm in}^{\rm HDO}$ and $X_{\rm out}^{\rm HDO}$. We made two sets of comparisons, one with the APEX data and the other with the SMA data. For comparison with the APEX data, the modeled maps were convolved with the APEX beam. For comparison with the SMA data, we used MIRIAD to create mock observations based on the modeled data. We first inserted the values of the observed parameters (epoch, rest frequency, and the coordinate of the observed reference position) into the blank header of the modeled data. Then, we multiplied the modeled image by the SMA primary beam. Afterward, we applied the (u,v) sampling retrieved from the SMA data to the modeled image and inverted the resulting (u,v) data to obtained the simulated maps/spectra. We then performed χ^2 analyses for $X_{\rm in}^{\rm HDO}$ ranging from 1×10^{-9} to 4×10^{-7} and for $X_{\rm out}^{\rm HDO}$ ranging from 1×10^{-15} to 2×10^{-11} for the Rolffs model and for $X_{\rm in}^{\rm HDO}$ ranging from 1×10^{-12} to 5×10^{-9} and for $X_{\rm out}^{\rm HDO}$ ranging from 1×10^{-17} to 5×10^{-10} for the Nomura model. We intend to also model the line velocity profiles and all spectra, including the spectra from the SMA data. Here the definition of χ^2 is $\Sigma\frac{(\rm T_{mb,ob}-T_{mb,mod})^2}{\sigma^2}$, where the sum is over each channel in each spectrum. The σ within this χ^2 analysis includes the statistical errors and uncertainties in flux calibration ($\sim$10% for 225 and 241 GHz observed with SMA, $\sim$30% for 893 GHz and $\sim$20% for other lines observed with APEX), but does not include any uncertainty in the adopted collisional rate coefficients used in the excitation calculation (Faure et al. 2012).

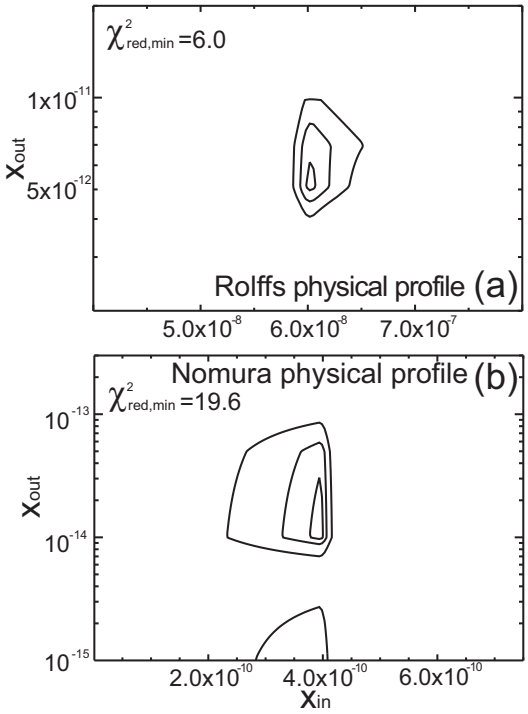

Figure 4.6 X_{in}^{HDO} and X_{out}^{HDO} contours (1, 2 and 3σ) for the χ^2_{red} for the different models. Fig (a) and (b) show the χ^2 contours calculated over all spectra with the Rolffs and Nomura physical profiles.

4.4.3 Results

The black solid lines in Fig. 4.6 present the contours delimitating the 1σ (68.3%), 2σ (95.4%) and 3σ (99.7%) confidence intervals. These contours are derived with the method described in Lampton et al. (1976), who showed that the $\Delta S = \chi^2 - \chi^2_{\rm min}$ random variable follows a χ^2 distribution with p variables, p being the number of parameters. Here p=2 (X_{in} and X_{out}), so that these contours correspond to $\chi^2 = \chi^2_{\rm min}$+2.3, $\chi^2_{\rm min}$+6.17 and $\chi^2_{\rm min}$+11.8. Here we used 1σ, 2σ, and 3σ in analogy with Gaussian-distributed random variables.

The fitting parameters and obtained results are listed in Table 4.4. The observed spectra are overlaid with the modeling results of the best fit in Figure 4.7. Here the system velocity of 58 km/s is assumed ($V_{\rm LSR}$). The minimum $\chi^2_{\rm red}$ are not close to 1, which indicates that the spectra are not well reproduced by the two different physical models. This is also obvious in Figure 4.7. When the Rolffs model is adopted (red lines in Figure 4.7), the emission at 225, 241, and 266 GHz is not high enough at the large scale to fit the observed data (APEX data), but the most compact emission in the 225 and 241 GHz lines is well reproduced (SMA data). At the same time, the simulated spectra at 464 and 893 GHz are optically thick ($\tau = 2.1$ and $\tau = 24.1$ at lines and source center) and the line profile in 893 GHz spectrum does not fit the observed spectrum either. In Figure 4.7, the blue and green lines indicate the results of the best-fit model using the Nomura physical profile, the green line was obtained excluding the spectrum at 893 GHz from the χ^2 analysis. In this case, the fractional abundances are 2×10^{-9} and 5×10^{-12} for the inner

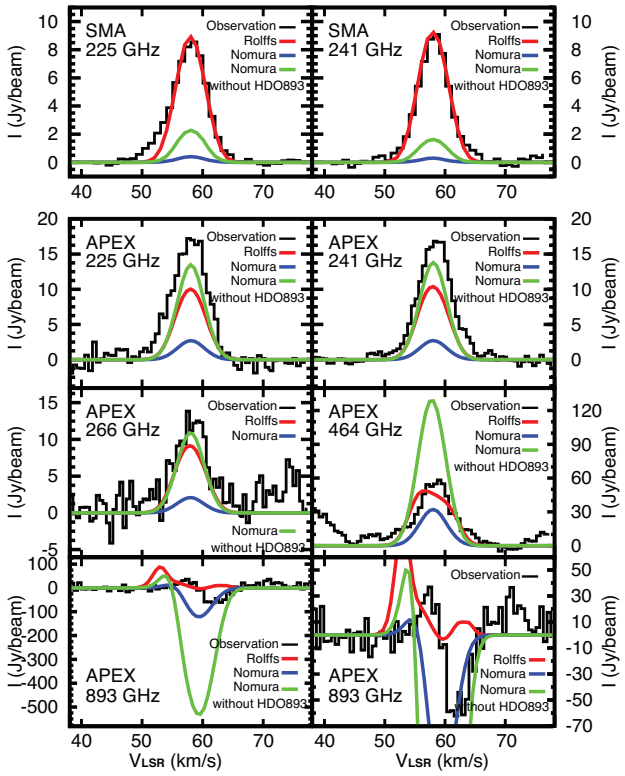

Figure 4.7 Comparison of the observed spectra with the results of our best-fit models for the two different physical profiles. The observed line emission is shown as black histograms in each spectrum. The red, green, and blue lines show the best-fit results of the Rolffs model, the Nomura model with all spectra, and the Nomura model excluding the HDO spectrum at 893 GHz ($X_{\rm in}^{\rm HDO} = 2 \times 10^{-9}$; $X_{\rm out}^{\rm HDO} = 5 \times 10^{-12}$).

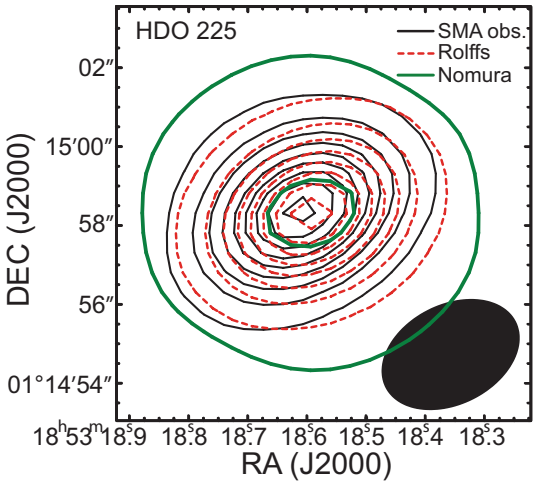

Figure 4.8 Overlay of the HDO 225 GHz integrated map observed with the SMA (black contours) with the simulated ones of the best-fit results of the Rolffs model and of the Nomura model excluding the HDO spectrum at 893 GHz. The red and green contours show the integrated HDO 225 GHz map of the best-fit results of the Rolffs model and of the Nomura model excluding the HDO spectrum at 893 GHz. These two integrated maps are simulated to be observed with the uv-coverage of the SMA observations. All contour levels are from 3 σ by steps of 5 σ, with 1 σ = 1.5 Jy beam^{-1}. The black ellipse indicates the beam size.

and outer region. This model fails to reproduce the central emission observed with the SMA.

Comparing the results reproduced by the two models (red and blue), we find that the best fit based on the Rolffs model is closer to the observed data ($\chi^2_{\rm red} = 6.0$). The fitting problems in the ground transitions (464 and 893 GHz) are slightly less severe than for the Nomura model (see Fig.4.7). Moreover, from the comparison of the two fitting results of the Nomura model (blue and green), we find that the absorption in the 893 GHz spectra and emission in 464 GHz are too strong if we try to increase the emission in the high-excitation lines to fit the spectra (225, 241, 266 GHz). Indeed, the continuum flux reproduced with the Nomura model ($\sim$ 49 K) is much higher than the real flux ($\sim$ 13.0 K). This is also found in Appendix A.2. and A.3. Figure 4.8 shows the angular distribution of the 225 GHz line from the SMA observation and the two models. Here again the model based on the Rolffs profiles fits the data much better. This is similar for the 241 GHz line and is therefore not shown.

The model based on the Rolffs centrally heated core reproduces the SMA observed line distribution well. This does not exclude the possibility that the heating of the very central dust core is external, but it shows that even at the resolution of our SMA data, we do not see clear evidence of a non-spherically symmetric heating of the envelope, and that the large-scale properties of the envelope can therefore be derived using such a model. Distinguishing between internal and external heating at small scales would require observations with much higher angular resolution.

Based on the superior results obtained with the Rolffs profiles, we focus on the Rolffs model below and try to reproduce the lines with a two-jump model of the HDO abundance distribution. Finally, we modify Rolffs physical structure to try to fit the observed data. The results of the two-jump model and modified models are discussed in Sections 5.1 and 5.2 and in Appendices A.2. and A.3.

Table 4.5. Parameters of the models

Model	X_{in1}^{HDO}	X_{in2}^{HDO}	X_{out}^{HDO}
One Jump[a]	6×10^{-8}	6×10^{-8}	5×10^{-12}
Two Jump 1 (2J1)	3×10^{-7}	6×10^{-8}	5×10^{-12}
Two Jump 2 (2J2)	3×10^{-7}	3×10^{-8}	5×10^{-12}
Two Jump 3 (2J3)	2×10^{-7}	6×10^{-8}	5×10^{-12}
Two Jump 4 (2J4)	2×10^{-7}	3×10^{-8}	5×10^{-12}
Two Jump 5 (2J5)	2×10^{-7}	3×10^{-8}	1×10^{-14}

[a] The results of the one-jump best-fit model.

4.5 Discussion

4.5.1 Two-jump model

To reproduce more emission in the high-excitation lines and decrease the emission in the 893 GHz line, we modeled the spectra with a two-jump model instead of a one-jump model. The additional jump was arbitrarily set to be located at T = 200 K. Figure 4.9 show the results of four testing models. The adopted HDO fractional abundances of the models are listed in Table 4.5. The red lines indicate the results of the original best-fit one-jump model, which underestimates the high-excitation lines. The two-jump models (2J-1 and 2J-3) are found to be somewhat better for these transitions (Fig. 4.9). This suggests that the two-jump model can produce higher emission in the high-excitation lines. This property has already been found for Sgr B2 (M) (Comito et al. 2010) and this is due to the very high critical density of these lines (see Table 1). Moreover, although we decreased the HDO fractional abundance in the second inner region of the core in model 2J-2 and 2J-4 by a factor of 2, the emission in the 893 GHz line is little affected ($< 1\sigma$). In addition, the line shapes of different lines do not change from model to model. Therefore, the results suggest that adopting a two-jump model can help in increasing the emission in the high-excitation lines, but cannot improve the 893 and 464 GHz line shapes. We note, however, that because the inner part is very compact, the enhancement of the high-excitation lines in the APEX beam when increasing the HDO abundance in this inner part is linked to an even faster relative enhancement of the flux in the SMA beam. As a consequence, one cannot increase the inner HDO abundance too much, even if the effect on the APEX lines is almost unnoticeable.

4.5.2 Modified physical profiles

In the previous sections, we have seen that the observed spectra are not perfectly reproduced using the Rolffs physical profile, even with a two-jump model. This is also the case for some HCN lines (see Fig. 5 in Rolffs et al. 2011). We now investigate how the model can be improved by modifying the physical profiles from the Rolffs model. We first investigate where the HDO emission and absorption take place by means of a shell analysis and then test the effect of modfying the physical profiles of the Rolffs model.

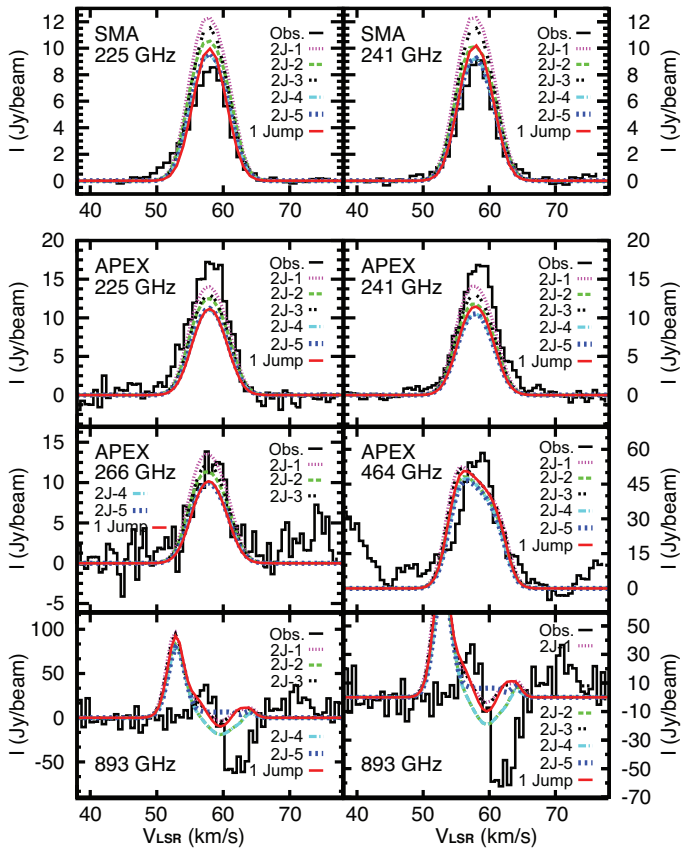

Figure 4.9 Comparison of the observed spectra and those simulated with different models. The red lines are the spectra of the original one-jump model.

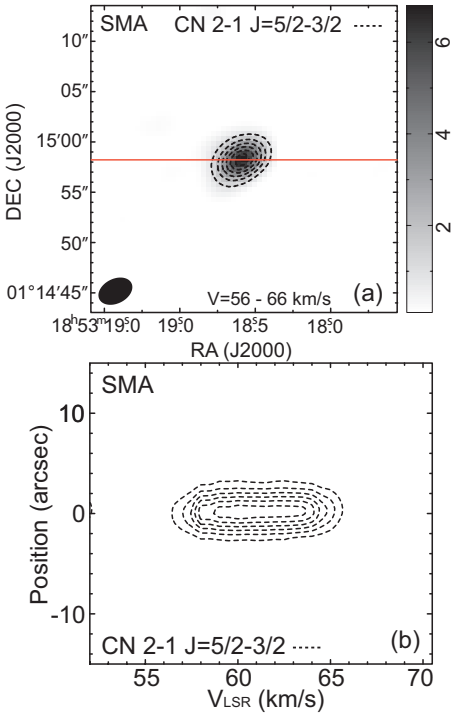

Figure 4.10 Integrated moment-0 map of CN 2-1 J=5/2–3/2 F=7/2-5/2 line (blended with the F=5/2-3/2 and F=3/2-1/2 lines) overlaid with the dust continuum map (a). The red line indicates the cut for the position-velocity (P-V) diagram. The P-V diagram of the CN line (b). Both are observed with SMA. The contours in fig. (a) are -0.67, -1.34, -2.01, -2.68, -3.35, and -4.02 and in fig. (b) they are -0.97, -1.94, -2.91, -3.88, -4.86, and -5.83. The P-V diagram is cut at the position of the observed center and position angle of 0.

4.5.2.1 Shell analysis and modified density/temperature profiles

To analyze the discrepancy between the best-fit model and the observed data, we performed a shell analysis by sequentially turning the abundance of HDO in the innermost shells to 0 and then simulating new spectra (Figure A1). The results of this study are shown in Appendix A.1. We find that the emission of all transitions (even the 893 GHz line) originates in the inner region, whereas the absorption originates in the outer region. This explains why it is impossible to improve the line profile of the 893 GHz within the frame of a jump model. Improvement can therefore only be achieved by modifying the physical profiles (density, temperature, velocity) of the source. In Appendices A.2 and A.3, we show that modifications of the density and temperature profiles are unable to improve the quality of the fit. In the next section, we investigate the effect of modifying the velocity field.

4.5.2.2 Modified velocity profile

– Modified infall velocity field

So far, we used the velocity profile provided by Rolffs et al. (2011) for all modeling. This is a modified free-fall velocity field. However, the line shape in the 893 GHz spectra cannot be simply reproduced by

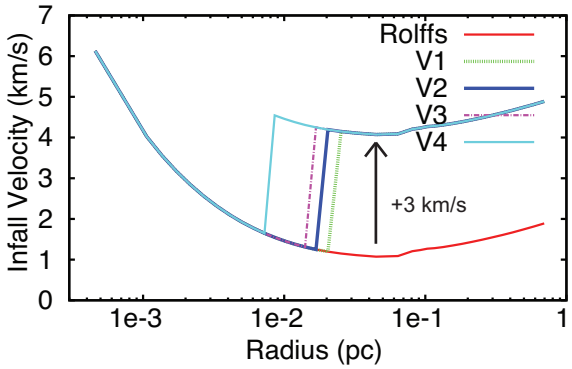

Figure 4.11 Comparison of the velocity profiles of the four different modified models (green, blue, purple, and light-blue) and the one of the Rolffs original model (red).

our present model, which might imply that there is an additional velocity field in the core.
Figure 4.10 shows the moment-0 map overlaid with the dust continuum map (a) and the position-velocity diagram (b) of the CN 2–1 absorption line observed with the SMA simultaneously to the HDO lines. Clearly, the distribution of the CN absorption is consistent with that of the dust continuum, as in the case of HDO. Moreover, the central velocity of the position-velocity diagram of the CN absorption is about 61 km/s, not 58 km/s. This redshifted absorption has already been found for many molecules, for instance NH_3, CO, ^{13}CO, and HCO^+(Heaton et al. 1989; Gómez et al. 2000; Wyrowski et al. 2012). Thus, it is possible that the gas that produces the absorption feature in the HDO 893 GHz spectra has a similar velocity distribution. Therefore we tried to modify the velocity field by adding a 3 km/s difference from the outer region to the inner region of the core (Figure 4.11). The results are shown in Figure 4.12. The spectra are simulated with the fixed fractional abundances 6×10^{-8} ($X_{\rm in}^{\rm HDO}$) and 5×10^{-12} ($X_{\rm out}^{\rm HDO}$) (best-fit model). The additional velocity (3 km/s) widens the emission of the optically thin lines (225, 241, and 266 GHz) somewhat, which enables a better fit of the line-width of the SMA lines. The opacities of the HDO 464 and 893 GHz lines are reduced and the 464 GHz line becomes optically thinner in models V3 and V4 ($\tau = 1.3$ and 0.8). Moreover, the peak positions of the absorption in the simulated 893 GHz spectra gradually approach those of the observed 893 GHz spectra. Therefore, carefully modifying the velocity field might be a good way to improve the fits. However, the detailed velocity profile around the boundary region of the core cannot be constrained from our data now. To obtain better modeling results, it is necessary to observing the HDO line map at 893 GHz with high angular resolution. In addition, this result also suggests that studying the HDO spectrum at 893 GHz can help us to understand the velocity field of the core.

– Modified turbulence velocity width

Because the line profiles are also affected by gas motions, the turbulence is also responsible for the line emission/absorption widths. The assumption that turbulence varies over the core has already been used for analyzing the spectra lines toward several massive sources and brought nicely fitting results (Herpin et al. 2009). Our previous study shows that the width of all simulated 893 spectra is obviously much wider than that of the observed spectrum, while the widths of the high-excitation lines are well fitted. Thus, we modified the turbulent velocity field by changing the parameter db in the model. In the Figure

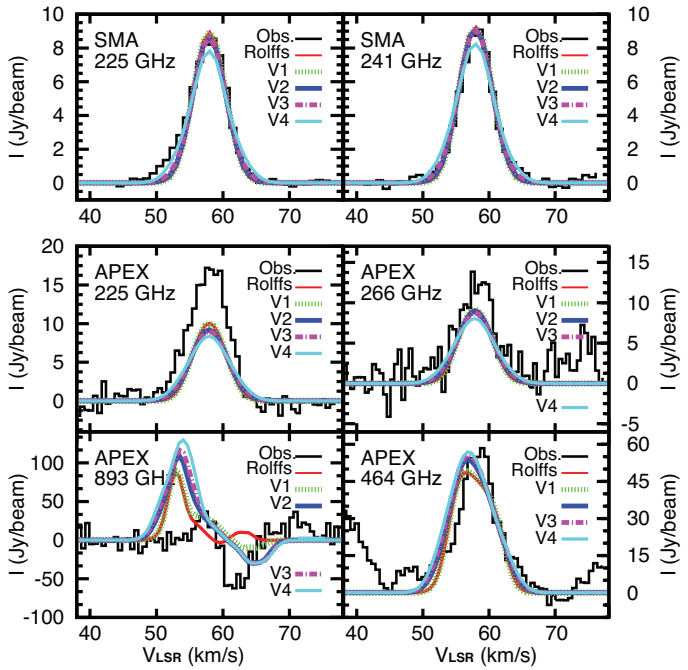

Figure 4.12 Comparison of the observed and modeled spectra using the velocity profiles V1-V4 (Fig. 4.11) and the same HDO fractional abundance as in the best fit. The red lines are the spectra modeled with the best-fit model using the original Rolffs physical profile. The observed and fitting spectra at 241 GHz are very similar to the those at 225 GHz; therefore, only the spectra at 225 GHz are plotted here.

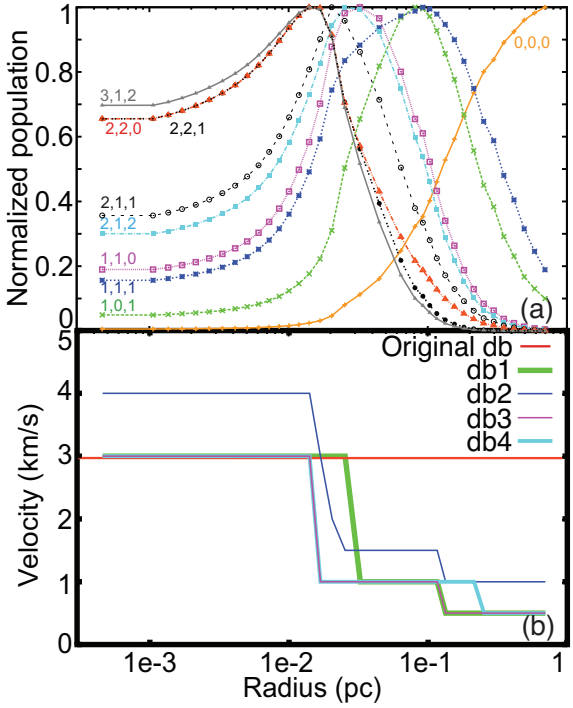

Figure 4.13 HDO normalized population of the selected levels of the Rolffs original model (a) and comparison of the turbulent velocity fields of the four models (db1 – db4) and the turbulent velocity fields of the original model (red) (b).

4.13a, the distribution of the populations of the upper level of high-excitation lines ($3_{1,2}$, $2_{2,0}$, and $2_{2,1}$) is different from those of the ground-transition lines ($1_{1,1}$ and $1_{0,1}$). The peaks of the high-excitation line populations are mainly located in the layer 15 – 16 ($1.4\times10^{-2}-1.7\times10^{-2}$ pc) and those of the ground-transition lines are placed in the layer 21 – 24 ($6.4\times10^{-2}-1.0\times10^{-1}$ pc). We used these considerations for elaborating our new db settings with the aim to narrow down the width of the simulated 893 spectra without significantly affecting the width of the high-excitation lines. Figure 4.13b illustrates our different db settings. The HDO fractional abundances in the model db1 – db4 are fixed with the values of the best-fit model: $X_{\rm in}^{\rm HDO} = 6\times10^{-8}$ and $X_{\rm out}^{\rm HDO} = 5\times10^{-12}$.
Comparing the spectra at 893 GHz with those of the previous best-fit model (Fig. 4.14), we find that the line profile has significantly improved much in db2 – db4. The width of the absorption part is narrower than before and more similar to the observed one. Moreover, we have better fits compared to previous spectra at 266 GHz and the opacity is reduced in the 464 GHz spectra. In addition, the $\chi^2_{\rm red}$ model db2 is 5.5, which is better than that of the Rolffs original model (6.0), showing that the fits can be improved by modifying the turbulent velocity field. We also performed χ^2 analyses for the same range of $X_{\rm in}^{\rm HDO}$ and $X_{\rm out}^{\rm HDO}$ in the section 4.2 based on model db2. The fractional abundances of the new best-fit in this test are still the same as in our previous results ($X_{\rm in}^{\rm HDO} = 6\times10^{-8}$ and $X_{\rm out}^{\rm HDO} = 5\times10^{-12}$). This implies that the turbulence velocity is not constant throughout the envelope of G34.26+0.15. However, the widths at 225 and 241 GHz are narrower than the previous and observed ones, suggesting that the db in the inner region of the core is not wide enough in the models. Here again, high angular resolution data at 893 GHz would be very helpful.

– Composition of the turbulent and infall velocity field effects
Because modifying the infall velocity field can help to move the peak of the absorption at 893 GHz (model V1), and modifying the turbulence velocity field can narrow this absorption, we ran models with modified velocity (V1 and db2). The result is shown in figure 4.15. Obviously, we can now reproduce part of the emission and all the absorption with better width and proper position, which allows us to study the fractional abundance in the outer region of the core. On the other hand, as expected, the emission at 893 GHz is not reproduced properly, because it originates from the inner region of the core (T>100 K) and the model V1 only changes the velocity field in the outer region of the core (T<100 K). Additional constraints in this direction will hopefully come from interferometeric data.
In conclusion, we have shown that it is possible to improve the original best-fit model by modifying the velocity field of the source. This improvement is obtained while keeping the fractional abundance of HDO to the value we derived with the original velocity setup of Rolffs et al. (2011). This study confirms the validity of the fractional abundance of HDO derived from the best-fit model in Sect. 4.4.3. Further steps toward constraining the velocity field and therefore a better HDO model will need high angular resolution observations of, e.g., the HDO 893GHz line.

4.5.3 HDO/H_2O ratio

$H_2^{18}O$ is always used to trace H_2O, because H_2O is easily optically thick. Here we compare the emission and absorption of the two para-$H_2^{18}O$ lines $3_{13}-2_{20}$ and $1_{11}-0_{00}$ (Gensheimer et al. 1996; Wyrowski et al. 2010) with our HDO results. Because the analysis of the HDO lines suggests that high-excitation lines can trace and constrain the inner fractional abundance quite well (Parise et al. 2005b; Liu et al.

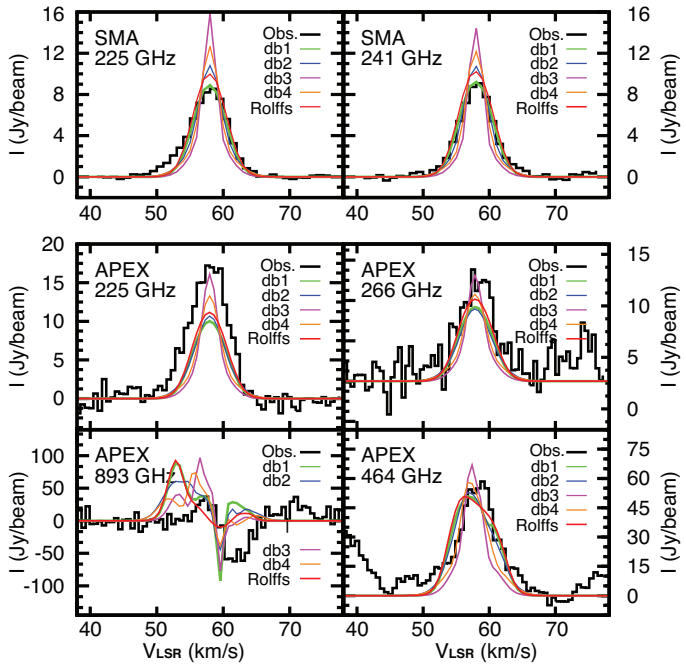

Figure 4.14 Same as Fig. 4.12, but for the models with different settings of the turbulent velocity field (db1 – db4).

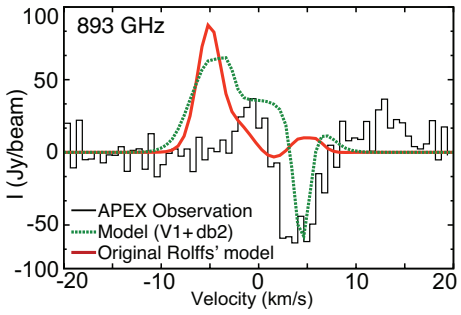

Figure 4.15 Comparison of the observed spectrum, the one of the best-fit model simulated with Rolffs' original physical profile, and the one reproduced with the modified turbulent and infall velocity fields (V1 and db2). The fractional abundance adopted here is the one of the best-fit model.

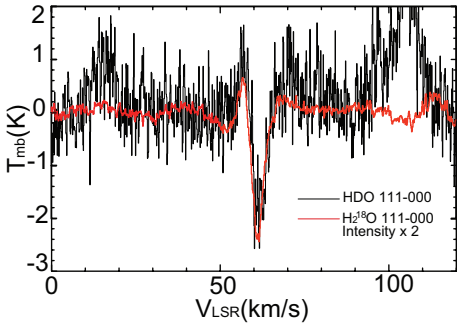

Figure 4.16 Comparison of the HDO at 893 GHz (black) with $H_2^{18}O$ $1_{11} - 0_{00}$ (red) spectra. The $H_2^{18}O$ data are taken from Wyrowski et al. (2010).

Table 4.6. Line parameters and continuum temperature corresponding to the frequency of each line. The parameters errors are obtained from the Gaussian fit.

	Freq. GHz	$T_{\rm peak}^{c}$ K	$T_{\rm cont}^{cd}$ K	Δv km/s	τ	$V_{\rm LSR}$ km/s
HDO	893.639	-1.89 ± 0.37	13.0	3.65 ± 0.24	0.17	61.9 ± 0.13
$H_2^{18}O$	1101.698	-1.20 ± 0.07	6.1	3.51 ± 0.06	0.22	61.3 ± 0.03

[c] $T_{\rm mb}$ scale
[d] continuum temperature

Table 4.7. Comparison of HDO fractional abundance between different sources.

Source	$X^{\rm HDO}$(best fit) Inner	outer	$\frac{\rm HDO}{\rm H_2O}$ Inner	outer	$\frac{\rm HDCO}{\rm H_2CO}$	$\frac{\rm DCN}{\rm HCN}$
	High-mass hot cores					
G34.26+0.15	6×10^{-8}[a]	5×10^{-12}[a]	3×10^{-4}[a]	1.9×10^{-4}[a] $-$ 4.9×10^{-4}[a]	0.01[h]	0.001[h]
AFGL 2591	1×10^{-7}[b]	4×10^{-9}[b]	5×10^{-4}[b]	$0.4-4\times10^{-3}$[b]	...	...
W33A	2×10^{-7}[b]	1×10^{-8}[b]		7×10^{-3}[b]	...	...
Orion KL	...	...		2×10^{-2}[c]	0.14[d]	0.005–0.02[k]
	Low-mass protostars					
NGC1333 IRAS2A	8×10^{-8}[e]	7×10^{-10}[e]	$\geq1\times10^{-2}$[e]	$7^{+11}_{-6}\times10^{-2}$[e]	$0.17^{+0.12}_{-0.08}$[f]	
IRAS 16293-2422	1×10^{-7}[g]	1.5×10^{-10}[g]	3×10^{-2}[g]	$\leq2\times10^{-3}(3\sigma)$[g]	0.15 ± 0.07[f]	0.013[m]
	1.7×10^{-7}[i]	8×10^{-11}[i]	3.4×10^{-2}[i]	5×10^{-3}[i]		

[a]This work. [b]van der Tak et al. (2006);[c]Bergin et al. (2010);[d]Turner (1990);[e]Liu et al. (2011); [f]Parise et al. (2006); [g]Parise et al. (2005a); [h]Roberts & Millar (2007); [i]Coutens et al. (2012); [k]Mangum et al. (1991); [m]van Dishoeck et al. (1995)

2011), we can also analyze the high-excitation $H_2^{18}O$ $3_{13} - 2_{20}$ line ($E_u = 204.7$ K) (Gensheimer et al. 1996) to study the $H_2^{18}O$ fractional abundance in the inner region of the core. We reproduced the reported integrated flux and line width (20.5 K and 8.4 km/s listed in Table 2 in Gensheimer et al. 1996) of this $H_2^{18}O$ line with RATRAN using a one-jump model based on the Rolffs original profiles. The resulting fractional abundance of the para-$H_2^{18}O$ in the inner region of the core is $(1.0 \pm 0.7) \times 10^{-7}$ (3σ). Thus, the HDO/H_2O is 3.0×10^{-4} with the assumption that the standard ortho/para ratio is 3 and the $^{18}O/^{16}O$ ratio is 500. This ratio is consistent with the estimate of 1.1×10^{-4} with an uncertainty of a factor of 4 (Gensheimer et al. 1996). Here, the adopted db for this high-excitation $H_2^{18}O$ line is 4.5 km/s instead of 3 km/s, because the width of this $H_2^{18}O$ line is wider than that of the high-excitation HDO lines (8.4 km/s for the $H_2^{18}O$ line compared to $\sim$6 – 7 km/s for the HDO lines). The different properties of the velocity field of the high-excitation $H_2^{18}O$ line may indicate that some part of the emission does not come from the quiescent envelope and the high-excitation HDO lines may not probe exactly the same gas. Therefore, the derived D/H ratio of water in the inner region here should be a lower limit.

Figure 4.16 displays the two spectra of the ground-state $1_{1,1} - 0_{0,0}$ transition of HDO and $H_2^{18}O$. The line shapes are very similar, suggesting they may originate from the same gas. Under the two assumptions that the excitation temperature of the line is negligible with respect to the temperature of the background continuum source and that only the ground state of the molecule is populated, the total column density of the absorbing HDO/$H_2^{18}O$ can then be computed from (Comito et al. 2003; Tarchi et al. 2004)

$$N_{tot} = \frac{8\pi\nu^3}{A_{ul}c^3}\frac{g_l}{g_u}\tau\Delta v,$$

where Δv is the line width and g_l and g_u are the statistical weights of the lower and upper level. The optical depth of the absorbed line can be determined by

$$\tau = -ln(1 - \frac{T_L}{T_C}),$$

where T_L is the brightness temperature of the line and T_C is the brightness temperature of the continuum. The line parameters from the Gaussian fit and the estimated values are listed in Table 4.6. The estimated total column densities are 1.8×10^{12} cm^{-2} for HDO and 1.8×10^{12} cm^{-2} for para-$H_2^{18}O$. Because the profiles of these two lines are very similar to each other, we assumed that both of them are originating from the same gas. Therefore, the [HDO]/[H_2O] ratio is $\sim 4.9 \times 10^{-4}$, assuming that the standard ortho/para ratio is 3 and the $^{18}O/^{16}O$ ratio is 500. However, the abundance of para-$H_2^{18}O$ might be underestimated here, because the emitted area of the continuum at 1101 GHz might be larger than that of the $H_2^{18}O$ due to the large Herschel beam. Assuming that the dust emissivity spectral index β is 2 as for the interstellar medium (Draine & Lee 1984; Schnee et al. 2010), the derived continuum flux at 1101 GHz of the core seen with APEX will be 2.8 K in the Herschel beam and the estimated total column $H_2^{18}O$ density becomes 4.7×10^{12} cm^{-2}. Then the obtained D/H ratio of water is $\sim 1.9 \times 10^{-4}$, which is close to what we obtained for the inner region of the core. We note that this value is uncertain, as the absorption takes place on top of emission in both cases, which we have ignored here.

The comparison of the HDO fractional abundances between different sources is shown in table 6.1. The water deuterium fractionation toward the two low-mass protostars, NGC1333 IRAS 2A and IRAS 16293-2422, have been studied with several HDO transitions (Liu et al. 2011; Parise et al. 2005a; Coutens et al. 2012). Most transitions were also used in this work.

The abundance of HDO jumps by more than four orders of magnitude at the 3σ confidence level in

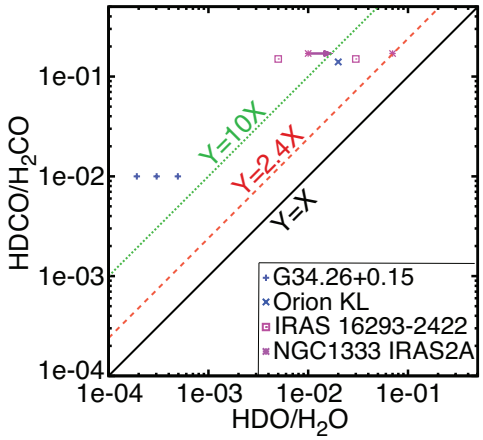

Figure 4.17 Diagram of HDO/H_2O vs. $HDCO/H_2CO$. Data are taken from Table 6.1.

G34.26+0.15. Similarly to this work, jump models are widely used to analyze the HDO and H_2O spectra of other high- and low-mass sources in Table 6.1, except for Orion KL. Ices are therefore also shown to evaporate from the grains in the inner part of the envelope in protostars of different masses. However, the D/H ratios of water in G34.26+0.15 is much lower than in low-mass protostars and similar to that in AFGL 2591 and other high-mass sources, such as Ori-IRc2, G31.41+0.31, and G10.47+0.03A (van der Tak et al. 2006; Gensheimer et al. 1996). In addition, the D/H ratios of formaldehyde and HCN in G34.26+0.15 are also lower than those in low-mass protostars. This can be explained if the dense and cold pre-collapse phase only lasts a short time and less CO freezes onto grain mantles. This hypothesis has been confirmed in the high-mass source AFGL 2591(van der Tak et al. 2006).

Figure 4.17 shows the diagram of HDO/H_2O vs. $HDCO/H_2CO$ and the values are taken from Table 6.1. It is found that the fractionation of water is at least $\sim$2.4 times lower than that of formaldehyde. This under-fractionation of water is found to be the most extreme for G34.26+0.15. One possible explanation is that if two molecules are mainly formed on the grain surface, the different deuterium fractionation can be due to the different pathways of each ice formation in translucent clouds: using a very simple chemical network on the grains, Cazaux et al. (2011) showed that the deuteration of formaldehyde is sensitive to the gas D/H ratio during the cloud collapse, while the deuteration of water depends on the dust temperature when ices form. More realistic models including water formation routes involving O_2 and O_3 also predict a higher fractionation of formaldehyde than water (Du et al. in prep.). However, recent studies showed that formaldehyde can also be formed in the gas phase from photodissociation reactions of grain species (Roueff et al. 2006). Formaldehyde can also efficiently be fractionated in the gas phase up to warm temperatures ($\sim$ 70K), through the CH_2D^+ route (Turner 2001; Roueff et al. 2007; Parise et al. 2009). It is therefore likely that the $HDCO/H_2CO$ ratio observed in the gas is not directly the result of grain chemistry. A better comparison would be with methanol fractionation, which is generally thought to form essentially on the grains.

Confirming the observed trend of under-fractionation of water would require observationally characterizing the deuterium fractionation (for both water and methanol) toward a bigger sample of sources, spanning a large mass interval. This under-deuteration of water with respect to other species is an important feature, which should be reproduced by astrochemical models aiming at explaining deuterium fractionation.

4.6 Conclusion

We presented five HDO transitions observed with APEX and two HDO high-excitation transitions observed with SMA toward the high-mass protostar, G34.26+0.15. With the 1D radiative transfer code RATRAN, and the physical profiles obtained from Rolffs et al. (2011), we derived the HDO fractional abundances relative to H_2 in the inner and outer region of the core to be $X_{\rm in}^{\rm HDO} = 6 \times 10^{-8}$ (T > 100 K) and $X_{\rm out}^{\rm HDO} = 5 \times 10^{-12}$ (T ≤ 100 K). This result shows that the HDO abundance is enriched in the inner region because of the sublimation of the ice in the same way as for other studied low- and high-mass sources, such as NGC1333 IRAS 2A, IRAS 16293-2422, and AFGL 2591 (Liu et al. 2011; Parise et al. 2005a; Coutens et al. 2012; van der Tak et al. 2006).

Although the abundance can be constrained, the HDO line profiles are not well reproduced, especially for the ground-state lines. We found that the fitted emission can be improved with two-jump models, suggesting the enhancement of the fractional abundance in the hot core. Modifying the physical profile, we showed that the velocity field is responsible for the HDO line profile at 893 GHz. Higher angular resolution observations of the HDO 893 GHz line are needed to constrain the velocity profiles of deuterated water in G34.26+0.15.

The H_2O abundance is estimated from one high-excitation and one ground transition para-$H^{18}O$ line (Gensheimer et al. 1996; Wyrowski et al. 2010). The D/H ratios of water are 3.0×10^{-4} in the inner region and $(1.9 - 4.9)\times10^{-4}$ in the outer region of the core. The deduced HDO/H_2O ratios in G34.26+0.15 are similar to those in other high-mass sources, such as AFGL 2591 (van der Tak et al. 2006), and are much lower than in low-mass star-forming regions, suggesting the possibility that the dense and cold pre-collapse phase is short for high-mass stars. Water is also found to be less fractionated than other molecules such as formaldehyde and methanol. This confirms this characteristic, which was observed previously in other sources, and provids a challenge for chemical models of deuterium fractionation on grain surfaces.

Appendix

A Model analysis

A.1. Shell analysis

To analyze the discrepancy between the best-fit model based on the Rolffs physical profiles and the observed data for the two ground transitions (464 and 893 GHz), we first constrained the physical shells responsible for the emission and absorption features. To this end, we simulated new spectra by sequentially turning the abundance of HDO in the innermost shells to 0 (Figure A1). The jump around 0.02 pc is at the shell whose temperature is about 100 K (jump model) The green dashed line represents the model where the HDO abundance is zero in all inner regions of the core (model SH6). Figure A2 presents the synthetic spectra obtained with these different models (SH1 – SH6). Obviously there is almost no emission in any spectrum with model SH6, suggesting that all emission, including the emission in the 893 GHz spectrum, is produced in the inner region of the core. Therefore, although lowering the abundance in the inner region can help to reduce the emission in the 893 GHz line, it will also decrease the emission

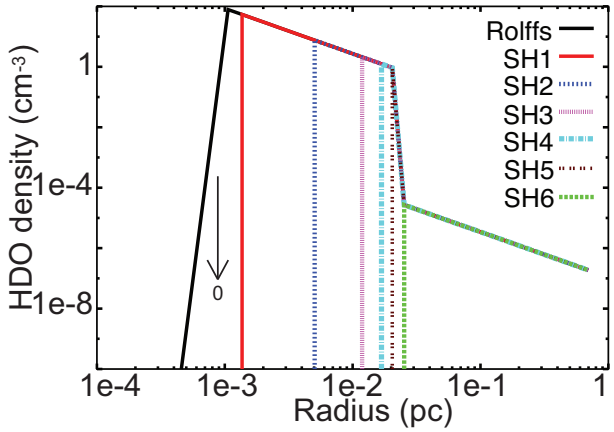

Figure A1 Original and modified molecular density profiles. The black line shows the original molecular density profile. Different colors indicate different molecular density profiles of models SH1 to SH6.

in other high-excitation lines (225, 241, and 266 GHz). On the other hand, the absorption in the 893 GHz spectrum is entirely produced in the outer region of the core and its line-width is wider than the observed one, implying that the assumed turbulent linewidth is wider than the observed one. Thus, we cannot adequately reproduce all spectra with the Rolffs original physical profiles.

A.2. Modified density profile

From previous test, it was found that the emission in the 893 GHz spectrum cannot be managed by the Rolffs physical profiles, but only by changing the HDO abundance. We therefore modified in the first place the density profile of the Rolffs model. Figure A3 compares the density profiles of three different modified models and original the Rolffs model (red line). Here we modified the density power law index (p), keeping the density at 0.1 pc fixed. The indices are 1.1 for model D1 (green), 1.7 for model D2 (dark-blue), and 2 for model D3 (purple). Modifying the density profile has a direct impact on the distribution of the continuum emission. The comparison of the radial profiles of the continuum emission of different models at multi-wavelength bands (225, 241, 335, and 848 GHz) is shown in Figure A4. Ignoring the misfitting parts within the beam (orange) and considering that free-free emission most likely also significantly contributes to the continuum emission, model D1 and the Rolffs model better reproduce the continuum emission in the 225 and 241 GHz bands than other models. For the 335 and 848 GHz band, the Rolffs model and all modified models are superior to the Nomura model. The best-fit results of each model are shown in Figure A5 (model D1: $1.0 \times 10^{-7}(\mathrm{X}_{\mathrm{in}}^{\mathrm{HDO}})$ and $1.0 \times 10^{-11}(X_{\mathrm{out}}^{\mathrm{HDO}})$; model D2: $5.0 \times 10^{-8}(X_{\mathrm{in}}^{\mathrm{HDO}})$ and $5.0 \times 10^{-12}(X_{\mathrm{out}}^{\mathrm{HDO}})$; model D3: $3.0 \times 10^{-8}(X_{\mathrm{in}}^{\mathrm{HDO}})$ and $5.0 \times 10^{-14}(X_{\mathrm{out}}^{\mathrm{HDO}})$). Comparing all spectra, we find that model D3 produced intensity similar to the Rolffs model in high-excitation lines and less emission in the 893 GHz line. However, the 464 and 893 GHz lines are optically thicker ($\tau = 2.9$ at 464 GHz and $\tau = 29.6$ at 893 GHz) than the lines produced by the Rolffs model. The high opacities result in self-absorption in the 464 and 893 GHz spectra (less emission). Moreover, results (464 and 893 GHz spectra) simulated with models D1 and D2 are very similar to the results produced with the original Rolffs model. Thus, we find that these models are not significantly better than the original the Rolffs model. In other words, the fits cannot be improved by simply modifying the density profile.

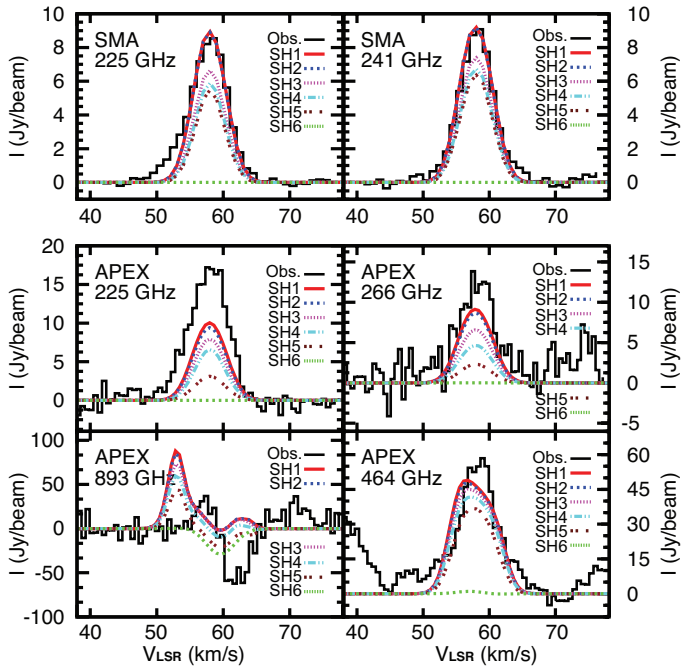

Figure A2 Comparison of the observed spectra with the results of 6 different shell models (Fig.A1). Different colors indicate the simulated lines of models SH1 to SH6. The observed and simulated spectra at 241 GHz are very similar to the spectra at 225 GHz; therefore, only the spectra at 225 GHz are plotted here.

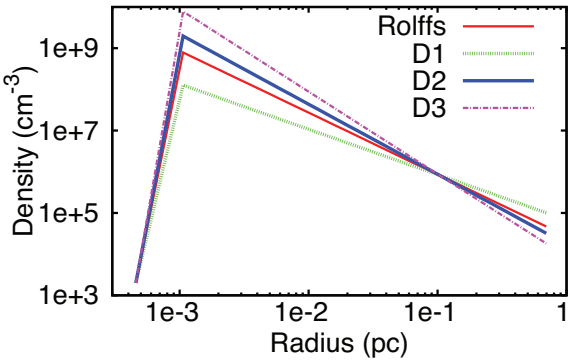

Figure A3 Comparison of the density profile of the three different modified models (blue, green, and pink) and original Rolffs' model (red).

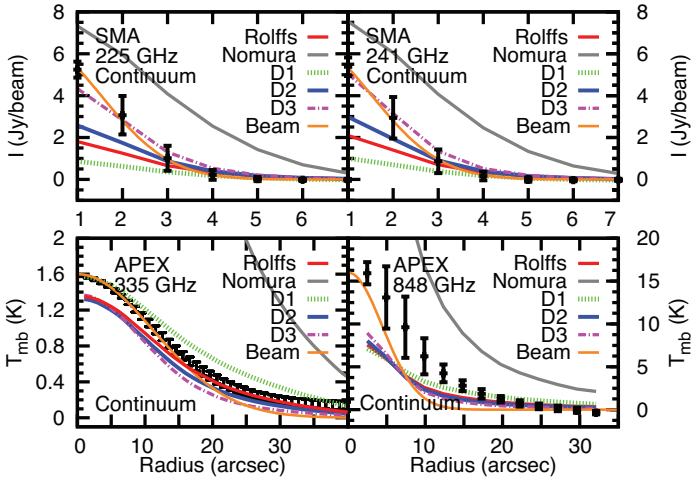

Figure A4 Radial profiles of the continuum emission at 225 (SMA), 241 (SMA), 356 (LABOCA, Rolffs et al. 2011), and 848 GHz (SABOCA, Wyrowski et al. in prep.) The modified models are overlaid in different colors (model D1 – green, D2 – dark-blue, and D3 – purple). The red and grey lines are reproduced profiles from the original Rolffs' and Nomura's models. The beam is shown as a orange dashed Gaussian. The errorbars represent only the deviation from a circular shape.

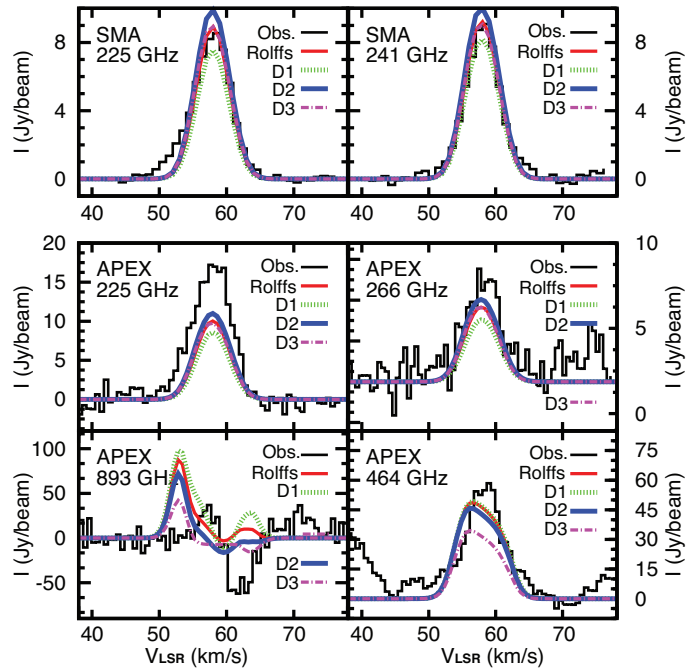

Figure A5 Comparison of the observed spectra with the best-fit results of 3 different models with modified density profiles (FigA3). The red lines are the best-fit model of the original Rolffs profile. The observed and simulated spectra at 241 GHz are very similar to those at 225 GHz; therefore, only the spectra at 225 GHz are plotted here.

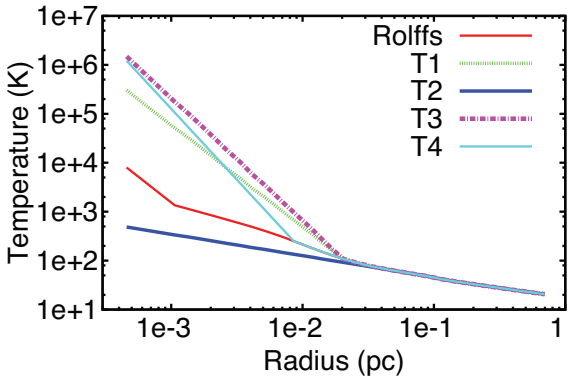

Figure A6 Comparison of the temperature profiles of the four different modified models (blue, green, light blue and purple) and the one of the original Rolffs model (red).

A.3. Modified temperature profile

To decrease the emission in 893 GHz spectra and maintain the emission in high-excitation lines (225, 241, 266 GHz), modifying the temperature profile is a possible way. We increased the temperature in the very inner region (models T1, T3, and T4) of the core and decreased the fractional abundance in the inner region of the core. The modified and original temperature profiles are shown in Figure A6. Model T2 contrasts with other models.

Like for changing the density profile, modifying the temperature profile also influences the continuum emission. Figure A7 compares the radial profiles of the continuum emission of different models in the four bands. Again, we find that the Rolffs model and all modified models are superior to the Nomura model in all bands. For the 225 and 241 GHz band, model T2 and the Rolffs model fit better, because the dust continuum is less than 25% of the total continuum flux, implying that increasing the temperature in the central region of the core is a poor solution. In the 335 and 848 GHz bands, T1, T2, and the Rolffs models are superior to others. The indistinguishable continuum at 848 GHz is due to a combination of optical depth and beam dilution effect: the temperature profile is changed only in the very central region of the core where the opacity is high and the beam size is much larger than the scale of the modified region (beam is $\sim 7.4''$ at 848 GHz and $2{\times}10^{-2}$ pc corresponds to $\sim 1.1''$). For 241 and 225 GHz, the angular resolution is sufficiently high and the opacity sufficiently low to detect the very inner region of the core.

To compare the effect on the spectra, Figure A8 shows the fitting results of the different modified models with a fixed HDO fractional abundance in the inner and outer region ($X_{\rm in}^{\rm HDO} = 6 \times 10^{-8}$ and $X_{\rm out}^{\rm HDO} = 5 \times 10^{-12}$). The fitting spectra of the T1 and T4 models are similar to spectra of the Rolffs model in the high-excitation spectra at 225 and 241 GHz, while the T2 model produces less emission in all spectra. However, models T1, T3, and T4 produce much poorer fits to the two ground-transition spectra, and T2 already becomes optically thick ($\tau = 3.4$) at 464 GHz. Hence, simply modifying the temperature profiles does not improve the agreement between the model and the observations.

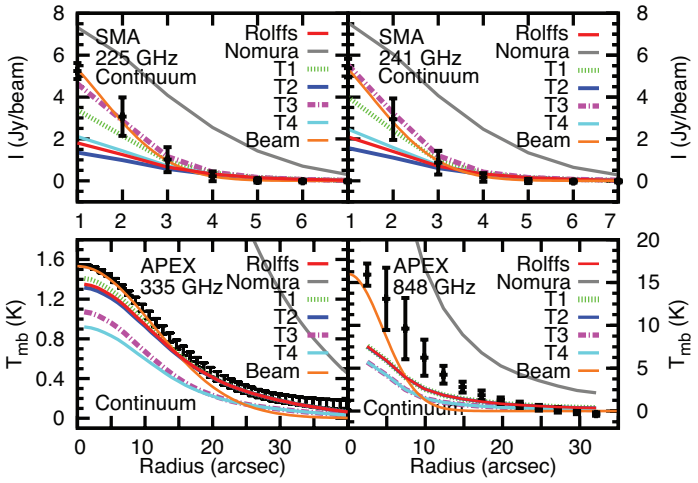

Figure A7 Same as Fig. A5, but for the modified temperature models.

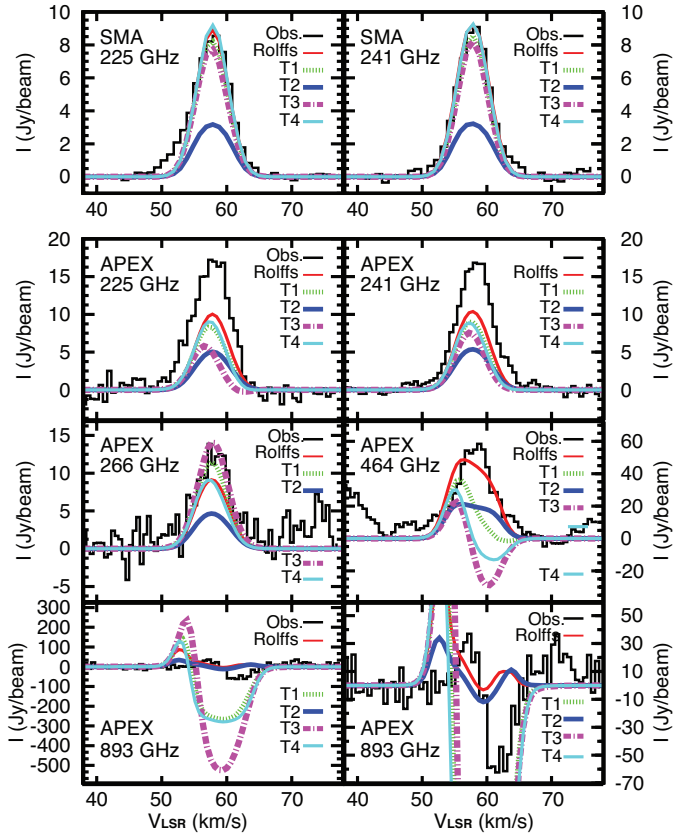

Figure A8 Comparison of the observed spectra and those reproduced with the fixed fractional abundances of models T1 to T4. The red lines are the best-fit model with the Rolffs original density profile.

Chapter 5

Water deuterium fractionation in a sample of luminous high-mass sources

5.1 Introduction

Singly deuterated water (HDO) has been studied towards many high-mass star-forming regions with ground-base telescopes (Jacq et al. 1990; Gensheimer et al. 1996; van der Tak et al. 2006). These studies mainly focus on the D/H ratios in the hot regions, because the HDO ground-transition line at 893 GHz and $H_2^{18}O$ ground-transition line at 1101 GHz could not be detected in the past. These ground-transition lines are necessary to constrain HDO and $H_2^{18}O$ abundances in cold envelopes. Recently, the HDO and the $H_2^{18}O$ ground-transition have been observed with APEX and the Herschel Space Observatory. We therefore can study the HDO/H_2O ratio in many high-mass star-forming regions throughout the whole envelope. The high-mass hot core G34.26+0.15 is the first source in which the D/H ratio has been studied in detail in both warm and cold envelopes. The G34.26+0.15 study shows that the HDO/H_2O ratio in both the warm and cold envelopes is much lower than in low-mass star-forming regions, implying the possibility that the dense and cold pre-collapse phase is shorter for high-mass stars. In this chapter, we expand the study of the D/H ratios of water to five luminous high-mass sources with the HDO high-excitation and ground-transition lines and then compare with the $H_2^{18}O$ high-excitation and ground-state transition lines to understand the water deuterium fractionation in high-mass star-forming regions.

5.2 Observations

5.2.1 Single-dish observations

We observed several HDO transitions with the APEX and Herschel space telescopes. The sources and the observed HDO lines are list in Table 5.1. All the APEX data were taken between 2007 to 2010 with the wobbler-switching mode with a throw of 240″. The temperature scale was converted from T_A^* to

Table 5.1. Sources and HDO observations

Source	RA (J2000)	Dec (J2000)	$V_{\rm LSR}$ (km/s)	$L^e_{\rm bol}$ ($L_\odot$)	M^e ($M_\odot$)	observed HDO lines[a]	observed $H_2^{18}O$ lines[d]
W51E	19:23:43.91	+14:30:28.2	+56	1.0(5)[f]	4.5(3)[f]	225, 241, 266, 464, 893	1101[b] & 390[c]
IRAS 16065-5158	16:10:20.01	−52:06:13.2	−62	2.9(5)[h]	3.6(3)[h]	225, 241, 464, 893	390[c]
G351.58-0.35	17:25:25.28	−36:12:44.8	−96	2.4(5)[g]	7.4(3)[g]	225, 241, 266, 464, 827, 848, 893	1101[b] & 390[c]
G327.3-0.6	15:53:07.80	−54:37:06.4	−45	8.2(4)[g]	2.4(3)[g]	225, 241, 464, 893	1101[b] & 390[c]
G10.47+0.03	18:08:38.25	−19:51:50.1	+69	3.7(5)[f]	1.1(3)[f]	225, 241, 266, 464, 893	1101[b] & 390[c]

[a] Rest frequencies (in GHz) of the observed HDO lines. Detail information are in Table 5.2.

[b] WISH project

[c] Wyrowski et al. in prep.

[d] Rest frequencies (in GHz) of the observed $H_2^{18}O$ lines.

[e] The numbers in parentheses are powers of 10.

[f] van der Tak et al. (2013) [g] Wyrowski et al. (2016) [h] Rolffs et al. (2011)

$T_{\rm mb}$ using the beam efficiencies indicated in Table 5.2, which we took from the APEX[1] and CHAMP^{+}[2] websites. The other characteristics of the HDO observations are listed in Table 5.2.

5.2.2 Interferometer observations

The interferometer observations toward G10.47+0.03 were carried out on 2011 April 26 and May 10 with the Submillimeter Array (SMA) on Mauna Kea, Hawaii. We used the 230 GHz receivers to observe the 225 and 241 GHz lines as well as the 1.3 mm continuum simultaneously. The primary-beam size (HPBW) of the 6-m-diameter antennas at 230 GHz is $\sim 54''$. The phase tracking center of this observation is the same as for the APEX observations. The frequency coverages are 225.76 – 229.73 GHz in the lower sideband and 237.73 – 241.71 GHz in the upper sideband and each band is divided into 48 chunks. A hybrid resolution mode was set with 512 channels per chunk (16.2 kHz resolution) for the HDO $J_{K_-K_+}$=$3_{1,2} - 2_{2,1}$ line, and 256 channels per chunk (32.4 kHz) for the HDO $J_{K_-K_+}$=$2_{1,1} - 2_{1,2}$ line.

The visibility data were calibrated using the MIR software package, which was originally developed for the Owens Valley Radio Observatory. The absolute flux density scale was determined from observations of Neptune for all data. The pair of nearby compact radio sources 1743-038 and 1911-201 were used to calibrate relative amplitude and phase. We used 3C279 to calibrate the bandpass.

The calibrated visibility data were Fourier transformed and CLEANed using the MIRIAD package. The map was made using uniform weighting. The synthesized beam size was $3\farcs4\times2\farcs5$ with a position angle of –64°. The continuum map was obtained by averaging all line-free channels in the two bands except chunks s44-s48 because they have different frequency resolution.

[1] http://www.apex-telescope.org/telescope/efficiency/index.php

[2] http://www3.mpifr-bonn.mpg.de/div/submmtech/heterodyne/champplus/champ_efficiencies.16-09-14.html

Table 5.2. Details of the APEX HDO observations

Frequency (GHz)	Transition	E_{up} (K)	n^a_{cr}(para-H_2) (cm^{-3})	n^a_{cr}(ortho-H_2) (cm^{-3})	HPBW ($''$)	B_{eff}	Receiver
225.897	$3_{1,2}$–$2_{2,1}$	167.7	9.91×10^7	2.20×10^7	27.85	0.75	APEX-1
241.561	$2_{1,1}$–$2_{1,2}$	95.3	3.53×10^7	8.78×10^6	26.04	0.75	APEX-1
266.161	$2_{2,0}$–$3_{1,3}$	157.2	1.21×10^9	2.93×10^8	23.64	0.75	APEX-1
464.924	$1_{0,1}$–$0_{0,0}$	22.3	1.71×10^6	3.69×10^5	13.53	0.60	FLASH/PI460
827.263	$4_{1,3}$–$3_{2,2}$	263.3	2.44×10^8	5.17×10^7	7.60	0.36	CHAMP$^+$
848.962	$2_{1,2}$–$1_{1,1}$	83.6	1.89×10^8	4.29×10^7	7.42	0.36	CHAMP$^+$
893.639	$1_{1,1}$–$0_{0,0}$	42.9	5.72×10^7	1.47×10^7	7.04	0.36[c]	CHAMP$^+$[d]

[a] Critical density at 100 K calculated by using the values of the Einstein coefficient and the collision rates tabulated for HDO (Faure et al. 2012) in the LAMDA database (http://www.strw.leidenuniv.nl/moldata/).
[b] The resolution of the original settings in the observations.
[c] 0.35 for G327.3-0.6 observed in 2008.
[d] The HDO 893GHz line was also observed toward G327.3-0.6 and IRAS 16065-5158 with the Herschel space telescope in 2011. The beam efficiency is 0.75.

5.3 Results

5.3.1 Single-dish Observations

Table 5.3 summarizes the properties of the observed HDO lines (Figure 5.3 to Figure 5.7). Most HDO lines are detected, except for the 893 GHz line in IRAS 16065-5158. HDO 225 GHz lines observed toward W51E and G327.3-0.6 are blended with an emission line at $\sim$ 225.900 GHz, which could be either C_2H_3CN or C_2H_5CN. Because the two ground-state lines are always suspected to be optically thick (Liu et al. 2011, 2013), we used the integrated intensities of excited HDO lines to perform a rotation diagram analysis with the assumption that the lines are optically thin and in local thermodynamic equilibrium (LTE) (Goldsmith & Langer 1999). We also assumed source sizes for each source, as suggested from the SABOCA or SMA observations (Table 5.4). Because these sizes are smaller than the APEX beams at the three observed frequencies, the derived column densities and source sizes are degenerate. Nevertheless, the temperature does not depend on the size assumption for optically thin emission. The resulting rotation diagrams are displayed in Figure 5.1 and the obtained rotation temperatures and total molecular column densities are listed in Table 5.4. Most values of the rotation temperatures and the column densities of the hot HDO are consistent with the estimates of previous studies (Table 5.4). The only exception is the HDO column density for G10.47+0.03. This is because the source size we assumed ($\sim 1.5'' \times 1.0''$) is much smaller than that used in a previous paper ($\sim 12'' \times 12''$, Gensheimer et al. (1996)). After applying the (beam) dilution factor, the HDO column densities averaged on the assumed beam size $12''\times12''$ in G10.47+0.03 is 4.8×10^{15} cm^{-2}, which is in good agreement with the value in the literature.

Table 5.3. Properties of the HDO lines

Freq. (GHz)	dv[a] (km/s)	rms[ce] (mK)	$T_{\rm peak}^{ce}$ (K)	$V_{\rm LSR}^{e}$ (km/s)	Δv[de] (km/s)	$\int T_{\rm mb}$dv[e] (K km/s)
W51E						
225[f]	0.49	40	0.33	57.2±0.7	7.2±1.7	2.5±0.5
241	0.45	37	0.34	56.7±1.4	8.3±3.4	3.0±1.1
266	0.83	28	0.18	55.7±0.4	11.3±1.3	2.2±0.2
464	0.31	188	2.49	56.6±0.4	10.5±0.8	27.9±1.8
893[g]	0.49	293	-0.75[b]	-58.4±0.6[b]	6.0±1.9[b]	-4.8±1.1[b]
893[h]	0.49	293	-1.97[b]	-69.4±0.1[b]	0.9±0.2[b]	-1.9±0.5[b]
IRAS 16065-5158						
225	0.97	18	0.11	-61.2±0.3	7.9±0.7	0.9±0.1
241	0.90	25	0.09	-61.7±1.6	9.5±4.2	0.9±0.3
464	0.31	132	0.67	-62.2±0.2	7.8±0.5	5.6±0.3
G351.58-0.35						
225	0.49	36	0.20	-96.8±0.2	6.9±0.6	1.5±0.1
241	0.45	25	0.20	-95.6±0.2	6.8±0.5	1.4±0.1
266	1.65	28	0.10	-95.9±0.6	9.9±1.3	1.0±0.1
464	0.20	107	0.93	-96.4±0.6	9.2±2.4	9.2±1.6
827	1.06	543	2.00	-94.3±0.7	9.7±1.8	20.7±3.2
848	0.52	759	2.08	-94.9±1.1	9.2±2.1	20.3±4.6
893[i]	0.49	732	-8.51[b]	-94.2±0.1[b]	3.2±0.2[b]	-29.2±2.4[b]
893[j]	0.49	732	-2.02[b]	-99.1±0.7[b]	4.1±0.2[b]	-18.3±2.6[b]
G327.3-0.6						
225[f]	0.16	73	0.84	-44.4±0.1	6.8±0.4	6.1±0.3
241	0.15	67	0.88	-44.4±0.4	5.6±0.8	6.0±1.1
464	0.63	313	1.17	-45.8±1.8	13.8±3.5	17.2±4.4
893[i]	0.49	443	-3.31[b]	-44.4±0.2[b]	3.1±0.4[b]	-11.0±1.6[b]
893[j]	0.49	443	-1.83[b]	-51.1±0.7[b]	10.0±1.3[b]	-19.5±2.4[b]
G10.47+0.03						
225	0.97	24	0.47	66.4±0.3	10.2±0.7	5.1±0.3
241	0.45	36	0.42	66.1±0.4	9.6±0.9	4.3±0.3
266	0.83	35	0.30	65.3±0.3	14.0±0.8	4.5±0.2
464	0.31	136	1.62	67.7±0.6	9.5±1.7	16.3±5.6
893[i]	0.49	413	-1.37[b]	68.0±0.3[b]	3.5±0.8[b]	-5.1±1.4[b]
893[j]	0.49	413	-0.69[b]	58.8±1.9[b]	16.6±3.2[b]	-12.3±2.4[b]

[a]Resolution [b]Only the absorption part [c]$T_{\rm mb}$ scale [d]Measured line widths

[e]Value is derived from gaussian fit using the software CLASS. The uncertainties only include the statistical noise, and not the calibration uncertainties.

[f]Blended with an emission line at 225.900 GHz, which possibly to belong to C_2H_3CN or C_2H_5CN or both. A two gaussian fit is used here to deconvolve the lines and then obtain the values of the HDO 225 line.

[g]The absorption at the $V_{\rm LSR}$ of 58.4 km/s.

[h]The absorption at the $V_{\rm LSR}$ of 69.4 km/s.

[i]The wide-blue-shifted absorption

[j]The narrow absorption at the system velocity

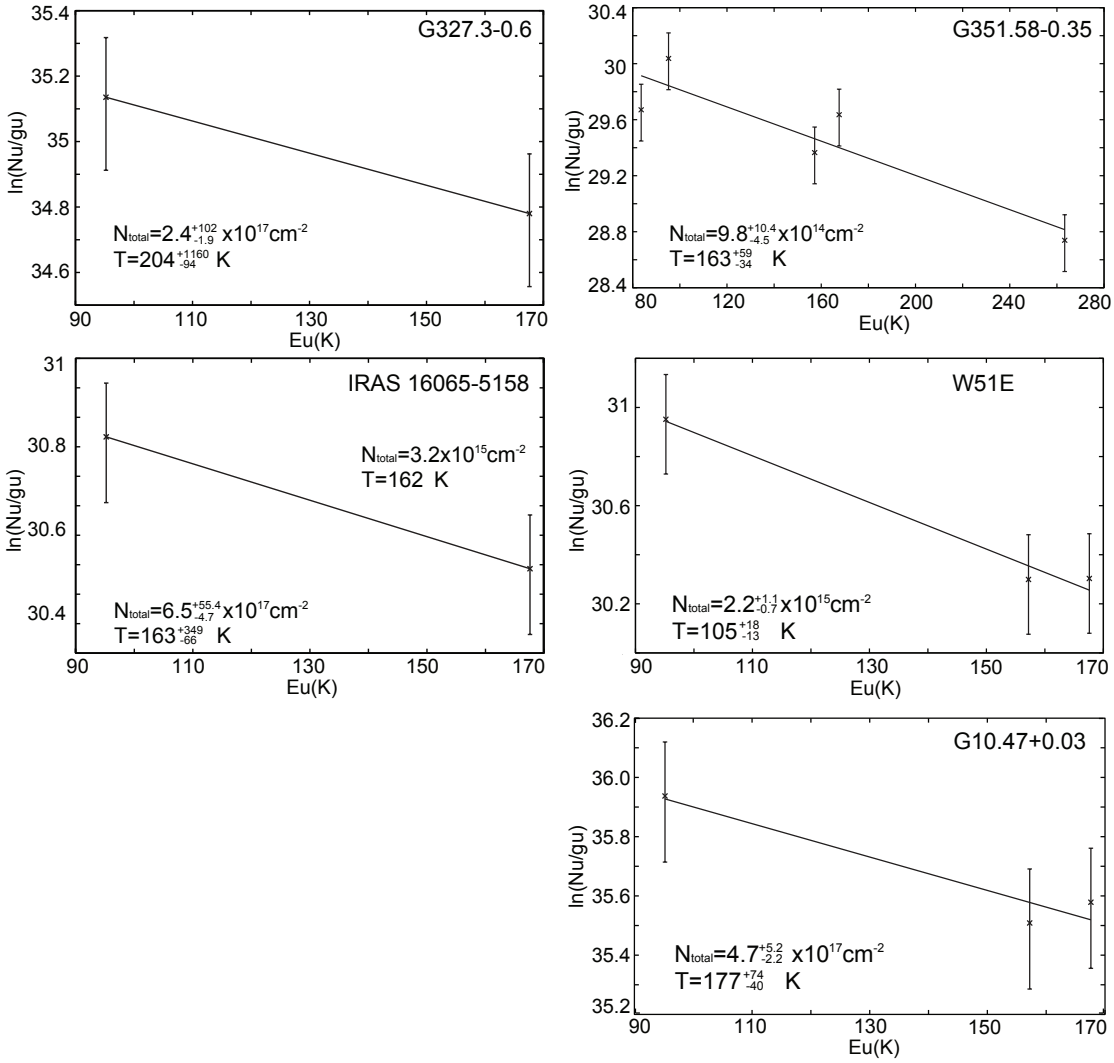

Figure 5.1 HDO rotation diagrams. The detected lines are shown as crosses with error bars.

Table 5.4. Parameters and results of the rotation diagram

Source	Source size ($'' \times ''$)	Beam size ($'' \times ''$)	$T_{\rm rot}$ (K)	HDO column density[a] ($\rm cm^{-2}$)	HDO column density[j] ($\rm cm^{-2}$)	T^b (K)	HDO column density[c] ($\rm cm^{-2}$)
W51E	16.0×11.0^d	$7.4\times\ 7.4^d$	105^{+18}_{-13}	$2.2^{+1.1}_{-0.7}\times10^{15}$	2.7×10^{15}	$T_{\rm rot} = 103\pm9$ K (CH_3CH_2CN)[h]	2.1×10^{15} [i]
IRAS 16065-5158	$6.4\times\ 3.1^f$	$5.0\times\ 5.0^f$	163^{+349}_{-66}	$6.5^{+55.4}_{-4.7}\times10^{15}$	8.3×10^{14}	$T_{\rm rot} < 250$ K (CH_3CN & SO_2)[j]	...
G351.58-0.35	16.1×13.3^d	$7.4\times\ 7.4^d$	163^{+59}_{-34}	$9.8^{+10.4}_{-4.5}\times10^{14}$	3.6×10^{14}	...	...
G327.3-0.6	$2.0\times\ 2.0^g$	...[g]	204^{+1160}_{-94}	$2.4^{+102}_{-1.9}\times10^{17}$	6.7×10^{15}	$T_{\rm ex} \leq 300$ K (CH_3CN & C_2H_5CN)[k]	$>2.2\times10^{14}$ [g]
G10.47+0.03	$1.5\times\ 1.0^e$	$3.8\times\ 2.7^e$	177^{+74}_{-40}	$4.7^{+5.2}_{-2.2}\times10^{17}$	4.8×10^{15}	$T_{\rm rot}$ = 140 – 160 K (CH_3CN)[l]	3.3×10^{15} [m]

[a] This work. The derived values are the total molecular column densities of the hot HDO averaged on the assumed source size.

[b] The values are derived with other molecules.

[c] from other papers.

[d] Value is measured with SABOCA maps using the task IMFIT of the MIRIAD package.

[e] Value is measured with SMA map using the task IMFIT of the MIRIAD package.

[f] Dedes et al. (2011), observed with the Australia Telescope Compact Array.

[g] Gibb et al. (2000), source size is obtained from the population diagram analysis.

[h] Demyk et al. (2008) [i]Jacq et al. (1990) [j]Dedes et al. (2011) [k]Schilke et al. (2006)

[i] Olmi et al. (1996) [m]Gensheimer et al. (1996), observed with the IRAM 30m (Beam $\sim 11''$).

[j] The total molecular column densities of the hot HDO averaged on the assumed beam size $12''\times12''$.

This values is estimated by applying the (beam) dilution factor to the obtained total HDO column densities (previous column).

Table 5.5. Results of the SMA observations toward G10.47+0.03

	Beam ($'' \times ''$)	Freq. (GHz)	rms (Jy/Beam)	Integrated flux[a]	Peak position[a] RA(J2000) DEC(J2000)	Positional error[b] ($''$) ($''$)	Deconvolved size[a] ($''$)
HDO 225	$3''.92 \times 2''.81$	225.9	0.08	94.8 Jy·km/s	$18^h08^m38^s.25$ $-19^o51^m50^s.53$	0.02 0.02	$1''.09 \times 0''.92$
HDO 241	$3''.64 \times 2''.60$	241.6	0.16	73.9 Jy·km/s	$18^h08^m38^s.25$ $-19^o51^m50^s.48$	0.03 0.03	$1''.25 \times 0''.91$
1.3 mm	$3''.76 \times 2''.69$	234.4	0.10	5.5 Jy	$18^h08^m38^s.25$ $-19^o51^m50^s.43$	0.02 0.03	$1''.28 \times 0''.37$

[a]Values are obtained from a Gaussian fit using the task IMFIT of the software MIRIAD.
[b]Values are derived from the theoretical formula $\sigma_{position} = FWHM/[\sqrt{8\ln 2} \cdot (S/N)]$ (Condon 1997).

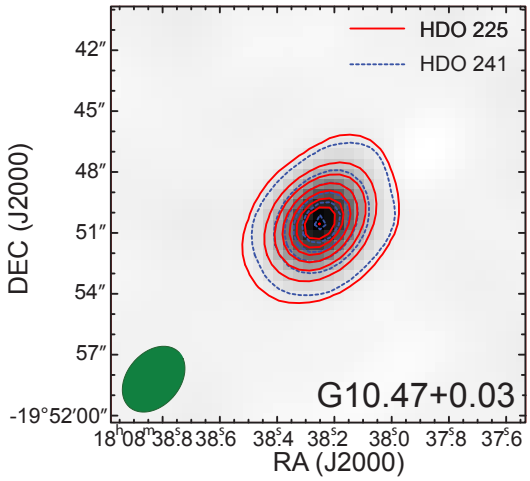

Figure 5.2 HDO 225 GHz (red contours)/HDO 241 GHz (blue-dashed contours) integrated map and 1.3 mm continuum map (grey scale) observed with the SMA toward G10.47+0.03. The contour levels are from 3 σ by steps of 12 σ, with 1 σ = 1.0 Jy beam^{-1}. The green ellipse indicates the beam size.

5.3.2 G10.47+0.03

5.3.2.1 Interferometer observations

The results of the interferometer observations are shown in Table 5.5 and Figure 5.2. The integrated intensity maps of the two HDO lines show that their distributions are very similar, suggesting that their emission comes from the same gas. In addition, the position of the peak of the HDO emission is very close to that of the 1.3 mm dust continuum (Table 5.5), implying that the distribution of the HDO is the same as the distribution of the 1.3 mm continuum.
Comparing the results observed with APEX, we find that the missing flux of the HDO 225 GHz and 241 GHz line emission is $\sim$34.1% and $\sim$34.4%. These values suggest that most HDO emission is coming from the center of the molecular cloud core, which is consistent with the fact that the line shapes are very similar. Here, the SMA map was convolved with the beam size of APEX after the primary beam correction was done. The SMA probes scales up to $32''$, which is much larger than the expected spatial extension of these high excitation HDO lines. In view of their critical density and energy, it is unlikely

Table 5.6. The adopted parameters of the Models

Source	source model	distance kpc	opacity[a]	turbulence width km/s
W51E	(1) & (2)	5.4[(1)] & 5.1[(2)]	bare, 10^5 cm^{-3}[(1)] & thin, 10^6 cm^{-3}[(2)]	1.0–4.0[(1)] & 2.0–2.5[(2)]
IRAS 16065-5158	(1)	4.0	bare, 10^5 cm^{-3}[(1)]	3.5
G351.58-0.35	(3)	6.8	thin, 10^5 cm^{-3}[(3)]	1.9–2.4
G327.3-0.6	(2)	3.3	thin, 10^6 cm^{-3}[(2)]	2.1–2.5
G10.47+0.03	(1) & (2)	10.5[(1)] & 5.8[(2)]	bare, 10^5 cm^{-3}[(1)] & thin, 10^6 cm^{-3}[(2)]	1.8–3.8[(1)] & 2.2–3.6[(2)]

[(1)] Rolffs et al. (2011) [(2)] van der Tak et al. (2013) [(3)] Wyrowski et al. (2016)

[a] Different opacities are from Ossenkopf & Henning (1994)

that the apparent missing flux is real. The calibration uncertainties of APEX and SMA are usually considered to be ∼20% and 5–15%. We therefore assume that the flux discrepancy is originating from the uncertainties of the calibration.

5.4 Modeling

5.4.1 Model description

To analyze the HDO data, we used the 1 D Monte Carlo code RATRAN, developed by Hogerheijde & van der Tak (2000) (see Chapter 2.3.1). The radiative transfer model takes as input the physical (n, T) profiles of the source. The adopted source models we used are listed in Tab. 5.6. The physical profiles, which correspond to the van der Tak and Wyrowski models (van der Tak et al. 2013; Wyrowski et al. 2016), are constrained by the observed spectral energy distribution (SED) data and the radial intensity profiles of the continuum maps. The density and temperature profiles of the Rolffs model (Rolffs et al. 2011) aim to reproduce the radial intensity profile from LABOCA data (345 GHz continuum). Centrally heated envelopes and infall velocity fields are assumed for all sources. The adopted distance, opacity, and turbulence are listed in Tab. 5.6. The HDO collisional rates used in this study have been computed by Faure et al. (2012) for para-H_2 and ortho-H_2 separately. In the modeling, we assumed that the ortho-to-para ratio of H_2 is in LTE in each cell of the core.

For most sources, we have APEX and Herschel data, so the modeled maps were convolved with the APEX and Herschel beams. For G10.47+0.03, in order to also compare with the SMA data, we used MIRIAD to create mock observations based on the modeled data and then obtained the simulated maps/spectra (see Section 4.4.2).

We then performed χ^2 analyses to constrain the HDO abundance for all spectra of each source. Here the definition of χ^2 is $\Sigma\frac{(T_{mb,ob}-T_{mb,mod})^2}{\sigma^2}$, where the sum is over the channels in each spectrum. The σ within this χ^2 analysis only includes the statistical errors of spectra.

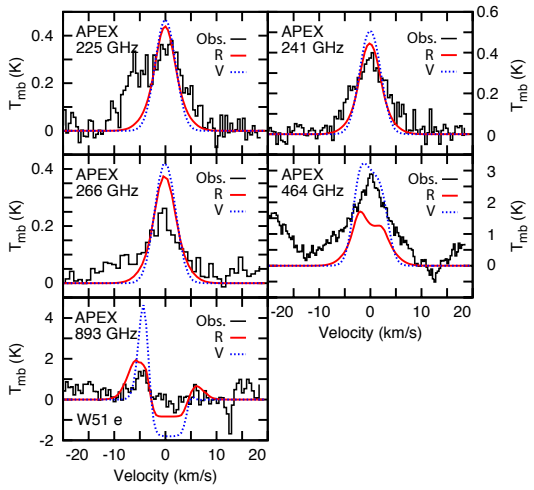

Figure 5.3 Lines towards W51e. Comparison of the observed spectra with the results of our best-fit models for the two different physical profiles. The observed line emission is shown as a black histogram in each spectrum. The red and blue-dashed lines show the best-fit results of the Rolffs model and the van der Tak model, respectively. The x axis is the velocity relative to the source velocity of W51e ($V_{\rm LSR}$=56 km/s, see Table 5.2).

5.4.2 Modeling results

An abundance jump model for HDO with sublimation at an assumed jump temperatures $T_{\rm j}$ of 100 K and release into the gas phase by thermal desorption, has been widely used in past studies of water and deuterated water in star-forming regions (e.g. Parise et al. 2005a; van der Tak et al. 2006; Liu et al. 2011; Herpin et al. 2012; Liu et al. 2013). Therefore, we also adopted such an abundance jump for the HDO lines in a first round of modeling ($X_{\rm in}^{\rm HDO}$, T $>$ 100 K and $X_{\rm out}^{\rm HDO}$, T $<$ 100 K, where the fractional abundances of deuterated water in the inner and outer regions). We then performed a grid of models with various inner and outer abundances and realized that the intensities of the different lines cannot be well reproduced simultaneously (see Fig. 5.3 to Fig. 5.7), except for the lines observed toward IRAS 16065-5158 (see Fig. 5.4).

In the cases of W51 e and G351.58-0.36 (Fig. 5.3 and 5.5), when the excited transitions observed at 225 and 241 GHz are reproduced, other transitions are overproduced or become too optically thick. In addition, in the cases of G327.3-0.6 and G10.47+0.03 (Fig. 5.6 and Fig. 5.7), even the reproduced HDO spectra (225 GHz and 241 GHz) show obviously self-absorption features, so the fits are not good enough to determine the abundances.

In order to reproduce the emission in the high-excitation lines and decrease/enhance the emission in the ground transition lines, we tried modeling the spectra with a two-jump model instead of a one-jump model for the four sources (W51e, G351.58-0.36, G327.3-0.6, and G10.47+0.03). However, the results suggest that this modification cannot improve the results; an example is given in Fig. 5.8. This property has already been found for G34.26+0.15 (see Section. 4.5.1). Although the modifications of the velocity profiles can affect the line profiles, the line intensities are still not significantly modified to decrease this disagreement.

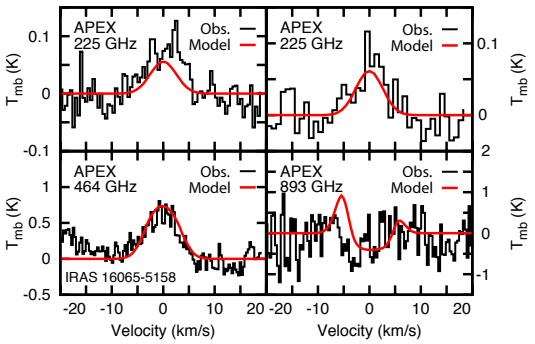

Figure 5.4 Lines towards IRAS 16065-5158. Comparison of the observed spectra with the results of our best-fit models ($X_{\rm in}^{\rm HDO} = 2 \times 10^{-08}$ and $X_{\rm out}^{\rm HDO} = 1 \times 10^{-12}$). The observed line emission is shown as black histograms in each spectrum. The red lines show the best-fit results of the Rolffs model.

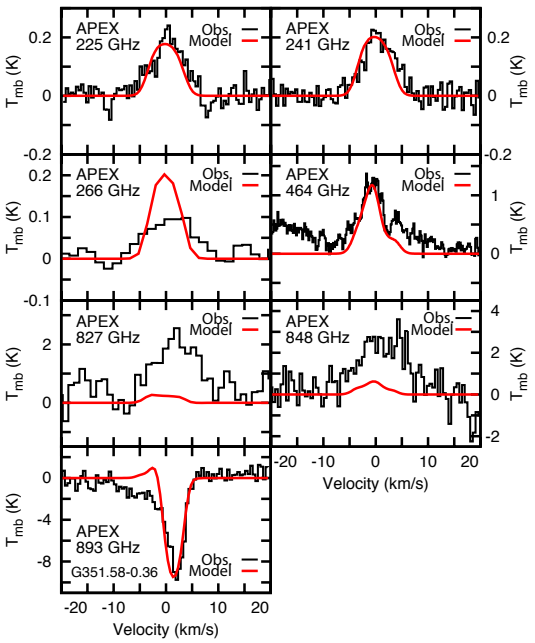

Figure 5.5 Lines towards G351.58-0.36. Comparison of the observed spectra with the results of our best-fit models. The observed line emission is shown as black histograms in each spectrum. The red lines show the best-fit results of the Wyrowski model.

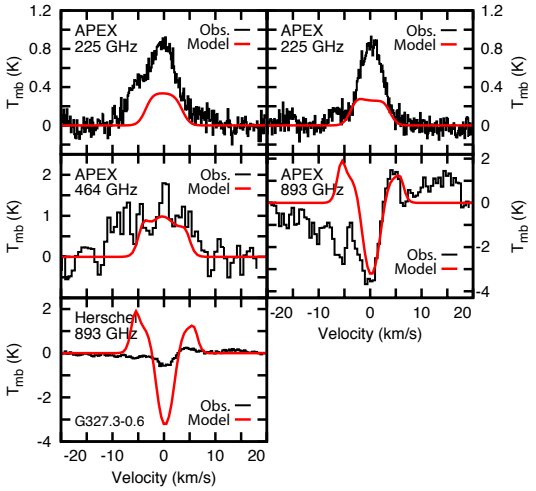

Figure 5.6 Lines towards G327.3-0.6. Comparison of the observed spectra with the results of our best-fit models. The observed line emission is shown as black histograms in each spectrum. The red lines show the best-fit results of the van der Tak model.

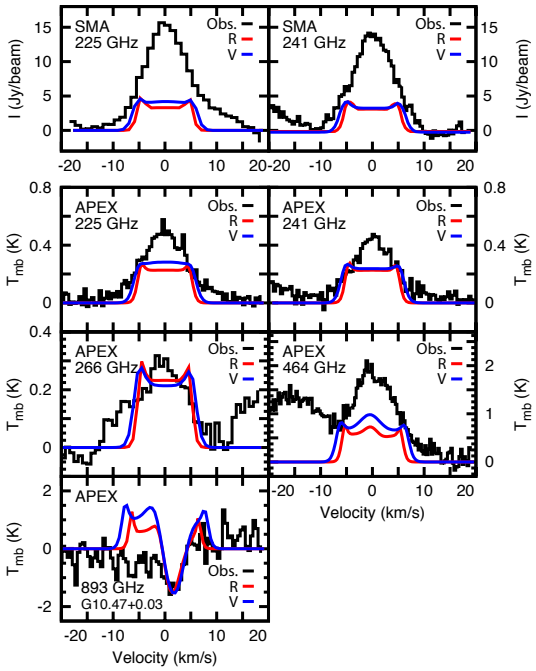

Figure 5.7 Lines towards G10.47+0.03. Comparison of the observed spectra with the results of our best-fit models for the two different physical profiles. The observed line emission is shown as black histograms in each spectrum. The red and blue-dashed lines show the best-fit results of the Rolffs model and the van der Tak model.

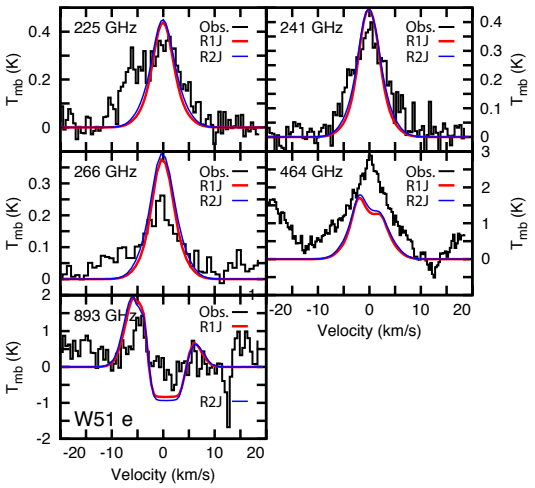

Figure 5.8 Lines towards W51e. Comparison of the observed spectra and those simulated with different models. The red and blue lines are the reproduced spectra of the one-jump model (R1J) and the two-jump model (R2J, T_{2j}= 200 K) with the physical profiles from Rolffs model.

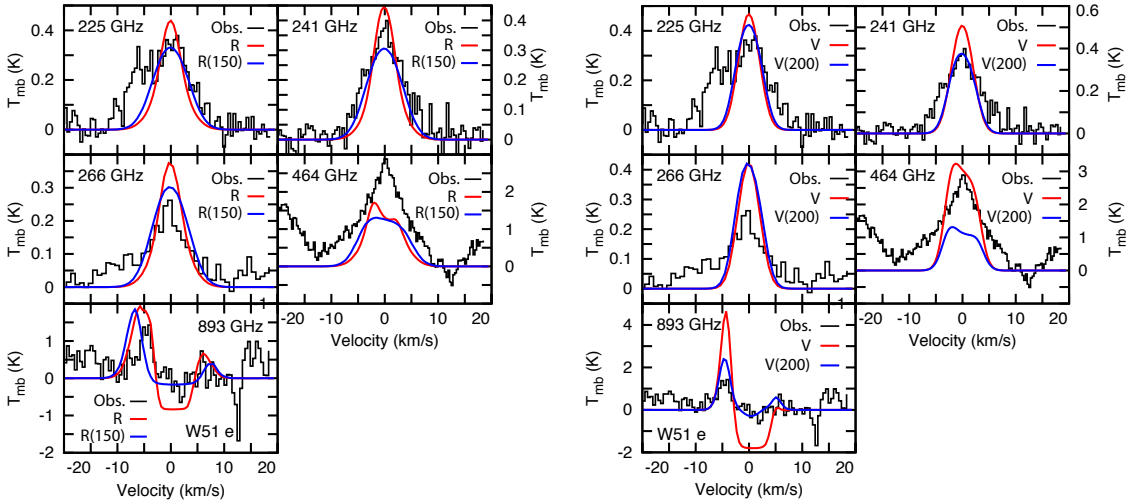

Figure 5.9 Lines towards W51e. Comparison of the observed spectra and those simulated with different sublimation temperatures, T_j. Left Panel: the red and blue lines are the reproduced spectra of the one-jump model with T_j= 100 K and with T_j= 150 K with the physical profiles from Rolffs model. Right Panel: the red and blue lines are the reproduced spectra of the one-jump model with T_j= 100 K and with T_j= 200 K with the physical profiles from van der Tak model.

Table 5.7. HDO and $H_2^{18}O$ abundances obtained with different jump temperatures Tj (W51e).

Models	Tj	θ^c	Best fit HDO abundances		$\chi^2_{\rm red}$	Best fit $H_2^{18}O$ abundances		$\chi^2_{\rm red}(H_2^{18}O)$		$(HDO/H_2O)^d_{in}$	
	K	$''$	inner region	outer region	(HDO)	inner region	outer region	inner region[e]	outer region[e]	inner region	outer region
R model[a]	100	1.4	5×10^{-08}	1×10^{-14}[f]	3.2	1.0×10^{-07}	2×10^{-11}	0.2	1.1	7.5×10^{-04}	...[f]
R model[a]	120	1.1	1×10^{-07}	1×10^{-14}[f]	3.0	2.0×10^{-07}	3×10^{-11}	0.3	1.1	7.5×10^{-04}	...[f]
R model[a]	150	1.0	1×10^{-07}	1×10^{-14}[f]	2.3	2.0×10^{-07}	3×10^{-11}	0.2	1.3	7.5×10^{-04}	...[f]
R model[a]	200	0.7	2×10^{-07}	1×10^{-12}[f]	2.6	5.0×10^{-07}	3×10^{-11}	0.5	1.4	6.0×10^{-04}	...[f]
V model[b]	100	2.0	5×10^{-08}	1×10^{-14}[f]	5.2	9.0×10^{-08}	9×10^{-11}	0.3	0.8	8.3×10^{-04}	...[f]
V model[b]	120	1.5	8×10^{-08}	1×10^{-13}[f]	4.1	1.0×10^{-07}	9×10^{-11}	0.6	0.8	1.2×10^{-03}	...[f]
V model[b]	150	1.2	2×10^{-07}	1×10^{-15}[f]	3.9	3.0×10^{-07}	9×10^{-11}	0.3	0.8	1.0×10^{-03}	...[f]
V model[b]	200	0.7	4×10^{-07}	1×10^{-12}[f]	3.8	6.0×10^{-07}	9×10^{-11}	0.4	0.8	1.0×10^{-03}	...[f]

[a] Rolffs et al. (2011) [b] van der Tak et al. (2013)

[c] Size of the region where the temperature is higher than Tj.

[d] Assuming $H_2^{16}O/H_2^{18}O = 500$.

[e] The $H_2^{18}O$ fractional abundance in the inner region and outer region is obtained by analyzing the $H_2^{18}O$ excitation transition at 390 GHz and the $H_2^{18}O$ ground transition at 1101 GHz, respectively.

[f] The HDO fractional abundance in the outer/cold region cannot be well constrained in the modeling and is not reliable, because the absorption is not clearly detected ($\sim$2.5σ detection, see Table 5.3). Therefore, we did not estimate the D/H ratios of water here.

In order to improve the fitting results for all the transitions, it is found that modifying the sublimation temperatures, $T_{\rm j}$, is necessary. For example, for W51e, with a jump temperature of 150 K (left panel in Figure 5.9: with Rolffs model–R(150)) and with a jump temperature of 200 K (right panel in Figure 5.9: with van der Tak model–V(200)), the models match the 893 GHz spectra than the models with a jump temperature of 100 K. Moreover, the better $\chi^2_{\rm red}$ of the model R(150) ($\chi^2_{\rm red}$=2.3) and the model V(200) ($\chi^2_{\rm red}$=3.9) show that the fits can be improved by modifying the sublimation temperatures (Table 5.7, $\chi^2_{\rm red}$ =3.2 and 5.2 when T$_j$=100 K). Therefore, for W51E, we ran grids of models for higher sublimation temperatures ($T_{\rm j}$ = 120, 150, and 200 K) and compared the influence of the jump temperature on the line intensities. Table 5.7 summarizes the best-fitting fractional abundances and the $\chi^2_{\rm red}$ values obtained with different jump temperature. Obviously, an increase of the jump temperature in the model is necessary to reproduce the opacity of the HDO lines. However, we cannot conclude that the sublimation temperature is significantly higher than 100 K in this source (W51e). Although some works suggested a higher evaporation temperature of 110 – 120 K (Fraser et al. 2001), the HDO transition cannot be perfectly reproduced with this temperature. Rather than the sublimation temperature, the assumed size of the hot core might be wrong. Our analyses of the HDO lines in W51e suggest that the size of the hot core in which the abundance of HDO increases due to the evaporation of the icy mantles is smaller than that of the original Rolffs and van der Tak models. Because the source models were constrained by single dish observations with large angular resolution (7.5$''$ and 18.6$''$) and the density profiles are assumed to follow a power law, the derived physical profiles are relatively uncertain in the inner parts of source envelope ($\leq$ 2$''$), where the excited HDO lines originate from. In the case of W51e, the size of the hot core in which the abundance of HDO rises due to the evaporation of the icy mantles should be smaller than that in the models (θ =1.0$''$ instead of 1.4$''$ for Rolffs model and θ =0.7$''$ instead of 2.0$''$ for van der Tak model, Table 5.7) and this circumstance has been also found and reported in Coutens et al. (2014).
Modifications of the jump temperature where also found to be necessary for modeling the HDO lines detected towards G351.58-0.36, G327.3-0.6, and G10.47+0.03, but the opposite direction. For these sources, we need to lower the sublimation temperature to achieve a better agreement between the models and the observations. This implies that the sizes of the hot cores are larger than those assumed in the models (T $>$ 100 K). To further support this argument, we can simply compare the source sizes of the HDO lines at 225 and 241 GHz (observed with the interferometer telescopes, such as the SMA), which mainly originate from hot core, with those of the hot core predicted by models. In the case of G10.47+0.03, the deconvolved size of the HDO lines at 225 and 241 GHz is $\sim$ 1.5$''$ $\times$ 1.0$''$ (Table 5.5). This size is larger than that of the hot core in the two source models (0.8$''$ in Rolffs model and van der Tak model).
Table 5.8 shows the fractional abundances of the best-fit results with modified sublimation temperatures. Although the obtained HDO fractional abundances are different with different sublimation temperature, it is found that the variation of the final HDO/$H_2^{18}O$ ratio is small. We will discuss this result in Section 6.5.1.1 & 6.5.1.2.

5.5 Discussion

5.5.1 Water deuterium fractionation in high-mass sources

Although many $H_2^{16}O$ transitions have been detected with Herschel towards these high-mass star forming regions, this molecule's abundance cannot be well determined from the observed transitions because of

Table 5.8. HDO and $H_2^{18}O$ abundances (other sources).

Models	Tj	θ^d	Best fit HDO abundances		$\chi^2_{\rm red}$	Best fit $H_2^{18}O$ abundances		$\chi^2_{\rm red}(H_2^{18}O)$		$(HDO/H_2O)^e_{in}$	
	K	$''$	inner region	outer region	(HDO)	inner region	outer region	inner region	outer region	inner region	outer region
IRAS 16065-5158											
R model[c]	100	1.1	2×10^{-08}	1.0×10^{-12}	1.1	3×10^{-07}	...	0.4	...	1.0×10^{-04}	...
G351.58-0.35											
W model[a]	100	0.6	9×10^{-08}	7.0×10^{-11}	2.0	...[f]	2.5×10^{-11}	...	2.8	...	1.4×10^{-03}
W model[a]	90	0.9	2×10^{-08}	5.0×10^{-11}	2.0	2.0×10^{-07}	2.5×10^{-11}	0.1	2.7	1.5×10^{-04}	1.0×10^{-03}
W model[a]	80	1.2	1×10^{-08}	3.0×10^{-11}	2.0	7.0×10^{-08}	2.5×10^{-11}	0.1	2.8	2.0×10^{-04}	8.0×10^{-04}
W model[a]	70	1.7	4×10^{-09}	9.0×10^{-12}	2.3	3.5×10^{-08}	2.5×10^{-11}	0.2	2.2	1.7×10^{-04}	6.0×10^{-04}
G327.3-0.6											
V model[b]	100	0.4	...[f]	...	...	...[f]	6.0×10^{-11}	...	2.2	...	...
V model[b]	90	1.0	8×10^{-07}	7.0×10^{-11}	5.7	7.0×10^{-07}	5.8×10^{-11}	0.4	0.7	1.7×10^{-03}	6.0×10^{-04}
V model[b]	80	1.2	6×10^{-07}	7.0×10^{-11}	5.7	6.0×10^{-07}	5.5×10^{-11}	0.4	1.0	1.5×10^{-03}	6.4×10^{-04}
V model[b]	70	1.6	2×10^{-07}	6.5×10^{-11}	6.4	2.0×10^{-07}	5.5×10^{-11}	0.6	1.1	1.5×10^{-03}	5.9×10^{-04}
G10.47+0.03											
R model[c]	100	0.8	...[f]	...[f]	...[f]	...[f]	5.0×10^{-11}	...[f]	2.1	...	...
R model[c]	90	1.0	4×10^{-07}	3.0×10^{-11}	2.7	...[f]	5.5×10^{-11}	...	2.4	...	2.7×10^{-04}
R model[c]	80	1.1	4×10^{-07}	3.0×10^{-11}	2.7	...[f]	5.0×10^{-11}	...	2.2.	...	3.0×10^{-04}
R model[c]	70	1.6	2×10^{-07}	1.5×10^{-11}	2.6	3.0×10^{-07}	4.0×10^{-11}	0.1	2.1	1.0×10^{-03}	1.4×10^{-04}
R model[c]	60	2.1	9×10^{-08}	2.0×10^{-11}	2.4	1.5×10^{-07}	4.3×10^{-11}	0.2	2.1	9.0×10^{-04}	2.5×10^{-04}
V model[b]	100	0.8	...[f]	...	...	...[f]	1.5×10^{-10}	...	2.0	...	...
V model[b]	90	1.0	9×10^{-07}	8.0×10^{-11}	4.0	...[f]	1.3×10^{-10}	...	1.9	...	3.1×10^{-04}
V model[b]	80	1.3	5×10^{-07}	7.0×10^{-11}	2.8	7.5×10^{-07}	1.0×10^{-10}	0.1	2.5	1.0×10^{-03}	3.5×10^{-04}
V model[b]	70	1.7	2×10^{-07}	3.0×10^{-11}	3.1	3.0×10^{-07}	1.0×10^{-10}	0.2	2.0	1.0×10^{-03}	1.8×10^{-04}
V model[b]	60	2.2	1×10^{-07}	2.0×10^{-11}	3.2	2.5×10^{-07}	1.0×10^{-10}	0.1	1.7	6.0×10^{-04}	1.1×10^{-04}

[a] Wyrowski et al. (2016)

[b] van der Tak et al. (2013) [c] Rolffs et al. (2011)

[d] Size of the region where the temperature is higher than Tj.

[e] Assuming $H_2^{16}O/H_2^{18}O = 500$.

[f] Fit is not good enough to determine the HDO abundances (extremely optically thick in high-excitation lines).

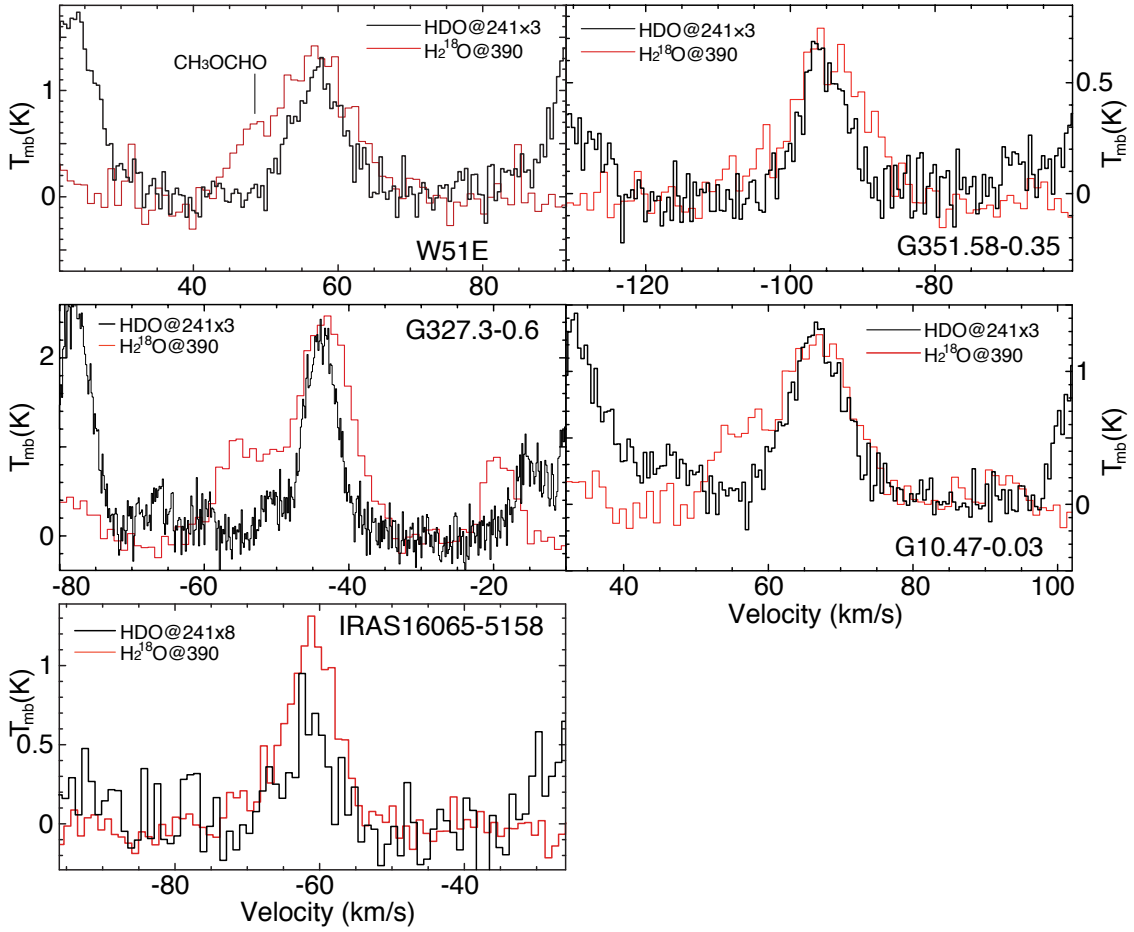

Figure 5.10 Comparison of the observed HDO spectra at 241 GHz (black) with the observed $H_2^{18}O$ 4_{14}–3_{21} spectra at 390 GHz (red). The $H_2^{18}O$ data are taken from Wyrowski et al. in prep.

their large opacities (Coutens et al. 2014). In addition, the H_2O lines usually probe more complex structures than HDO lines do (van der Tak et al. 2013; Kristensen et al. 2010b). $H_2^{18}O$ transitions are therefore widely used to trace H_2O in studies of water deuterium fractionation (Liu et al. 2013; Emprechtinger et al. 2013; Coutens et al. 2014).

In this section, we calculate the HDO/H_2O in the inner and outer regions of the core by comparing the estimated $H_2^{18}O$ abundance with our derived HDO abundance. The high-excitation transition ($H_2^{18}O$ 4_{14}–3_{21}) is suitable to probe the hot core and constrain the $H_2^{18}O$ abundance in the warm inner region. On the other hand, the absorption in the fundamental line ($H_2^{18}O$ 1_{11}–0_{00}) allows us to measure the $H_2^{18}O$ abundance in the cold outer envelope.

5.5.1.1 The HDO/H_2O in the inner/warmer region of the cores

Figure 5.10 shows comparisons of the observed HDO 2_{11}–2_{12} spectra at 241 GHz (black lines) with the observed $H_2^{18}O$ 4_{14}–3_{21} spectra at 390 GHz (red lines). It is obvious that the detected $H_2^{18}O$ emis-

Table 5.9. Properties of the analyzed $H_2^{18}O$ ($4_{1,4}$–$3_{2,1}$) line at 390 GHz and the derived D/H ratios of water in the inner/hot region of the cores.

Source	dv[a] (km/s)	$T_{\rm peak}^{ce}$ (K)	$V_{\rm LSR}^{e}$ (km/s)	Δv^{de} (km/s)	$\int T_{\rm mb}$dv^{e} (K km/s)	$H_2^{18}O$ column density[b] (cm^{-2})	(HDO/H2O)$_{in}^{f}$
W51e	0.94	1.32	56.0	8.0	11.3	6.8×10^{15}	4.8×10^{-04}
IRAS 16065-5158	0.94	1.04	-61.5	7.9	8.8	1.1×10^{16}	4.5×10^{-04}
G351.58-0.35	0.94	0.68	-95.5	7.0	5.1	1.8×10^{15}	8.0×10^{-04}
G327.3-0.6	0.94	0.93	-45.0	6.4	6.3	6.1×10^{16}	5.9×10^{-03}
G10.47+0.03	0.94	0.90	66.0	10.2	9.8	2.7×10^{17}	2.6×10^{-03}

[a] Resolution
[b] Ortho-$H_2^{18}O$ column density
[c] $T_{\rm mb}$ scale
[d] Measured line widths
[e] Value is derived from gaussian fit using the software CLASS.
[f] Assumption: $^{18}O/^{16}O$=500 and an ortho to para ratio of 3/1

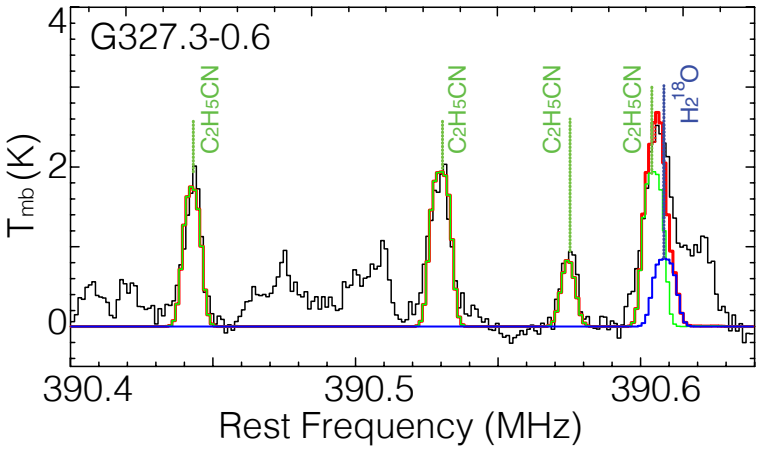

Figure 5.11 The molecular spectrum at 390 GHz in G327.3-0.6. The modeled C_2H_5CN and $H_2^{18}O$ are shown in green and blue, respectively. The composed spectrum is shown in red.

sion spectra are wider than the HDO lines, in particular when we remove the influence of the blending CH_3OCHO line. The additional red-shifted emission might correspond to blending C_2H_5CN lines. Because many C_2H_5CN lines are detected in the $H_2^{18}O$ spectra, we can decompose the emission line by modeling the C_2H_5CN and $H_2^{18}O$ transition lines. Figure 5.11 shows as example the analysis of $H_2^{18}O$ in G327.3-0.6. We reproduced the C_2H_5CN lines (green) and the $H_2^{18}O$ line (blue) to match the composed spectrum (red) to the observed spectrum (black). Table 5.9 lists the properties of the modeled $H_2^{18}O$ 4_{14}–3_{21} lines. The obtained physical parameters (system velocity and line width) of the $H_2^{18}O$ lines are similar to those of the HDO line at 241 GHz (Table 5.3), suggesting that they mainly come from the same gas. We therefore can calculate the HDO/H_2O values in the inner/warmer region of the cores by estimating the $H_2^{18}O$ abundance with this $H_2^{18}O$ transition. There are two methods to derive $H_2^{18}O$'s fractional abundance.

First, assuming that the $H_2^{18}O$ line at 390 GHz is optically thin and in LTE, the $H_2^{18}O$ column density (N_{tot}) can be derived from the following equation,

$$\frac{N_{tot}}{N'_u} = \frac{Q_{rot}}{g_u} exp(\frac{E_u}{kT_{ex}}),$$

where Q_{rot} is the rotational partition function, E_u is the Eu is the upper level energy of the transition, T_{ex} is the excitation temperture and N'_u is the molecular density in the upper energy level u, which has been corrected for the beam filling factor, f.

Here, we used T_{rot} listed in Table 5.4 for T_{ex} and the inverse of the beam filling factor was calculated by

$$1/f = (B/S) + 1,$$

where B is the beam size and S is the source size listed in Table 5.4. Thus, with the HDO column density listed in Table 5.4 and the two assumptions that $^{18}O/^{16}O$=500, and that the ortho-to-para ratio is 3:1, the D/H ratios of hot water in different sources are obtained (Table 5.9).

Second, we modeled the $H_2^{18}O$ lines at 390 GHz with similar procedures as in section 5.4 and the resulting fractional abundances of ortho-$H_2^{18}O$ are listed in Tables 5.7 and 5.8. The resulting HDO/H_2O ratios for each source are again estimated with the assumptions that the standard ortho/para ratio is 3 and the $^{18}O/^{16}O$ ratio is 500. Similar to the analyses of the HDO transition lines, the $H_2^{18}O$ fractional abundances are obtained using a range of different T_j. As a result, the variation of the final HDO/H_2O ratio is smaller than a factor of 4 (Table 5.7 and 5.8). Therefore, the parameter T_j is of minor importance for the calculation of the D/H ratio. This characteristic has been pointed out already in Coutens et al. (2014).

Although the derived water deuterium fractionation in the inner/warmer region of the cores with the two methods are different, the variances of the D/H ratios of water are less than a factor of 6 (Table 5.11). This difference may be caused by the uncertainties in the source sizes or the improper assumption that the $H_2^{18}O$ line at 390 GHz is optically thin. It is found that the $H_2^{18}O$ line at 390 GHz is sometimes even optically thick in some sources with certain sublimation temperatures during the RATRAN modeling (see Table 5.8).

The D/H ratio of water has been studied towards W51e and G10.47+0.03 in the past. Reported values are 3×10^{-4} and 6.3×10^{-5} with an uncertainty of a factor of 4 in W51e and 2.6×10^{-4} with an uncertainty of a factor of 4 in G10.47 (Jacq et al. 1990; Gensheimer et al. 1996). The calculated values in this work are consistent with these previous estimation ((0.5–1.2)$\times10^{-3}$ in W51e and (0.6-2.6)$\times10^{-3}$ in G10.47+0.03, Table 5.9, 5.8 and 5.7).

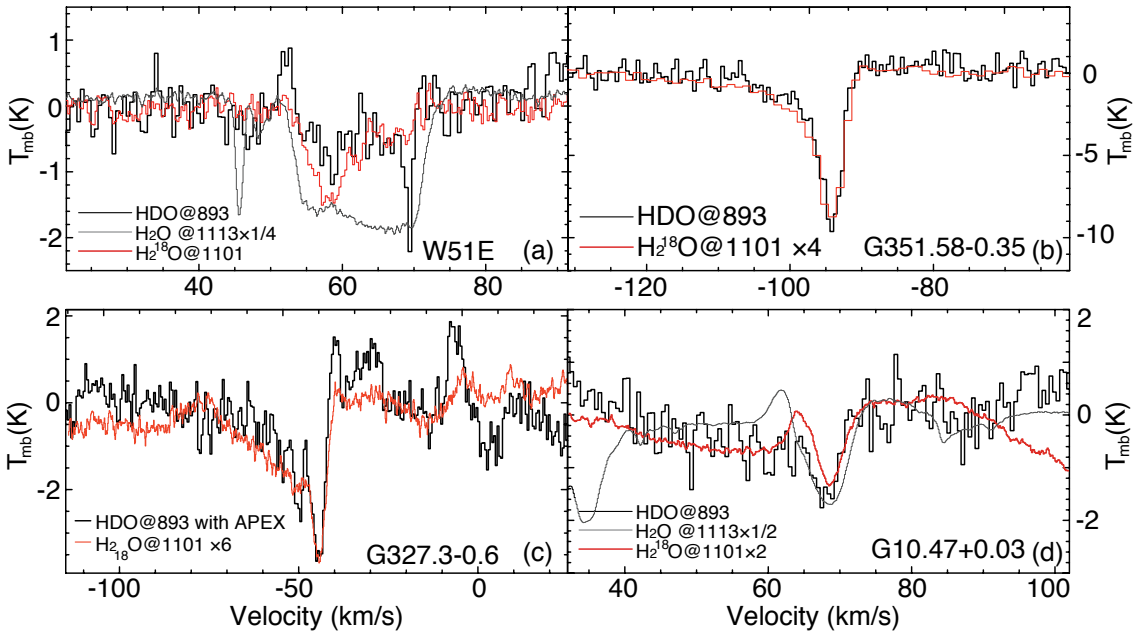

Figure 5.12 Comparison of the observed HDO spectra at 893 GHz (black) with the observed $H_2^{18}O$ 1_{11}–0_{00} spectra at 1101 GHz (red) and H_2O 1_{11}–0_{00} spectra at 1113 GHz (grey). The $H_2^{18}O$ and H_2O data are taken from Wyrowski et al. (2010), van der Tak et al. (2013) and Herschel Archive data.

5.5.1.2 The HDO/H_2O ratio in the outer/colder region of the cores

Figure 5.12 displays the spectra of the 1_{11}–0_{00} ground-state transitions of HDO and $H_2^{18}O$. Except for the HDO absorption line at 69.4 km/s (Figure 5.12a) which is suggested to be associated with a dense clump in a filament interacting with W51e2 (Mookerjea et al. 2014), the HDO and $H_2^{18}O$ have very similar line profiles. In addition, the blue-shifted wing-like absorption is detected in the HDO and $H_2^{18}O$ spectra towards G351.58-0.35, G327.3-0.6 and G10.47+0.03. This similarity between the two spectra implies that the molecular lines may come from the same gas. Therefore, we are able to calculate the D/H ratios of water in the outer/colder region of the cores with the $H_2^{18}O$ abundance which is estimated here. The $H_2^{18}O$ abundance in the outer/colder region is obtained also with the two methods described below.
With the two assumptions that only the ground state of the molecule is populated and that the excitation temperature of the line is negligible with respect to the temperature of the background continuum source, the total column density of the absorbing HDO and $H_2^{18}O$ can then be computed from (Comito et al. 2003; Tarchi et al. 2004):

$$N_{tot} = \frac{8\pi\nu^3}{A_{ul}c^3}\frac{g_l}{g_u}\tau\Delta v,$$

where Δv is the line width, A_{ul} is the Einstein A Coefficient, and g_l and g_u are the statistical weights of the lower and upper level. The optical depth of the absorbed line can be determined by

$$\tau = -ln(1-\frac{T_L}{T_C}),$$

where T_L is the brightness temperature of the line and T_C is the brightness temperature of the continuum. The $H_2^{18}O$ line parameters from the Gaussian fit and the calculated total column densities of the

Table 5.10. $H_2^{18}O$ line parameters, the column densities of HDO and $H_2^{18}O$ and the derived D/H ratios in the outer/cold region of the cores. The parameter errors are obtained from the Gaussian fit.

Source	$T_{\rm peak}^{b}$ [c] K	$T_{\rm cont}^{bcd}(1101)$ K	Δv^{b} km/s	$V_{\rm LSR}^{b}$ km/s	$N(H_2^{18}O)$ cm^{-2}	$T_{\rm cont}^{cdf}(893)$ K	N(HDO) cm^{-2}	HDO/H_2O[e]	$T_{\rm cont}^{bdg}(1101)$ K	HDO/H_2O[eh]
W51e	-1.40 ± 0.14	7.9	6.2±0.4	58.3±0.2	2.83×10^{12}	11.3	1.10×10^{12}	1.94×10^{-4}	2.5	4.64×10^{-5}
G351.58-0.35	-0.61 ± 0.06[i]	4.8	10.2±1.1	-99.4±1.1	3.22×10^{12}	11.3	4.43×10^{12}	6.88×10^{-4}	2.2	3.07×10^{-4}
	-1.97 ± 0.06[j]	4.8	3.6±1.1	-94.2±1.1	4.47×10^{12}	11.3	1.19×10^{13}	1.33×10^{-3}	2.2	3.19×10^{-4}
G327.3-0.6	-0.28 ± 0.05[i]	4.2	19.3±0.6	-54.7±0.3	3.20×10^{12}	12.5	4.22×10^{12}	6.58×10^{-4}	2.8	4.31×10^{-4}
	-0.47 ± 0.05[j]	4.2	4.1±0.2	-44.6±0.1	1.15×10^{12}	12.5	2.57×10^{12}	1.11×10^{-3}	2.8	7.17×10^{-4}
G10.47-0.03	-0.36 ± 0.03[i]	4.2	18.8±1.3	52.9±0.6	4.02×10^{12}	11.9	2.64×10^{12}	3.28×10^{-4}	2.7	2.03×10^{-4}
	-0.63 ± 0.03[j]	4.2	3.3±0.3	68.8±0.1	1.30×10^{12}	11.9	1.13×10^{12}	4.37×10^{-4}	2.7	2.65×10^{-4}

[b] $H_2^{18}O$ line parameters

[c] $T_{\rm mb}$ scale

[d] continuum temperature

[e] Assumption: $^{18}O/^{16}O$=500 and an ortho to para ratio of 3/1

[f] Continuum level at 893 GHz observed with APEX

[g] The derived continuum flux at 1101 GHz of the core seen with APEX in the Herschel beam

[h] The updated total column $H_2^{18}O$ density with recalculated $T_{\rm cont}$ at 1101 GHz

[i] The wide-blue-shifted absorption

[j] The narrow absorption at the system velocity

HDO/H_2O ratios are listed in Table 5.10. Under the assumption that the standard ortho/para ratio is 3 and the $^{18}O/^{16}O$ ratio is 500, we also estimate the D/H ratios of water in the outer/colder region of the cores. However, because the emitting area of the continuum at 1101 GHz might be larger than the source size of the $H_2^{18}O$ gas, the abundances of para-$H_2^{18}O$ might be underestimated here. Thus, assuming that the dust emissivity spectral index β is 2 (Draine & Lee 1984; Schnee et al. 2010), we derived the continuum flux at 1101 GHz of the cores seen with APEX in the Herschel beam and then recalculated the D/H ratios of water (last two column in Table 5.10). The obtained ratios are then lower-limits.
Another way to simply estimate the $H_2^{18}O$ abundance in the outer region is analyzing the absorption of the $H_2^{18}O$ ground-state transition lines at 1101 GHz with RATRAN. The modeling was performed with similar procedures as in section 5.4. The obtained para-$H_2^{18}O$ fractional abundances and the calculated HDO/H_2O ratios in the outer region of the cores are listed in Tables 5.7 and 5.8. Because the modeling here only focused on the absorption parts of the $H_2^{18}O$ lines which originate from outer region, the modification of the sublimation temperature does not have a significant influence on the results.
The variation of the values of the water deuterium fractionation in the outer/colder region of the cores, which are derived with the two different ways, are smaller than a factor of 5 (Table 5.11). This difference may be caused by uncertainties in the assumptions, for example, the environment may not being in LTE.

5.5.1.3 The HDO fractional abundance and water deuterium fractionation in high-mass star-forming regions

A comparison of the HDO fractional abundances between different sources is shown in Tables 5.4, 5.7, 5.8, and 5.10. The abundance of HDO jumps by more than three orders of magnitude in all high-mass star-forming regions. Similarly to this work, jump models have been widely used to analyze the HDO and H_2O spectra of other high- and low-mass sources (Liu et al. 2013; Coutens et al. 2014; Liu et al. 2011; Parise et al. 2005a; Coutens et al. 2012). Therefore, ices are obviously shown to evaporate from the grains in the inner parts of the envelopes in protostars of different masses.
We first searched for a correlation of the HDO abundances and D/H ratios of water obtained in this work with different source parameters, such as the bolometric luminosity L_{bol}, the envelope mass M, and the ratio L_{bol}/M. The L_{bol}/M ratio is considered to be an indicator of the evolutionary state of a young stellar object both for low-mass (Saraceno et al. 1996; Bontemps et al. 1996) and high-mass (Molinari et al. 2008; Giannetti et al. 2013) star formation. Figure 5.13 shows the HDO abundances (Figure 5.13a – 5.13f) and HDO/H_2O ratios (Figure 5.13g – 5.13l) as a function of these parameters. We do not find correlations between most of them. The only exception is that the HDO abundances and HDO/H_2O ratios measured toward the blue-wing show very similar values in our source sample (Figure 5.13d – 5.13f and Figure 5.13j – 5.13l). This correlation could be simply fortuitous or it might suggest that the mechanism of the water formation in these blue-wings (outflows) could be the same for different sources. To verify this, more similar studies toward other high-mass sources are needed.
A comparison of HDO/H_2O ratios between different sources is shown in Table 5.11. Generally speaking, the estimated ratios determined in this work are around a few 10^{-4} to 10^{-3}, except for the ratios in the outer core of W51e (the HDO absorption is detected under 3σ). These values are similar to those measured in G34.26+0.15, AFGL 2591 and other high-mass sources, such as Ori-IRc2, G31.41+0.31, and G10.47+0.03A (Jacq et al. 1990; Gensheimer et al. 1996; van der Tak et al. 2006; Bergin et al. 2010; Coutens et al. 2014), and lower than those in low-mass protostars. These relatively low D/H ratios have

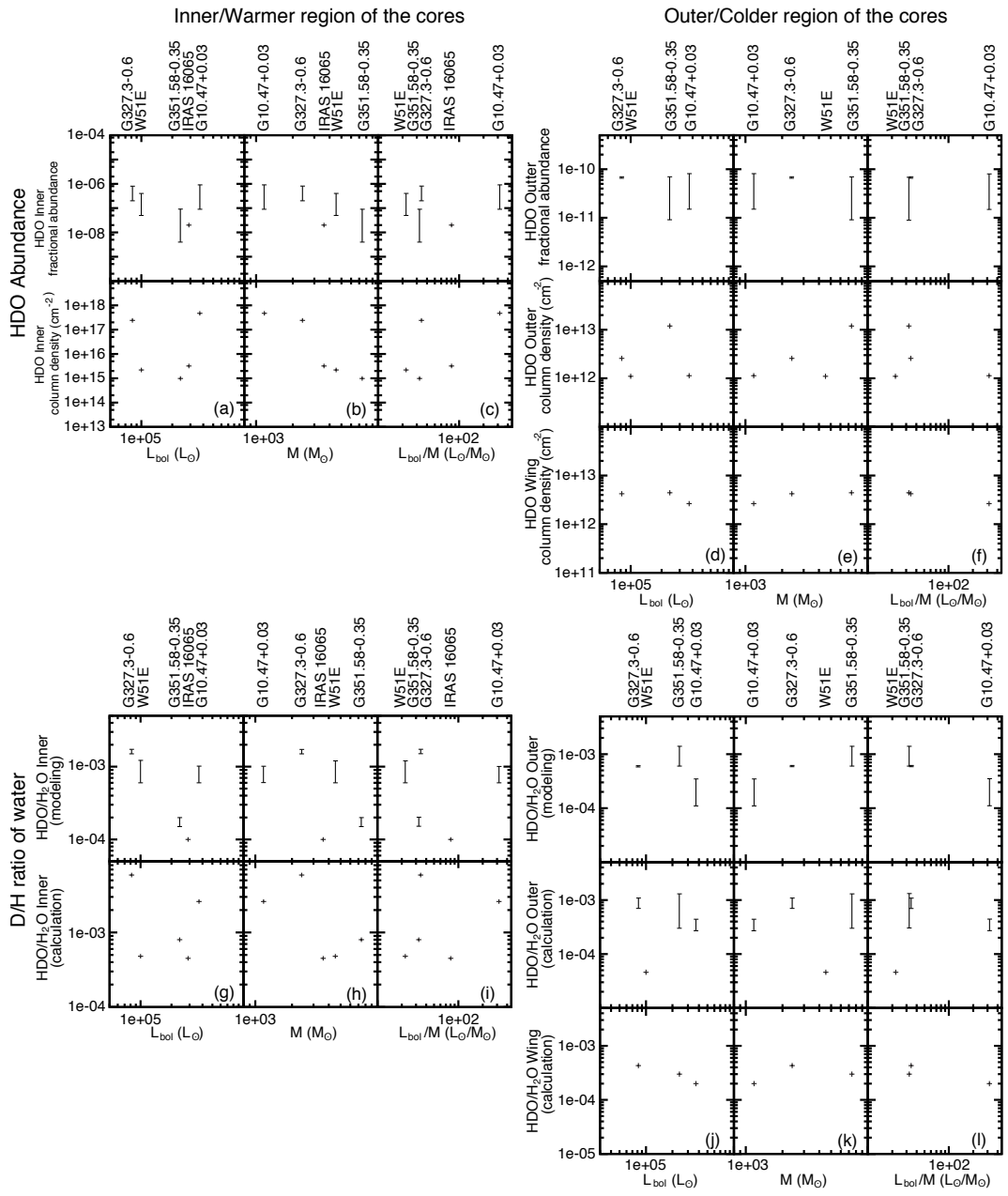

Figure 5.13 Comparison of the inner (left) and outer (right) HDO abundances (upper panels) and HDO/H_2O ratios (lower panels) estimated in the high-mass star-forming regions as a function of the ratio between the bolometric luminosity L_{bol}, the envelope mass M, and the ratio L_{bol}/M. Upper left: HDO abundances shown in upper and lower parts are the fractional abundance obtained from the results of the RATRAN modeling and from the rotation diagrams, respectively. Upper right: Similar to upper left panels and the lowest panels here are the HDO abundance in blue-wing obtained from the calculation in Section 6.5.1.2. Lower left: The ratios shown in upper and lower panels are calculated from the HDO and $H_2^{18}O$ fractional abundance obtained from the results of the RATRAN modeling and from the rotation diagrams, respectively. Lower right: Similar to lower left panels and the lowest panels here are the results estimated from the HDO and $H_2^{18}O$ fractional abundance in blue-wing obtained from the calculation in Section 5.5.1.2.

Table 5.11. HDO fractional abundance in different high-mass star forming regions.

Source	HDO/H_2O				
	inner core		outer core		blue-wing
	Modeling[e]	Calculation[f]	Modeling[e]	Calculation[g]	Calculation[g]
	This study				
W51e	$(0.6-1.2)\times10^{-3}$	4.8×10^{-4}		4.6×10^{-5}	...
IRAS 16065-5158	1.0×10^{-4}	4.5×10^{-4}	...	...	...
G351.58-0.35	$(1.5-2.0)\times10^{-4}$	8.0×10^{-4}	$(0.6-1.4)\times10^{-3}$	$(0.3-1.3)\times10^{-3}$	3.0×10^{-4}
G327.3-0.6	$(1.5-1.7)\times10^{-3}$	5.9×10^{-3}	$(5.9-6.0)\times10^{-4}$	$(0.7-1.1)\times10^{-3}$	4.3×10^{-4}
G10.47-0.03	$(0.6-1.0)\times10^{-3}$	2.6×10^{-3}	$(1.1-3.5)\times10^{-4}$	$(2.7-4.4)\times10^{-4}$	2.0×10^{-4}
	Previous studies				
G34.26+0.15	3×10^{-4a}		$(1.9-4.9)\times10^{-4a}$		...
	$(3.5-7.5)\times10^{-4b}$		$(1.0-2.2)\times10^{-3b}$		...
AFGL 2591	5×10^{-4c}		$(0.4-4.0)\times10^{-3c}$		...
W33A	7×10^{-3d}				

[a]Liu et al. (2013);[b]Coutens et al. (2014);

[c]van der Tak et al. (2006);[d]Bergin et al. (2010)

[e]The HDO/H_2O ratios listed in Table 5.7 and Table 5.8.

[f]The HDO/H_2O ratios listed in Table 5.9. [g]The HDO/H_2O ratios listed in Table 5.10

been explained by the argument that the dense and cold pre-collapse phase is short in high-mass star-forming regions and that the destroyers of the H_3^+ isotopologuese, CO and O freeze out on the grains (van der Tak et al. 2006; Liu et al. 2013; Taquet et al. 2014).

The HDO/H_2O ratios in the blue-wings, which might originate from the outflows, are estimated in the high-mass star forming regions for the first time. As we mentioned above, the values obtained in this work are similar to each other. These values are slightly lower than the D/H ratio in a molecular outflow shock of low-mass protostars, ((0.4–2)$\times10^{-3}$ for L1157-B1 found by Codella et al. (2012) and (0.07–0.6)$\times10^{-2}$ for NGC1333 IRAS 4A found by Coutens et al. (2013a)). Moreover, the D/H ratios of water in blue-wings are not far away from the ratios in the outer region of their original cores (within a factor of 2).

Comparing the HDO/H_2O ratios in the inner and outer region of the cores, it is found that the ratios in the inner regions are larger than the ratios in the outer region in the sources G327.3-0.6, G10.47+0.03, and W51e. On the contrary, the ratios are larger in the outer region of the cores in G351.58-0.35, G34.26+0.15, and AFGL 2591. This difference is probably due to the different evolutionary stages of the cores in different star-forming regions. In the inner region of the core, water and deuterated water are mainly destroyed by chemical reactions: H + H_2O/HDO $\rightarrow$ OH + ortho-H_2/para-H_2. However, the reverse reactions only efficiently form water and thus the HDO/H_2O ratio generally decreases as a function of time (Coutens et al. 2014). On the other hand, in the outer region of the core, the ion-molecules react with water and deuterated water. For example, HCO^+ + HDO $\rightarrow$ H_2DO^+ + CO. The product H_2DO^+ will dissociatively recombine with an electron to form HDO again. Water is also reformed through similar processes but not as efficient as deuterated water (Taquet et al. 2014; Coutens et al. 2014). In addition, in cold regions, the D atoms are enriched in the ice with time due to photodesorption which causes the HDO/H_2O ratio to increase both in ice and gas when the molecules are photodesorbed (Arasa et al. 2015).

The D/H ratio of water can also reflect the different initial conditions, such as density and temperature, during ice formation (Caselli & Ceccarelli 2012; Coutens et al. 2014). To confirm and clarify these arguments and understand which mechanism play a leading role in different environments, detailed analysis of the astrochemical models for a variety of sources is required.

5.6 Conclusion

Deuterated water was detected in five luminous high-mass sources with ground-based telescopes (APEX and SMA). The HDO ground-state transition, which was observed toward G351.58-0.35, G327.3-0.6, and G10.47+0.03, show blue-wing absorption, which may trace the outflows in these star forming regions. In addition to a rotation diagram, we also used the 1D radiative transfer code RATRAN to analyze the spectra to obtain HDO fractional abundances throughout the envelopes from the inner/warmer regions to the outer/colder regions. To better reproduce the line profiles, it is found that modifications to the sublimation temperature of deuterated water are necessary, implying that the hot cores are larger or smaller than expected by physical source models, which were constrained by single dish observations with large angular resolution ($\sim 7.5''$ and $\sim 18.6''$) and thus are relatively uncertain in the inner parts of the source envelope ($\lesssim 2.0''$).

The HDO/H_2O ratios are estimated by comparing our results with the analyses of the two $H_2^{18}O$ transition lines, 4_{14}–3_{21} and 1_{11}–0_{00}. The HDO/H_2O ratios in all sources ($\sim 10^{-3}-\sim 10^{-4}$) are similar to those

in other high-mass sources and are obviously lower than in low-mass star-forming regions, supporting the previous argument made for G34.26+0.15 that the dense and cold pre-collapse phases are short.
It is found that the D/H ratios in the inner regions are larger than the ratios in the outer regions in the sources G327.3-0.6, G10.47-0.03, and W51e. By contrast, the ratios are larger in the outer region of the cores in G351.58-0.35, G34.26+0.15 and AFGL 2591 (van der Tak et al. 2006; Coutens et al. 2014). This difference probably can be explained by the different evolutionary stages of the cores or the different initial conditions in different star-forming regions. More detailed analyses of the astrochemical models for each source are required to clarify these arguments.

Chapter 6

Discussion and summary

In the previous chapters, we have shown and discussed the results of our studies toward low- and high-mass star-forming regions. Here, we present an overall discussion of the results and final summaries.

6.1 Discussion

6.1.1 The distribution of HDO in star-forming regions

The distribution of water deuterium fractionation ratios in low- and high-mass star-forming regions studied in this thesis is summarized in Table 6.1. The HDO/H_2O fractional abundance varies by at least two orders of magnitude between the inner and the outer regions of envelopes, except for AFGL2591 and W33A, where the outer abundance was only constrained with the HDO $1_{0,1}$–$0_{0,0}$ line (464 GHz) (van der Tak et al. 2006). This line is not very suitable to study the HDO abundance in the outer region alone because the HDO emission in the inner/warmer region also contributes significantly to the spectra (Liu et al. 2013; Coutens et al. 2014). Therefore, the differences show that jump models are necessary for all star-forming regions. This implies that ices evaporate from the grains in the inner part of the envelope in different-masses star-forming regions (Parise et al. 2005a; Liu et al. 2011; Coutens et al. 2012; Liu et al. 2013; Coutens et al. 2014).

Previous studies show that the HDO fractional abundance in inner and outer regions do not correlate with the evolutionary state of star formation (see Section 5.5.1.3 and Section 4.2 in Coutens et al. (2013a)), but the fractional abundance may be related to the physical environment (e.g. temperature and density), determined by the initial conditions of ambient molecular clouds (Coutens et al. 2013a). This interpretation is based only on the comparison of the samples in the NGC 1333 complex, so more studies toward different star-forming complexes are needed to confirm it.

Table 6.1. Comparison of HDO fractional abundance between different sources.

Source	X^{HDO}(best fit)		$\frac{HDO}{H_2O}$			
	Inner	outer	Inner	outer	innermost	outflow
	High-mass hot cores					
G34.26+0.15	6.0×10^{-8ab}	5.0×10^{-12ab}	3×10^{-4ab}	$(1.9 - 4.9) \times 10^{-4ab}$	...	...
	2.0×10^{-7c}	8.0×10^{-11c}	$(3.5 - 7.5) \times 10^{-4c}$	$(1.0 - 2.2) \times 10^{-3c}$	...	...
W51e	1.0×10^{-7a}	1.0×10^{-14d}	$(0.6 - 1.2) \times 10^{-3a}$	...	...	...
IRAS 16065-5158	2.0×10^{-8a}	1.0×10^{-12d}	1×10^{-4a}	...	...	...
G351.58-0.35	2.0×10^{-8a}	5.0×10^{-11a}	$(1.5 - 2.0) \times 10^{-4a}$	$(0.6 - 1.4) \times 10^{-3a}$	...	3.0×10^{-4}
G327.3-0.6	8.0×10^{-7a}	7.0×11^{-11a}	$(1.5 - 1.7) \times 10^{-3a}$	$(5.9 - 6.0) \times 10^{-4a}$	...	4.3×10^{-4}
G10.47-0.03	9.0×10^{-8a}	2.0×10^{-11a}	$(0.6 - 1.0) \times 10^{-3a}$	$(1.1 - 3.5) \times 10^{-4a}$	...	2.0×10^{-4}
AFGL 2591	1.0×10^{-7e}	4.0×10^{-09e}	5×10^{-4e}	$(0.4 - 4.0) \times 10^{-3e}$	...	...
W33A	2.0×10^{-7e}	1.0×10^{-08e}	7×10^{-3l}		...	...
NGC 6334I	...	...	2.6×10^{-4m}		...	2.1×10^{-4m}
	Low-mass protostars					
NGC1333 IRAS2A	8.0×10^{-8af}	7.0×10^{-10af}	$\geq 1 \times 10^{-2af}$	$7^{+11}_{-6} \times 10^{-2af}$	7.4×10^{-4j}	...
	...	...	1×10^{-3n}	...	...	...
NGC1333 IRAS4A	7.5×10^{-9g}	1.2×10^{-11g}	$(0.4 - 3) \times 10^{-3g}$	...	1.9×10^{-3j}	$(0.7 - 90) \times 10^{-3g}$
NGC1333 IRAS4B	1.0×10^{-8g}	1.2×10^{-10g}	$(0.1 - 3.7) \times 10^{-3g}$	...	5.9×10^{-4j}	...
IRAS 16293-2422	1.0×10^{-7h}	1.5×10^{-10h}	3×10^{-2h}	$\leq 2 \times 10^{-3}(3\sigma)^h$	9.2×10^{-4k}	...
	1.8×10^{-7i}	8.0×10^{-11i}	3.4×10^{-2i}	5×10^{-3i}		
L1448-mm	4.0×10^{-7g}	...	...	...	...	...

[a]This thesis.

[b]Liu et al. (2013);[c]Coutens et al. (2014);

[d]The value is not reliable because the absorption is under 3σ detection.

[e]van der Tak et al. (2006);[f]Liu et al. (2011);[g]Coutens et al. (2013a); [h]Parise et al. (2005a);[i]Coutens et al. (2012)

[j]($\lesssim$ 300 AU), Persson et al. (2014); [k]($\lesssim$ 50 AU), Persson et al. (2013);

[l]Bergin et al. (2010);[m]Emprechtinger et al. (2013);[n]Visser et al. (2013)

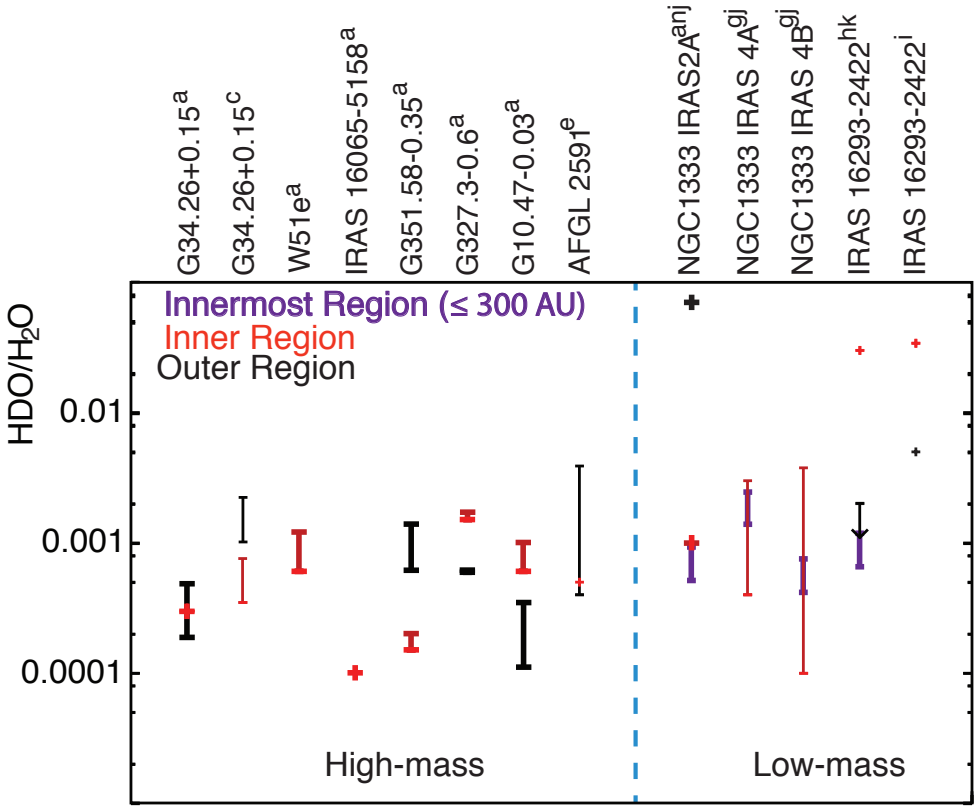

Figure 6.1 Values of the D to H ratio of water, for different objects. Data plotted with bold lines and with the superscript "a" are the studies done in this thesis. For other superscripts, see Table 6.1.

6.1.2 Water deuterium fractionation in star-forming regions

We summarize the D/H ratios of water from our jump model studies in in Table 6.1. In order to easily compare the values, the D/H ratios are plotted in Figure 6.1. The HDO/H_2O ratios are consistently around a few 10^{-4} to a few 10^{-3} in the high-mass star forming regions and similar ratios generally appeared in the innermost regions of low-mass star-forming cores (Persson et al. 2013, 2014), in the solid water from low-mass star-forming regions (Teixeira et al. 1999), and are predicted by chemical models in water ice (Yang et al. 2013; Ceccarelli et al. 2014; Furuya et al. 2016). Previous studies toward the innermost regions in the four low-mass star-forming regions suggest that because the infall timescales are too short for significant gas-phase chemical reactions of water, the relatively low ratios ($\sim$$10^{-4}$ to $\sim$$10^{-3}$) might be independent of the initial conditions of the birth environment and could directly result from the ratios in the original water ice (Persson et al. 2014). The timescales for the early, deeply-embedded stages in the high-mass star-forming regions are also very short and therefore the obtained D/H ratios may also reflect the ratios in the water ice. If the above arguments are correct, the chemical evolution of water proceeds similarly in different mass star-forming regions and the slight differences of the HDO/H_2O ratios between different sources might arise from the variation of initial conditions (e.g. ortho-to-para nuclear spin ratio of H_2, density, and temperature, Coutens et al. 2013a,b; Furuya et al. 2015; Lee & Bergin 2015).
Moreover, it is found that the D/H ratios of water in outflows are very similar to each other in high-mass star-forming regions ($(2.0-4.3)\times10^{-4}$) and these values are not far away from the ratios in the source's original envelopes (within a factor of 2). This consistency is also found in the low-mass star-forming region NGC 1333 IRAS4A and it was suggested that the gaseous water is released by thermal desorption in the warm corino and by sputtering in the outflow and that HDO is therefore widespread in the early evolution of the core (Coutens et al. 2013a). The results of our studies toward several high-mass star-forming regions may also support this implication. To confirm this argument, higher angular resolution observations are needed to investigate the D/H ratios of water in the very centers of the high-mass hot cores.
Current gas-grain astrochemical models tend to over-predict the HDO/H_2O ratio in the inner hot regions and underpredict the D_2O/HDO ratio in the inner hot regions. Two possibilities were proposed: one is that there is a lack in our understanding of deuterium chemistry on icy grain surfaces and another is that after the sublimation of water ice, water formation at high temperature (T $>$ 200–300 K) plays a role in the inner regions (Coutens et al. 2014). The consistency of our results is more in favor of the first possibility. Actually, a new study presents a chemical model, which assumes that the H_2O, HDO, and D_2O are formed via grain surface reactions at different time, that successfully predicts the HDO/H_2O and D_2O/HDO ratios measured in a low-mass star-forming region (Furuya et al. 2016). In order to clarify if this scenario is correct, investigations of the D_2O/HDO ratios toward star-forming regions with different masses are necessary.

6.2 General summary

In this thesis, I present our results of the studies of the HDO/H_2O ratios in one low-mass protostar and six luminous high-mass star-forming regions. Deuterated water was detected in these sources with ground-based telescopes (APEX and SMA). We modeled the HDO spectra with the 1D radiative transfer code

RATRAN to obtain HDO fractional abundances throughout the envelopes from the inner and warmer regions to the outer and colder regions. To reproduce the line profiles, modifications are required for specific physical source properties that have been previously established (e.g., velocity profile for G34.26+0.15 and sublimation temperature of HDO for other high-mass sources). This is because the original source models were constrained by single dish observations with low angular resolution and therefore the inner part of the source envelope was not resolved ($\lesssim 2.0''$).

Our studies show that the HDO abundance is enhanced in the inner regions because of the ice evaporation from the grains. This holds for sources with very different masses. Previous studies toward low-mass protostars and our studies toward the high-mass star-forming regions show that the values of the HDO fractional abundance in both regions do not correlate with the evolutionary states.

Together with the analysis of the $H_2^{18}O$ transition lines observed with the Herschel Space Observatory and APEX, the HDO/H_2O ratios are estimated. It is found that the ratios in the envelopes and the outflows in the high-mass star-forming regions and in the innermost regions in the low-mass star-forming cores are very similar. In addition, similar ratios are also found and predicted by chemical models for solid water. Because the timescales of the early evolution are short for the early stages of the sources of different masses, the observed ratios in gaseous water could directly reflect the original ratios in the water ice. This indicates that the chemical evolution of water is the same regardless of the masses of the regions.

Bibliography

Altwegg, K., Balsiger, H., Bar-Nun, A., et al. 2015, Science, 347

Andersson, M. & Garay, G. 1986, A&A, 167, L1

Andersson, S. & van Dishoeck, E. F. 2008, A&A, 491, 907

Andre, P., Ward-Thompson, D., & Barsony, M. 1993, ApJ, 406, 122

André, P., Ward-Thompson, D., & Barsony, M. 2000, Protostars and Planets IV, 59

Arasa, C., Koning, J., Kroes, G.-J., Walsh, C., & van Dishoeck, E. F. 2015, A&A, 575, A121

Atkinson, R., Baulch, D. L., Cox, R. A., et al. 2004, Atmospheric Chemistry and Physics, 4, 1461

Avalos, M., Lizano, S., Rodríguez, L. F., Franco-Hernández, R., & Moran, J. M. 2006, ApJ, 641, 406

Balsiger, H., Altwegg, K., & Geiss, J. 1995, J. Geophys. Res., 100, 5827

Bate, M. R. 1998, ApJ, 508, L95

Bergin, E. A., Melnick, G. J., Stauffer, J. R., et al. 2000, ApJ, 539, L129

Bergin, E. A., Phillips, T. G., Comito, C., et al. 2010, A&A, 521, L20

Bergin, E. A. & Tafalla, M. 2007, ARA&A, 45, 339

Bergin, E. A. & van Dishoeck, E. F. 2012, Philosophical Transactions of the Royal Society of London A: Mathematical, Physical and Engineering Sciences, 370, 2778

Beuther, H., Churchwell, E. B., McKee, C. F., & Tan, J. C. 2007, Protostars and Planets V, 165

Beuther, H., Schilke, P., Gueth, F., et al. 2002, A&A, 387, 931

Bockelée-Morvan, D., Biver, N., Swinyard, B., et al. 2012, A&A, 544, L15

Bockelée-Morvan, D., Gautier, D., Lis, D. C., et al. 1998, Icarus, 133, 147

Boesgaard, A. M. & Steigman, G. 1985, ARA&A, 23, 319

Bontemps, S., Andre, P., Terebey, S., & Cabrit, S. 1996, A&A, 311, 858

Boogert, A. C. A., Pontoppidan, K. M., Knez, C., et al. 2008, ApJ, 678, 985

Brinch, C., Jørgensen, J. K., & Hogerheijde, M. R. 2009, A&A, 502, 199

Buhr, H., Mendes, M. B., Novotný, O., et al. 2010, Phys. Rev. A, 81, 062702

Campins, H., Hargrove, K., Pinilla-Alonso, N., et al. 2010, Nature, 464, 1320

Carral, P. & Welch, W. J. 1992, ApJ, 385, 244

Caselli, P. & Ceccarelli, C. 2012, A&A Rev., 20, 56

Cazaux, S., Caselli, P., & Spaans, M. 2011, ApJ, 741, L34

Ceccarelli, C., Caselli, P., Bockelée-Morvan, D., et al. 2014, Protostars and Planets VI, 859

Ceccarelli, C., Castets, A., Caux, E., et al. 2000, A&A, 355, 1129

Ceccarelli, C., Castets, A., Loinard, L., Caux, E., & Tielens, A. G. G. M. 1998, A&A, 338, L43

Cernicharo, J. & Crovisier, J. 2005, Space Sci. Rev., 119, 29

Cesaroni, R. 2005, in IAU Symposium, Vol. 227, Massive Star Birth: A Crossroads of Astrophysics, ed. R. Cesaroni, M. Felli, E. Churchwell, & M. Walmsley, 59–69
Charnley, S. B., Tielens, A. G. G. M., & Rodgers, S. D. 1997, ApJ, 482, L203
Charutz, D. M., Last, I., & Baer, M. 1997, The Journal of Chemical Physics, 106, 7654
Chavarría, L., Herpin, F., Jacq, T., et al. 2010, A&A, 521, L37
Chen, H., Grenfell, T. G., Myers, P. C., & Hughes, J. D. 1997, ApJ, 478, 295
Chen, H., Myers, P. C., Ladd, E. F., & Wood, D. O. S. 1995, ApJ, 445, 377
Cheung, A. C., Rank, D. M., & Townes, C. H. 1969, Nature, 221, 917
Chini, R., Kruegel, E., & Wargau, W. 1987, A&A, 181, 378
Churchwell, E. 1999, in NATO Advanced Science Institutes (ASI) Series C, Vol. 540, NATO Advanced Science Institutes (ASI) Series C, ed. C. J. Lada & N. D. Kylafis, 515
Churchwell, E. 2002, ARA&A, 40, 27
Cleeves, L. I., Bergin, E. A., Alexander, C. M. O., et al. 2014, Science, 345, 1590
Codella, C., Ceccarelli, C., Lefloch, B., et al. 2012, ApJ, 757, L9
Comito, C., Schilke, P., Gérin, M., et al. 2003, A&A, 402, 635
Comito, C., Schilke, P., Rolffs, R., et al. 2010, A&A, 521, L38
Condon, J. J. 1997, PASP, 109, 166
Coutens, A., Vastel, C., Cabrit, S., et al. 2013a, A&A, 560, A39
Coutens, A., Vastel, C., Caux, E., et al. 2012, A&A, 539, A132
Coutens, A., Vastel, C., Cazaux, S., et al. 2013b, A&A, 553, A75
Coutens, A., Vastel, C., Hincelin, U., et al. 2014, MNRAS, 445, 1299
Cuppen, H. M., Ioppolo, S., Romanzin, C., & Linnartz, H. 2010, Physical Chemistry Chemical Physics (Incorporating Faraday Transactions), 12, 12077
Dalgarno, A., Black, J. H., & Weisheit, J. C. 1973, Astrophys. Lett., 14, 77
Dalgarno, A. & Lepp, S. 1984, ApJ, 287, L47
Daniel, F., Dubernet, M.-L., & Grosjean, A. 2011, A&A, 536, A76
Daniel, F., Dubernet, M.-L., Meuwly, M., Cernicharo, J., & Pagani, L. 2005, MNRAS, 363, 1083
Dayou, F. & Balança, C. 2006, A&A, 459, 297
de Buizer, J. M. 2004, in IAU Symposium, Vol. 221, Star Formation at High Angular Resolution, ed. M. G. Burton, R. Jayawardhana, & T. L. Bourke, 181
de Laeter, J. R., Böhlke, J. K., & De Biévre, P. 2003, Pure and Applied Chemistry, 75, 683
Dedes, C., Leurini, S., Wyrowski, F., et al. 2011, A&A, 526, A59
Demyk, K., Wlodarczak, G., & Carvajal, M. 2008, A&A, 489, 589
Draine, B. T. & Lee, H. M. 1984, ApJ, 285, 89
Dubernet, M.-L., Daniel, F., Grosjean, A., & Lin, C. Y. 2009, A&A, 497, 911
Dulieu, F., Amiaud, L., Congiu, E., et al. 2010, A&A, 512, A30
Dulieu, F., Congiu, E., Noble, J., et al. 2013, Scientific Reports, 3, 1338
Einstein, A. 1916, Deutsche Physikalische Gesellschaft, 18
Einstein, A. 1917, Physikalische Zeitschrift, 18
Elitzur, M. & Watson, W. D. 1978, ApJ, 222, L141
Emprechtinger, M., Lis, D. C., Rolffs, R., et al. 2013, ApJ, 765, 61
Encrenaz, T. 2008, ARA&A, 46, 57
Faure, A. & Josselin, E. 2008, A&A, 492, 257

Faure, A., Wiesenfeld, L., Scribano, Y., & Ceccarelli, C. 2012, MNRAS, 420, 699
Fey, A. L., Claussen, M. J., Gaume, R. A., Nedoluha, G. E., & Johnston, K. J. 1992, AJ, 103, 234
Fraser, H. J., Collings, M. P., McCoustra, M. R. S., & Williams, D. A. 2001, MNRAS, 327, 1165
Furuya, K., Aikawa, Y., Hincelin, U., et al. 2015, A&A, 584, A124
Furuya, K., van Dishoeck, E. F., & Aikawa, Y. 2016, A&A, 586, A127
Galli, D. & Palla, F. 1998, A&A, 335, 403
Gálvez, Ó., Maté, B., Herrero, V. J., & Escribano, R. 2011, ApJ, 738, 133
Gaume, R. A., Fey, A. L., & Claussen, M. J. 1994, ApJ, 432, 648
Geiss, J. & Reeves, H. 1981, A&A, 93, 189
Gensheimer, P. D., Mauersberger, R., & Wilson, T. L. 1996, A&A, 314, 281
Gerlich, D. 1982, in Symposium on Atomic and Surface Physics, ed. W. Lindinger, F. Howorka, T. Maerk, & F. Egger, 304
Giannetti, A., Brand, J., Sánchez-Monge, Á., et al. 2013, A&A, 556, A16
Gibb, E., Nummelin, A., Irvine, W. M., Whittet, D. C. B., & Bergman, P. 2000, ApJ, 545, 309
Gibb, E. L., Whittet, D. C. B., Boogert, A. C. A., & Tielens, A. G. G. M. 2004, ApJS, 151, 35
Glover, S. C. O. & Abel, T. 2008, MNRAS, 388, 1627
Goldsmith, P. F. & Langer, W. D. 1999, ApJ, 517, 209
Gómez, Y., Rodríguez-Rico, C. A., Rodríguez, L. F., & Garay, G. 2000, Rev. Mexicana Astron. Astrofis., 36, 161
Green, S. 1986, ApJ, 309, 331
Green, S. 1989, ApJS, 70, 813
Green, S. 1994, ApJ, 434, 188
Green, S. & Chapman, S. 1978, ApJS, 37, 169
Hartogh, P., Lis, D. C., Bockelée-Morvan, D., et al. 2011, Nature, 478, 218
Hatchell, J., Millar, T. J., & Rodgers, S. D. 1998a, A&A, 332, 695
Hatchell, J., Thompson, M. A., Millar, T. J., & MacDonald, G. H. 1998b, A&AS, 133, 29
Heaton, B. D., Little, L. T., & Bishop, I. S. 1989, A&A, 213, 148
Herbst, E. & Klemperer, W. 1973, ApJ, 185, 505
Herbst, E. & van Dishoeck, E. F. 2009, ARA&A, 47, 427
Herpin, F., Chavarría, L., van der Tak, F., et al. 2012, A&A, 542, A76
Herpin, F., Marseille, M., Wakelam, V., Bontemps, S., & Lis, D. C. 2009, A&A, 504, 853
Hirota, T., Bushimata, T., Choi, Y. K., et al. 2008, PASJ, 60, 37
Hoare, M. G., Kurtz, S. E., Lizano, S., Keto, E., & Hofner, P. 2007, Protostars and Planets V, 181
Hogerheijde, M. R. & van der Tak, F. F. S. 2000, A&A, 362, 697
Hoover, R. B. 2006, Biogeosciences Discussions, 3, 23
Ivezić, Z. & Elitzur, M. 1997, MNRAS, 287, 799
Jacq, T., Walmsley, C. M., Henkel, C., et al. 1990, A&A, 228, 447
Jacq, T., Walmsley, C. M., Mauersberger, R., et al. 1993, A&A, 271, 276
Jørgensen, J. K., Schöier, F. L., & van Dishoeck, E. F. 2002, A&A, 389, 908
Kasting, J. F., Whitmire, D. P., & Reynolds, R. T. 1993, Icarus, 101, 108
Kong, S., Tan, J. C., Caselli, P., et al. 2016, ArXiv e-prints
Kristensen, L. E., van Dishoeck, E. F., van Kempen, T. A., et al. 2010a, A&A, 516, A57
Kristensen, L. E., Visser, R., van Dishoeck, E. F., et al. 2010b, A&A, 521, L30+

Kuchar, T. A. & Bania, T. M. 1994, ApJ, 436, 117
Küppers, M., O'Rourke, L., Bockelée-Morvan, D., et al. 2014, Nature, 505, 525
Kurtz, S. 2005, in IAU Symposium, Vol. 227, Massive Star Birth: A Crossroads of Astrophysics, ed. R. Cesaroni, M. Felli, E. Churchwell, & M. Walmsley, 111–119
Kurtz, S., Cesaroni, R., Churchwell, E., Hofner, P., & Walmsley, C. M. 2000, Protostars and Planets IV, 299
Lada, C. J. 1987, in IAU Symposium, Vol. 115, Star Forming Regions, ed. M. Peimbert & J. Jugaku, 1–17
Lamberts, T., Cuppen, H. M., Ioppolo, S., & Linnartz, H. 2013, Physical Chemistry Chemical Physics (Incorporating Faraday Transactions), 15, 8287
Lampton, M., Margon, B., & Bowyer, S. 1976, ApJ, 208, 177
Larson, R. B. 1969, MNRAS, 145, 271
Latter, W. B. 1989, PhD thesis, Arizona Univ., Tucson.
Lécluse, C. & Robert, F. 1994, Geochim. Cosmochim. Acta, 58, 2927
Lee, J.-E. & Bergin, E. A. 2015, ApJ, 799, 104
Lepp, S. & Shull, J. M. 1984, ApJ, 280, 465
Lepp, S., Stancil, P. C., & Dalgarno, A. 2002, Journal of Physics B Atomic Molecular Physics, 35, R57
Linsky, J. L. 2003, Space Science Reviews, 106, 49
Lis, D. C., Biver, N., Bockelée-Morvan, D., et al. 2013, ApJ, 774, L3
Liu, F.-C., Parise, B., Kristensen, L., et al. 2011, A&A, 527, A19
Liu, F.-C., Parise, B., Wyrowski, F., Zhang, Q., & Güsten, R. 2013, A&A, 550, A37
Loinard, L., Castets, A., Ceccarelli, C., Caux, E., & Tielens, A. G. G. M. 2001, ApJ, 552, 163
Mangum, J. G., Plambeck, R. L., & Wootten, A. 1991, ApJ, 369, 169
McKee, C. F. & Ostriker, E. C. 2007, ARA&A, 45, 565
Meier, R., Owen, T. C., Matthews, H. E., et al. 1998, Science, 279, 842
Mezger, P. G., Altenhoff, W., Schraml, J., et al. 1967, ApJ, 150, L157
Michael, J. V. & Fisher, J. R. 1990, The Journal of Physical Chemistry, 94, 3318
Mielke, S. L., Lynch, G. C., Truhlar, D. G., & Schwenke, D. W. 1994, The Journal of Physical Chemistry, 98, 8000
Millar, T. J., Bennett, A., & Herbst, E. 1989, ApJ, 340, 906
Mitchell, D. N. & Roy, D. J. L. 1973, The Journal of Chemical Physics, 58, 3449
Miyauchi, N., Hidaka, H., Chigai, T., et al. 2008, Chemical Physics Letters, 456, 27
Mizuno, A., Onishi, T., Hayashi, M., et al. 1994, Nature, 368, 719
Mokrane, H., Chaabouni, H., Accolla, M., et al. 2009, ApJ, 705, L195
Molinari, S., Pezzuto, S., Cesaroni, R., et al. 2008, A&A, 481, 345
Mookerjea, B., Casper, E., Mundy, L. G., & Looney, L. W. 2007, ApJ, 659, 447
Mookerjea, B., Vastel, C., Hassel, G. E., et al. 2014, A&A, 566, A61
Nomura, H. & Millar, T. J. 2004, A&A, 414, 409
Oba, Y., Miyauchi, N., Hidaka, H., et al. 2009, ApJ, 701, 464
Oba, Y., Osaka, K., Watanabe, N., Chigai, T., & Kouchi, A. 2014, Faraday Discuss., 168, 185
Offer, A. R., van Hemert, M. C., & van Dishoeck, E. F. 1994, J. Chem. Phys., 100, 362
Olmi, L., Araya, E. D., Chapin, E. L., et al. 2010, The Astrophysical Journal, 715, 1132
Olmi, L., Cesaroni, R., & Walmsley, C. M. 1996, A&A, 307, 599

Ossenkopf, V. & Henning, T. 1994, A&A, 291, 943
Pagani, L., Salez, M., & Wannier, P. G. 1992, A&A, 258, 479
Pardo, J. R., Cernicharo, J., Herpin, F., et al. 2001, ApJ, 562, 799
Parise, B., Castets, A., Herbst, E., et al. 2004, A&A, 416, 159
Parise, B., Caux, E., Castets, A., et al. 2005a, A&A, 431, 547
Parise, B., Ceccarelli, C., & Maret, S. 2005b, A&A, 441, 171
Parise, B., Ceccarelli, C., Tielens, A. G. G. M., et al. 2006, A&A, 453, 949
Parise, B., Leurini, S., Schilke, P., et al. 2009, A&A, 508, 737
Parise, B., Simon, T., Caux, E., et al. 2003, A&A, 410, 897
Peimbert, M. & Torres-Peimbert, S. 1999, ApJ, 525, 1143
Persson, M. V., Jørgensen, J. K., & van Dishoeck, E. F. 2013, A&A, 549, L3
Persson, M. V., Jørgensen, J. K., van Dishoeck, E. F., & Harsono, D. 2014, A&A, 563, A74
Pineau des Forets, G., Flower, D. R., & McCarroll, R. 1991, MNRAS, 248, 173
Pottage, J. T., Flower, D. R., & Davis, S. L. 2004, MNRAS, 352, 39
Prasad, S. S. & Tarafdar, S. P. 1983, ApJ, 267, 603
Prodanović, T., Steigman, G., & Fields, B. D. 2010, MNRAS, 406, 1108
Puy, D., Alecian, G., Le Bourlot, J., Leorat, J., & Pineau Des Forets, G. 1993, A&A, 267, 337
Ragan, S., Henning, T., Krause, O., et al. 2012, A&A, 547, A49
Ratajczak, A., Quirico, E., Faure, A., Schmitt, B., & Ceccarelli, C. 2009, A&A, 496, L21
Richet, P., Bottinga, Y., & Javoy, M. 1977, Annual Review of Earth and Planetary Sciences, 5, 65
Roberts, H., Herbst, E., & Millar, T. J. 2003, ApJ, 591, L41
Roberts, H., Herbst, E., & Millar, T. J. 2004, A&A, 424, 905
Roberts, H. & Millar, T. J. 2007, A&A, 471, 849
Rolffs, R., Schilke, P., Wyrowski, F., et al. 2011, A&A, 527, A68+
Roueff, E., Dartois, E., Geballe, T. R., & Gerin, M. 2006, A&A, 447, 963
Roueff, E., Lis, D. C., van der Tak, F. F. S., Gérin, M., & Goldsmith, P. F. 2005, A&A, 438, 585
Roueff, E., Parise, B., & Herbst, E. 2007, A&A, 464, 245
Roueff, E., Tiné, S., Coudert, L. H., et al. 2000, A&A, 354, L63
Saraceno, P., Andre, P., Ceccarelli, C., Griffin, M., & Molinari, S. 1996, A&A, 309, 827
Schilke, P., Comito, C., Thorwirth, S., et al. 2006, A&A, 454, L41
Schnee, S., Enoch, M., Noriega-Crespo, A., et al. 2010, ApJ, 708, 127
Schöier, F. L., van der Tak, F. F. S., van Dishoeck, E. F., & Black, J. H. 2005, A&A, 432, 369
Shimonishi, T., Onaka, T., Kato, D., et al. 2010, A&A, 514, A12
Shu, F. H., Adams, F. C., & Lizano, S. 1987, ARA&A, 25, 23
Snell, R. L. & Wootten, H. A. 1977, ApJ, 216, L111
Sridharan, T. K., Beuther, H., Saito, M., Wyrowski, F., & Schilke, P. 2005, The Astrophysical Journal Letters, 634, L57
Steigman, G. 2006, International Journal of Modern Physics E, 15, 1
Sultanov, R. A. & Balakrishnan, N. 2004, The Journal of Chemical Physics, 121, 11038
Taquet, V., Charnley, S. B., & Sipil, O. 2014, The Astrophysical Journal, 791, 1
Tarchi, A., Greve, A., Peck, A. B., et al. 2004, MNRAS, 351, 339
Teixeira, T. C., Devlin, J. P., Buch, V., & Emerson, J. P. 1999, A&A, 347, L19
Thi, W.-F., Woitke, P., & Kamp, I. 2010, MNRAS, 407, 232

Thompson, A., Moran, J., & Swenson, G. 2008, Interferometry and Synthesis in Radio Astronomy (Wiley)
Tielens, A. G. G. M. & Hagen, W. 1982, A&A, 114, 245
Turner, B. E. 1990, ApJ, 362, L29
Turner, B. E. 2001, ApJS, 136, 579
van Buren, D., Mac Low, M.-M., Wood, D. O. S., & Churchwell, E. 1990, ApJ, 353, 570
van der Tak, F. F. S., Chavarría, L., Herpin, F., et al. 2013, A&A, 554, A83
van der Tak, F. F. S., Walmsley, C. M., Herpin, F., & Ceccarelli, C. 2006, A&A, 447, 1011
van Dishoeck, E., Blake, G., Jansen, D., & Groesbeck, T. 1995, ApJ, 447, 760
van Dishoeck, E. F., Bergin, E. A., Lis, D. C., & Lunine, J. I. 2014, Protostars and Planets VI, 835
van Dishoeck, E. F., Herbst, E., & Neufeld, D. A. 2013, Chemical Reviews, 113, 9043
van Dishoeck, E. F., Kristensen, L. E., Benz, A. O., et al. 2011, PASP, 123, 138
Villanueva, G. L., Mumma, M. J., Bonev, B. P., et al. 2009, ApJ, 690, L5
Visser, R. et al., A&A, in prep.
Visser, R., Jrgensen, J. K., Kristensen, L. E., van Dishoeck, E. F., & Bergin, E. A. 2013, The Astrophysical Journal, 769, 19
Wagner, A. F. & Graff, M. M. 1987, ApJ, 317, 423
Wagoner, R. V. 1969, ApJS, 18, 247
Wagoner, R. V. 1973, ApJ, 179, 343
Wang, K.-S. 2013, Small Scale Kinematics of Massive Star-Forming Cores (PhD thesis)
Ward-Thompson, D., Casali, M., & Whitworth, A. 2004, An Introduction to Star Formation (Cambridge University Press)
Ward-Thompson, D., Scott, P. F., Hills, R. E., & Andre, P. 1994, MNRAS, 268, 276
Watanabe, N. & Kouchi, A. 2008, in Progress in Surface Science, Vol. 83, 439–489
Watt, S. & Mundy, L. G. 1999, ApJS, 125, 143
Weber, A. S., Hodyss, R., Johnson, P. V., Willacy, K., & Kanik, I. 2009, ApJ, 703, 1030
Weiß, A., De Breuck, C., Marrone, D. P., et al. 2013, ApJ, 767, 88
Wilking, B. A. 1989, PASP, 101, 229
Williams, S. J., Fuller, G. A., & Sridharan, T. K. 2004, A&A, 417, 115
Wilson, T., Rohlfs, K., & Hüttemeister, S. 2000, Tools of Radio Astronomy: Problems and Solutions, Astronomy and Astrophysics Library (Springer Berlin Heidelberg)
Wood, D. O. S. & Churchwell, E. 1989, ApJS, 69, 831
Wootten, A., Loren, R. B., & Snell, R. L. 1982, ApJ, 255, 160
Wyrowski, F., Güsten, R., Menten, K. M., et al. 2016, A&A, 585, A149
Wyrowski, F., Güsten, R., Menten, K. M., Wiesemeyer, H., & Klein, B. 2012, A&A, 542, L15
Wyrowski, F., van der Tak, F., Herpin, F., et al. 2010, A&A, 521, L34+
Yang, J., Turner, M. S., Schramm, D. N., Steigman, G., & Olive, K. A. 1984, ApJ, 281, 493
Yang, L., Ciesla, F. J., & Alexander, C. M. O. . 2013, Icarus, 226, 256
Yıldız, U. A., van Dishoeck, E. F., Kristensen, L. E., et al. 2010, A&A, 521, L40+
Yorke, H. W. 1986, ARA&A, 24, 49
Zinnecker, H. & Yorke, H. W. 2007, ARA&A, 45, 481

Acknowledgements

I would like to thank Dr. Bérengère Parise who kindly leads me into the real world of astrochemistry. She was very nicely training and inspiring me. I would like to thank Dr. Friedrich Wyrowski and Prof. Dr. Karl Menten who kindly help me to finish this thesis and also the studies in high-mass star-forming regions. Prof. Dr. Pavel Kroupas acknowledged for his consistent support to my projects and for influencing me with his intuitive way of thinking. My study in star formation benefited from discussions with many colleagues and collaborators, especially Dr. Kuo-Song Wang and Dr. Silvia Leurini who brought me into their researches and made me realized many new possibilities. I also benefited from discussions with my friends, Dr. Rosie Chen, Dr. Pei-Ying Hsieh, Ru-Lin Cheng, Tzu-Ruei Yang and my officemates in MPIFR. Dr. Dirk Murders is thanked for providing helps on computational aspect. I also would like to thank Barbara Menten and Tuyet-Le Tran for dealing the problems happened in my daily life, and would like to thank the Dr. Rainer Mauersberger and Simone Pott for their efforts in our IMPRS. Finally, thanks for my dear family, my sister and my parents for supporting me in research and life every time, no matter what I want to do.